

UNIVERSITY OF BELGRADE
FACULTY OF MECHANICAL ENGINEERING



Ahmed Ali Irhayim Abubaker

**NUMERICAL AND EXPERIMENTAL SIMULATION OF
ATMOSPHERIC BOUNDARY LAYER INFLUENCE ON FLOW
PATTERNS AROUND BUILDING STRUCTURES**

DOCTORAL DISSERTATION

BELGRADE, 2021

**УНИВЕРЗИТЕТ У БЕОГРАДУ
МАШИНСКИ ФАКУЛТЕТ**



Ахмед Али Ирхаим Абубакер

**НУМЕРИЧКА И ЕКСПЕРИМЕНТАЛНА СИМУЛАЦИЈА
УТИЦАЈА АТМОСФЕРСКОГ ГРАНИЧНОГ СЛОЈА НА
СТРУЈНО ПОЉЕ ОКО ГРАЂЕВИНСКИХ ОБЈЕКТА**

ДОКТОРСКА ДИСЕРТАЦИЈА

БЕОГРАД, 2021

Members of the Committee

Dr. Ivan Kostić, full professor, **Supervisor of Doctoral Dissertation**
University of Belgrade, Faculty of Mechanical Engineering

Dr. Časlav Mitrović, full professor
University of Belgrade, Faculty of Mechanical Engineering

Dr. Aleksandar Bengin, full professor
University of Belgrade, Faculty of Mechanical Engineering

Dr. Aleksandar Simonović, full professor
University of Belgrade, Faculty of Mechanical Engineering

Dr. Marija Samardžić, assistant professor
University of Defense, Military Accademy, Belgrade, and
scientific associate, Military Technical Institute (VTI) Belgrade

Date of defense:

ACKNOWLEDGEMENTS

First of all, I would like to express deep gratitude to my supervisor professor Dr. Ivan Kostić for his encouragement, wise suggestions, assistance throughout this work, and for introducing me to the field of computational and experimental aerodynamic aspects of wind engineering by providing me the opportunity to verify my computational results in Belgrade University wind tunnel. Next, I would like to thank the assistant professor Dr. Olivera Kostić for her support in my CFD investigations and laboratory work and for providing assistance in preparing the conference and journal publications.

I also would like to take this opportunity to extend my sincere gratitude to the late professor Dr. Zoran Stefanović for his initial guidance and advices.

I would also like to thank professor Dr. Časlav Mitrović and all the staff at Belgrade University wind tunnel facility for their assistance, help, and patience.

Lastly but most importantly, I want to express my gratitude to my mother, brothers, sisters, wife, and lovely daughter, who gave me support and patience to make this thesis possible.

Above all, I am very much grateful to almighty Allah for giving me the courage and good health to complete this study.

NUMERICAL AND EXPERIMENTAL SIMULATION OF ATMOSPHERIC BOUNDARY LAYER INFLUENCE ON FLOW PATTERNS AROUND BUILDING STRUCTURES

ABSTRACT

Wind forces can cause huge damage to the building elements due to their inadequate design or material deterioration. The differences in surface pressures that create these complex forces depend on the interaction of many variables, natural variables such as wind speed and turbulence, ground surface features, air properties, with building variables as the shape, location, and physical properties of structures. A high level of information on the magnitude and variety of the pressures is required for managing the risk to buildings from the wind. This information has conventionally been collected during series of full-scale and wind tunnel tests, but these can corroborate both expensive and time-consuming. For this reason, Computational Fluid Dynamics (CFD) methods nowadays are adequate tools for predicting flow characteristics over buildings, informing decisions, and guiding the design.

In this thesis, a computational algorithm has been established and implemented within the CFD model as a simulated virtual wind tunnel, with the aim to investigate wind flow characteristics of several types of atmospheric boundary layers (ABLs) and their influence on low and medium-rise buildings. The CFD model's accuracy and high operational capabilities have been established by defining the optimal assignments of a number of important computational parameters, such as the computational domain size, inlet boundary conditions, mesh configuration, the turbulence model type, solver schemes, and solution methods.

Results of several numerical simulations performed within the scope of this thesis have been compared and validated both by some existing, and newly performed wind tunnel tests for the purpose of the thesis fulfillment, and by the recommendations of the relevant national wind standards for civil engineering, with the aim to assess the performance of the CFD model and determine its appropriate simulation parameters for various flow cases. Also, some of the ABL flow characteristics and mechanisms of wind pressure influence on low and medium-rise buildings have been identified.

The provided CFD model's performance has firstly been tested using already existing wind tunnel test cases, which simulated certain terrain types using different passive obstacle types. Results from two wind tunnel facilities have been considered: the smooth and suburban terrains simulated in the open-loop Assuit University (Egypt) wind tunnel and the urban terrain in the closed-loop Belgrade University, Faculty of Mechanical Engineering wind tunnel. The CFD model has shown good agreement with the experiments for both terrain types.

Within the next step, the pressures on a medium-rise building with complex geometry have been investigated both experimentally and numerically. For the purpose of this thesis, a custom model of the building was created and tested in the Belgrade University wind tunnel, using the same obstacle types as in earlier tests mentioned in the previous paragraph. The good agreements between the newly obtained experimental data and numerical results have also confirmed the high level of accuracy and the capability of here established CFD model to properly predict pressures on this kind of buildings.

In the final step, a new different type of terrain has been designed within the CFD model's Belgrade University virtual wind tunnel, aimed to numerically investigate pressure coefficient values and distributions on three low-rise building models with different roof shapes. The good

prediction of pressure coefficients compared to the relevant national wind standards data has also confirmed the capability and accuracy of the established CFD model to study the wind influence on this kind of buildings.

With the proper simulations of various atmospheric boundary layers and well predictions of pressure on low and medium-rise buildings, here presented CFD model can offer a cost-effective alternative tool for wind engineering applications and make considerable enhancements to the existing national wind standards used for structural building design and analyses.

Keywords: atmospheric boundary layer, wind influence on buildings, wind tunnel tests, CFD calculations, medium-rise buildings, low-rise buildings, qualitative analysis, quantitative analysis.

Scientific discipline: Mechanical engineering

Scientific sub-discipline: Aeronautical engineering

UDC 533.6.011:69.2/.6:519.87(043.3)

НУМЕРИЧКА И ЕКСПЕРИМЕНТАЛНА СИМУЛАЦИЈА УТИЦАЈА АТМОСФЕРСКОГ ГРАНИЧНОГ СЛОЈА НА СТРУЈНО ПОЉЕ ОКО ГРАЂЕВИНСКИХ ОБЈЕКТА

САЖЕТАК

Силе генерисане ветром могу изазвати велика оштећења на зградама услед њиховог неадекватног пројектовања, или недовољне чврстоће примењених материјала. Разлике у површинским притисцима које могу генерисати овако разорне силе зависе од великог броја утицајних фактора, као што су брзина ветра и степен турбуленције, утицај околних објеката на тлу, других својстава струјног поља ваздуха, карактеристика саме зграде у контексту њеног облика, локације и њених структуралних својстава. Да би се правилно проценио утицај притисака изазваних ветром на ниво ризика којем зграде могу бити изложене, потребно је обезбедити што више адекватних информација о локалној расподели и вредностима притиска. Те информације су се уобичајено добијале комбиновањем испитивања објеката у реалном окружењу и испитивања модела у аеротунелима, али такав приступ може бити како скуп, тако и дуготрајан. У савременим условима, компјутерска динамика флуида (енгл. Computational Fluid Dynamics - CFD) прерасла је у релевантан нови прорачунски алат за адекватну процену карактеристика струјног поља око зграда, дефинисање улазних параметара и правилно вођење грађевинског пројекта у овом контексту.

У овој докторској дисертацији установљен је и примењен прорачунски CFD модел у оквиру кога је извршена сумулација виртуелног аеротунела, са циљем да се помоћу њега врше испитивања различитих типова атмосферског граничног слоја и њиховог утицаја на ниске зграде и зграде средње величине. Тачност CFD модела и његова висока оперативна применљивост постигнути су дефинисањем оптималних задавања одређеног броја важних прорачунских параметара, као што је величина контролне запремине, гранични услови на њеном улазу, конфигурисање прорачунске мреже, избор турбулентног модела, солвера и прорачунских метода.

Резултати нумеричких симулација обављених у овој дисертацији верификовани су поређењем како са већ постојећим, тако и са новим аеротунелским испитивањима наменски обављеним у оквиру израде ове дисертације, али и са препорукама датим у релевантним Националним стандардима за грађевинске инжењере, са циљем верификовања могућности установљеног CFD модела и одређивања одговарајућих симулационих параметра за различите случајеве струјања. Поред тога, успешно су идентификоване неке специфичне карактеристике атмосферског граничног слоја и механизми утицаја притисака изазваних ветром на ниске и средње зграде.

Могућности установљеног CFD модела најпре су верификоване коришћењем већ постојећих резултата аеротунелских испитивања, где су вршене симулације одређених типова терена коришћењем различитих пасивних препрека. Поређења су обављена са резултатима из два различита аеротунела: за раван и приградски терен симулиран у аеротунелу Универзитета Асуит (Египат) отореног типа, као и за урбани терен симулиран у аеротунелу затвореног типа на Мшинском факултету Универзитета у Београду. Прорачун је дао добра поклапања са експериментом за оба типа терена.

У наредном кораку анализирани су притисци на моделу зграде средње величине са комплексном геомеријом, како експериментално тако и нумерички. У оквиру израде ове дисертације, наменски је израђан модел ове зграде и извршено је његово испитивање у аеротунелу Универзитета у Београду, коришћењем истих типова препрека које су коришћене у претходно поменутих ранијим испитивањима у овом аеротунелу. Добра поклапања

прорачунских и нових експерименталних резултата пружила су потврду о високом нивоу тачности резултата, као и могућности установљене CFD методе да пружи добре предикције расподеле притисака на зградама ове категорије.

У финалном кораку, у овако установљеном виртуелном CFD моделу аеротунела Универзитета у Београду, извршено је моделирање новог типа терена са циљем да се нумерички одреде вредности коефицијента притиска и његова расподела на три модела малих зграда са различитим облицима кровова. Остварена су добра поклапања прорачунских резултата коефицијената притиска са карактеристичним случајевима разматраним у релевантним националним стандардима, што је пружило потврду да се овај прорачунски модел може успешно користити и за анализу утицаја ветра на ову категорију зграда.

Захваљујући добрим предикцијама расподеле притиска на малим и средњим зградама, уз правилно моделирање различитих типова атмосферског граничног слоја, прорачунски CFD модел представљен у овој дисертацији може представљати алтернативни - финансијски и временски ефикаснији прорачунски алат у односу на класичне у области инжењерских анализа утицаја ветра и пружити могућност за даља унапређења постојећих националних стандарда намењених структуралној анализи и пројектовању зграда.

Кључне речи: атмосферски гранични слој, утицај ветра на зграде, аеротунелска испитивања, CFD прорачуни, средње зграде, ниске зграде, квалитативна анализа, квантитативна анализа.

Научна област: Машинство

Ужа научна област: Ваздухопловство

UDC 533.6.011:69.2/.6:519.87(043.3)

TABLE OF CONTENTS

LIST OF FIGURES	X
LIST OF TABLES	XIII
CHAPTER 1: INTRODUCTION.....	1
1.1 Background.....	1
1.2 Thesis Motivation	1
1.3 Scope and Objectives.....	2
1.4 Overview of Thesis Contents	2
CHAPTER 2: LITERATURE REVIEW.....	4
2.1 Atmospheric Boundary Layer (ABL).....	4
2.2 Simulation of Atmospheric Boundary Layer in Wind Tunnel	6
2.3 Wind Pressure Effects on Buildings.....	7
2.4 Previous and Related CFD Studies.....	10
2.4.1 Previous CFD Studies for ABL Simulated in the Wind Tunnels.....	10
2.4.2 Previous CFD Studies for Medium-rise buildings.....	12
2.4.3 Previous CFD Studies for Low-rise buildings	13
CHAPTER 3: NUMERICAL SIMULATION	15
3.1 Introductory remarks	15
3.2 Governing Equations	15
3.3 Turbulence Models	17
3.3.1 Boussinesq Hypothesis.....	18
3.3.2 The Shear Stress Transport (<i>SST</i>) $k-\omega$ Model	18
3.3.2.1 Modeling the Effective Diffusivity	18
3.3.2.2 Modeling the Turbulence Production.....	20
3.3.2.3 Modeling the Turbulence Dissipation	20
3.3.2.4 Cross-Diffusion Modification	21
3.3.3 General Conservation Equation or General Scalar Transport Equation.....	21
3.4 Numerical Solution Methodology	21
3.4.1 The Density-Based Solver.....	21
3.4.2 The Discretization of the General Scalar Transport Equation	22
3.4.2.1 Discretization of the Temporal Term	23
3.4.2.2 Discretization of the Convection Term	23
3.4.2.3 Discretization of the Diffusion Term	24
3.4.2.4 Discretization of the Source Term.....	24
3.4.2.5 Solving the Linear System Equations	25

3.4.3 Density-Based Solver for the Coupled Set of Governing Equations.....	25
3.4.3.1 Governing Equations in Vector Form	25
3.4.3.2 The Discretization of the General Vector Equation	27
3.4.3.3 Spatial Discretization	27
3.4.3.4 Linearization.....	28
3.4.4 Solution Methods	29
3.4.4.1 The Multi-grid Methods	29
3.4.4.1.1 Geometric Multi-Grid	29
3.4.4.1.2 Algebraic Multi-Grid	32
3.4.4.2 The Gauss-Seidel Method	32
3.4.4.3 The Incomplete Lower Upper Method.....	33
 CHAPTER 4: CFD MODELING OF ATMOSPHERIC BOUNDARY LAYER.....	34
4.1 Wind Tunnels Experiments	34
4.1.1 The Assiut University Wind Tunnel	34
4.1.2 The Belgrade University Wind Tunnel.....	35
4.2 The CFD Simulations and Verifications	36
4.2.1 Computational Domain and Mesh Configuration	36
4.2.2 Setup and Solution	37
4.3 Results and Discussion	37
4.3.1 Comparison of CFD and Wind Tunnel Experiments Results	37
4.3.2 Valuation of Wind Velocity Profile Parameters	42
 CHAPTER 5: EXPERIMENTAL AND NUMERICAL ANALYSIS OF A MEDIUM RISE-BUILDING WIND LOADINGS	46
5.1 The Wind Tunnel Experiment	46
5.1.1 Building Model	46
5.1.2 Experiment Instruments	48
5.1.3 Sensors Testing	50
5.1.3.1 Velocity Calibration for the Sensors	50
5.1.3.2 Pressure Calibration for the Sensors	52
5.1.4 Experimental Procedures	55
5.2 Numerical Simulation of the Medium-Rise Building.....	56
5.2.1 Numerical Simulation Procedure	56
5.2.1.1 Computational Domains and Mesh Configuration.....	56
5.2.1.2 Setup and Solution.....	57
5.3 Results and Comparisons.....	58
 CHAPTER 6: NUMERICAL ANALYSIS OF LOW-RISE BUILDINGS.....	81
6.1 Wind Standards and Codes.....	81
6.2 Generate the Required ABL on the Belgrade University Virtual Wind Tunnel	82

6.2.1 Redesign of the passive devices on the Belgrade University Virtual Wind Tunnel	82
6.2.2 Numerical Simulation for the Empty Virtual Wind Tunnel with the New Design of the Passive Devices.....	84
6.3 Numerical Simulation of the Low-rise Buildings.....	85
6.3.1 Modeling the Low-rise Buildings	85
6.3.2 Numerical Simulation Procedure	86
6.3.2.1 Geometry and Mesh	86
6.3.2.2 Setup and Solution.....	88
6.4 Results and Discussion	88
6.4.1 Area-averaged Pressure Coefficients	88
6.4.2 Comparison of the CFD Results with the AS-NZS 1170-2, 2011 Standard.....	89
6.4.2.1 The Comparison on the Gabled roof low-rise building.....	90
6.4.2.2 The Comparison on the Mono-sloped roof low-rise building.....	91
6.4.2.3 The Comparison on the Curved roof low-rise building	93
CHAPTER 7: CONCLUSION AND RECOMMENDATIONS FOR FUTURE WORK	95
7.1 Summary and Conclusion.....	95
7.2 Recommendations for Future Work	96
REFERENCES.....	98

LIST OF FIGURES

Figure 2.1 Schematic illustration of the ABL structure	4
Figure 2.2 Log law and power law regions in the mean wind velocity profile	5
Figure 2.3 The power law profiles over different terrain types	6
Figure 2.4 Flow pattern around cuboidal building.....	7
Figure 2.5 Distribution of pressures (+) and suction (-) on flat roof low rise building.....	8
Figure 2.6 Mean pressure coefficient contours on a cube: (a) when the flow is blowing normal to the front face, (b) when the flow is blowing at 30° to the cube.....	9
Figure 3.1 Illustration of the density-based solver.....	22
Figure 3.2 Adjacent Cells c_0 and c_1 with Vectors	23
Figure 3.3 Node agglomeration to form coarse grid cells.....	29
Figure 3.4 The three levels V-cycle GMG Algorithm	30
Figure 3.5 Illustration of the FMG Initialization	31
Figure 4.1 Construction components and their details of the Assiut University wind tunnel, all dimensions in mm	34
Figure 4.2 Photograph of the boundary layer development section with the passive devices and test section at Assiut University wind tunnel	35
Figure 4.3 Components of the Belgrade University wind tunnel	35
Figure 4.4 Picture of the test section with the passive devices at Belgrade University wind tunnel.....	36
Figure 4.5 The unstructured meshes for two cases tested at the Assuit wind tunnel, (a) – Case of spires only, and (b) – case of spires and surface roughness.....	36
Figure 4.6 The unstructured mesh for the Belgrade wind tunnel model.....	37
Figure 4.7 Contours of velocity magnitude for case 1, for the three different fan speeds 500, 1000, and 1440 rpm, respectively	38
Figure 4.8 Comparisons of mean velocity profiles for case 1, for the three different fan speeds	38
Figure 4.9 Contours of velocity magnitude for case 2, for the three different fan speeds 500, 1000, and 1440 rpm, respectively	39
Figure 4.10 Comparisons of mean velocity profiles for case 2, for the three different fan speeds	40
Figure 4.11 Contours of mean velocity at various cross-sections, at 1440 rpm fan speed, (a) for case 1, and (b) for case 2.....	40
Figure 4.12 Contours of velocity magnitude for case 3, in the plane of symmetry	41
Figure 4.13 Comparisons of the relative velocity profiles for case 3	41
Figure 4.14 Contours of mean velocity for case 3 in various cross-sections, inside the test section.....	41
Figure 4.15 Contours of local eddy viscosity at 1000 rpm fan speed, (a) case 1, and (b) case 2.....	42
Figure 4.16 Contour of local eddy viscosity for case 3	42
Figure 4.17 Best fitting log law profiles, (a) for case 1, and (b) for case 2	43
Figure 4.18 Best fitting log law profile for case 3	44
Figure 4.19 Best fitting power law profiles, (a) for case 1, and (b) for case 2	44
Figure 4.20 Best fitting power law profile for case 3	45
Figure 5.1 Metropol Palace Hotel at Belgrade, Serbia	46
Figure 5.2 Model building dimensions in mm, with turntable plate.....	47
Figure 5.3 Taps locations on the model surfaces, all dimensions in mm	47
Figure 5.4 Taps locations on the canopy surfaces, all dimensions in mm.....	48
Figure 5.5 (a) Adapter used to connect the 5 mm silicone tubing with the 3 mm pressure tap, (b) Adapter glued to the model wall	48

Figure 5.7 Sensors hosing box of the multi-manometer	49
Figure 5.6 Cap box of the multi-manometer	49
Figure 5.8 Sensors connection to the Arduino	50
Figure 5.9 BOSCH BMP280 sensor	50
Figure 5.10 Pitot tube used for testing sensors	51
Figure 5.11 The sensor inside an air capsule filter	51
Figure 5.12 Velocity calculated for the first two sensors	52
Figure 5.13 Velocity calculated for the second two sensors	52
Figure 5.14 Comparison between measured pressures and the wind tunnel nominal speed.....	53
Figure 5.15 Sensors connections and calibration procedure.....	53
Figure 5.16 Typical operation screen.....	54
Figure 5.17 Calibration results for the first sensor.....	54
Figure 5.18 Calibration results for the second sensor.....	54
Figure 5.19 The model isometric view shows the locations of the sensors	55
Figure 5.20 Absolute pressure measurements on the model at 0 m/s	55
Figure 5.21 The model positions on the wind tunnel test section.....	56
Figure 5.22 The computational domain when the collector included.....	57
Figure 5.23 Unstructured mesh generated for the model building and the zone around it.....	57
Figure 5.24 Isometric and back views of the model with faces, rows, and sensors numbers	58
Figure 5.25 Top view of the model with faces, rows, and sensors numbers	58
Figure 5.26 Pressure comparison at 0 degrees wind direction azimuth, 5 m/s	60
Figure 5.27 Pressure comparison at 0 degrees wind direction azimuth, 10 m/s	61
Figure 5.28 Pressure comparison at 0 degrees wind direction azimuth, 15 m/s	62
Figure 5.29 Pressure comparison at 0 degrees wind direction azimuth, 20 m/s	63
Figure 5.30 Pressure comparison at 45 degrees wind direction azimuth, 5 m/s	64
Figure 5.31 Pressure comparison at 45 degrees wind direction azimuth, 10 m/s	65
Figure 5.32 Pressure comparison at 45 degrees wind direction azimuth, 15 m/s	66
Figure 5.33 Pressure comparison at 45 degrees wind direction azimuth, 20 m/s	67
Figure 5.34 Pressure comparison at 90 degrees wind direction azimuth, 5 m/s	68
Figure 5.35 Pressure comparison at 90 degrees wind direction azimuth, 10 m/s	69
Figure 5.36 Pressure comparison at 90 degrees wind direction azimuth, 15 m/s	70
Figure 5.37 Pressure comparison at 90 degrees wind direction azimuth, 20 m/s	71
Figure 5.38 Pressure comparison at 135 degrees wind direction azimuth, 5 m/s	72
Figure 5.39 Pressure comparison at 135 degrees wind direction azimuth, 10 m/s	73
Figure 5.40 Pressure comparison at 135 degrees wind direction azimuth, 15 m/s	74
Figure 5.41 Pressure comparison at 135 degrees wind direction azimuth, 20 m/s	75
Figure 5.42 Absolute pressure contours at 0 degrees wind direction azimuth, (a) 5 m/s, (b) 10 m/s, (c) 15 m/s, and (d) 20 m/s	76
Figure 5.43 Absolute pressure contours at 10 m/s, (a) 45 degrees, (b) 90 degrees and	76
Figure 5.44 Eddy viscosity at 0 degrees wind direction azimuth, 5 m/s.....	77
Figure 5.45 Eddy viscosity at 0 degrees wind direction azimuth, 10 m/s.....	78
Figure 5.46 Eddy viscosity at 0 degrees wind direction azimuth, 15 m/s.....	78
Figure 5.47 Eddy viscosity at 0 degrees wind direction azimuth, 20 m/s.....	79
Figure 5.48 Eddy viscosity at 45 degrees wind direction azimuth, 10 m/s.....	79
Figure 5.49 Eddy viscosity at 90 degrees wind direction azimuth, 10 m/s.....	80
Figure 5.50 Eddy viscosity at 135 degrees wind direction azimuth, 10 m/s.....	80
Figure 6.1 Spire base width variation with the power law exponent (Simiu et al., 1978).....	83
Figure 6.2 The elliptic spire model, dimensions in mm.....	83
Figure 6.3 The unstructured mesh for the computational domain	84
Figure 6.4 (a) Wind velocity profiles, (b) Turbulence intensity profile	85

Figure 6.5 The best curve fitting for the height z.....	85
Figure 6.6 (a) The model of the gabled roof building, (b) The model of the mono-sloped roof building, (c) The model of the curved roof building, dimensions in mm	86
Figure 6.7 The unstructured meshes generated for model buildings and zones around them: (a) gabled roof (b) mono-sloped roof, (c) curved roof.....	87
Figure 6.8 (a) Parameters for the gabled roof low-rise buildings, (b) Parameters for the mono-sloped roof low-rise buildings	89
Figure 6.9 Parameters for the curved roof low-rise buildings	89
Figure 6.10 Pressure coefficient distributions for the gabled roof model, frontal (left) and rear (right) isometric view	90
Figure 6.11 Flow pattern around the gabled roof model at a vertical section.....	91
Figure 6.12 Pressure coefficient distributions for the mono-sloped roof model, frontal (left) and rear (right) isometric view	92
Figure 6.13 Flow pattern around the mono-sloped roof model at a vertical section	92
Figure 6.14 Pressure coefficient distributions for the curved roof model, frontal (left) and rear (right) isometric view	93
Figure 6.15 Flow pattern around the curved roof model at a vertical section	94

LIST OF TABLES

Table 2-1 Terrain types, roughness length, [8]	5
Table 4-1 The number of mesh elements on every computational domain	37
Table 4-2 Values of u^* , z_0 and d	43
Table 5.1 Technical data of BOSCH BMP280 sensor	50
Table 5.2 Number of elements in every computational domain	57
Table 6-1 The key parameters that affect the values of pressure coefficients in the four standards	82
Table 6-2 The number of elements created in each unstructured mesh	87
Table 6-3 Comparison of the pressure coefficients on the gabled roof low-rise building	90
Table 6-4 Comparison of the pressure coefficients on the mono-sloped roof low-rise building	91
Table 6.5 Comparison of the pressure coefficients on the curved roof low-rise building	93

CHAPTER 1: INTRODUCTION

1.1 Background

The wind has a significant influence in different structures, especially for the buildings built deep in the boundary layer on the earth's surface where wind flow unsteadiness, speed gradients, and wind turbulence are high. Most buildings on earth with lower heights fall in this category as low and medium-rise buildings, which are generally used for various purposes such as residential houses, industrial and commercial buildings, and public facilities. These buildings are commonly exposed to high wind pressure, which causes damages and instabilities in their structural form, particularly the non-engineered buildings built in conventional ways without recourse to eligible engineers or architects.

However, damages or failures of cladding and parts of these buildings due to wind loads can be very costly, starting with local surface damage and finishing with total crumbling. These damages may occur either directly or indirectly with respect to the velocity profile and turbulence intensity, besides variation of the building geometry. Having this in mind, it is clear that knowing the nature of pressures on buildings induced by wind will enable safer design provided by engineers and thus, more economical buildings [1].

In the recent couple of decades, many wind tunnels and some full-scale experiments have been used to investigate the wind pressures of low-rise buildings, while few investigations involve medium-rise buildings [2]. Consequently, since World War II, several codes of practice and national wind standards were produced to design different building types against wind loads [3]. Furthermore, in the 1970s, the use of CFD in indoor and outdoor building airflows began and expanded later to include different building design aspects [4].

1.2 Thesis Motivation

The full-scale experiments are the most reliable for obtaining wind-measured data representing real-life wind loads on buildings. This type of testing is ordinarily performed just in a few points in building components and space around it, without or with control over the boundary conditions. Also, such testing is expensive and time-consuming [5].

However, wind tunnel testing permits a considerable amount of control over boundary conditions, even though the Reynolds numbers are significantly smaller in wind tunnel tests than in actual buildings. Tests can further be laborious, expensive, and suffer from potentially irreconcilable similarity requirements. Also, measurements in wind-tunnel are regularly performed only in few points in and around a building [5–7].

On the other hand, CFD methods are becoming increasingly accepted as an alternative tool for optimizing different building shapes and arrangements. The CFD estimation of wind loads offers advantages over the full-scale or reduced-scale testing in boundary layer wind tunnels. For example, any Reynolds number, boundary layer profile, and turbulence can be simulated by CFD. Furthermore, CFD methods are suitable also for design practice since it can estimate the flow domain around a building. They also can predict all the variables of interest under well-controlled conditions such as velocity, pressure, and temperature, and these results can be visualized, including all needed details. The most advanced CFD methods are still quicker and less expensive than full-scale experiments and reduced-scale wind tunnels experiments [6–9].

However, most full-scale and wind tunnels experiments were performed to investigate the wind pressures of low and medium-rise model buildings with simple shapes and relatively small plan dimensions [1], in the same way as the wind standards and codes deal with regular-shaped buildings, since their data based on some past wind tunnels experiments [10]. This issue raises the need for procedures more applicable and accurate CFD techniques for extending codes of practice.

These techniques are more time-efficient and thus economical than wind standards or experiments in building design.

Anyhow, more research work using CFD is still required, keeping in mind that CFD techniques application is limited because CFD results are susceptible to a wide range of simulation parameters, mainly defined by users. For example, the computational domain size, boundary conditions, mesh configuration, turbulence model, and solver schemes and methods can lead to large discrepancies in simulation results, providing another argument for experimental results to be used in validation of simulation.

1.3 Scope and Objectives

The primary goal of this thesis is to establish an accurate and reliable CFD model that might resemble complex flow patterns in wind tunnels with various obstacles, used to study the influences of wind on low and medium-rise buildings with different configurations. The goal was accomplished by fulfilling the following objectives:

- Review and identify key issues of the most critical flow characteristics and atmospheric conditions for estimating wind flow patterns around the buildings immersed in the atmospheric boundary layer.
- Define the simulation parameters of the computational model, which will provide lower computational cost and the best possible matches with the relevant experimental results when modeling the atmospheric boundary layer field, in the planned relevant range of speeds of 1÷50 m/s.
- Explore the computational model ability and efficiency to simulate different atmospheric boundary layers of complex topographies. Previously published experimental data based on tests performed in different wind tunnels using various types of obstacles such as barrier walls, spires, and roughness elements will be presented to validate the numerical simulation results. The defined simulation parameters with some modifications related to adjustment to existing geometries will be used.
- Inspect the computational model ability and accuracy in predicting the wind pressures on the modeled medium-rise building surfaces with a canopy attached to its façade and on the canopy itself. This building model will be assembled and tested in the Belgrade University Wind Tunnel test section to measure pressures in the relevant points and zones of its surfaces. The measured data will be used to confirm the numerical simulation results. Further verification and additional correction, updating, and optimizing the simulation parameters will be performed, if necessary.
- Evaluate the computational model applicability to simulate new ABL in the existent virtual wind tunnel test section for future studies.
- Inspect the computational model ability and accuracy in predicting the wind pressures on several low-rise buildings with various roof shapes and base dimensions. Each simulation result will be compared to the Australian/New Zealand Standard (AS-NZS) data.

The established and verified computational model would be able to substitute a significant number of wind tunnel testing hours and lessen the total cost of analyzing aerodynamic loads that act on buildings at various wind speeds, directions, and atmospheric boundary layer profiles. Thus, such research would become accessible to building projects with lower budgets.

1.4 Overview of Thesis Contents

The thesis is arranged into seven chapters, as follows:

- *Chapter one* gives the general background and sets the primary goal of this thesis with related objectives.
- *Chapter two* presents and discusses the main characteristics of the Atmospheric Boundary Layer, the approaches and criteria of simulating the appropriate ABL in Wind Tunnel, and

the essential features of the flow around buildings. Some previous CFD studies for simulated ABL generated in Wind Tunnel and investigated wind effect on low and medium-rise buildings are also reviewed.

- *Chapter three* introduces the theoretical background of the CFD and looks in depth at the numerical solution methodology that has been performed using Ansys Fluent code. It also covers and describes a set of selected simulation parameters for the provided CFD computational model, such as the turbulence model, spatial and temporal discretization methods and schemes, and solver methods. These parameters were sufficient to ensure credibility and employed in all numerical simulations performed in this study.
- *In chapter four*, different ABLs generated in two types of wind tunnels using various obstacles and different speeds in their test sections were simulated numerically in order to verify the accuracy of the CFD computational model in simulating different ABLs. The rest of the simulation parameters for the provided CFD computational model were defined and discussed. These parameters were the computational domain, mesh configuration, and boundary conditions, which were modified to adjust to existing geometries. Subsequently, Computational results were compared with available experimental data for validation.
- *In chapter five*, the wind pressures on a model of medium-rise are studied experimentally and numerically. Several experimental tests in the Belgrade University wind tunnel were carried out of the medium-rise building model immersed in ABL with urban area exposure category. A detailed specification of the assembly of the model and laboratory instruments and equipment are also provided. The predicted pressures on the model were obtained and investigated using the provided CFD computational model with different computational domains and boundary conditions to assess the optimum configuration. Computational results are then compared with experimental results for validation.
- *In chapter six*, the provided CFD computational model performed in chapter four for the Belgrade University wind tunnel was redesigned to simulating ABL of open country exposure. The modified CFD computational model was used to investigate pressure coefficients on three types of low-rise buildings. Computational results were compared with the AS-NZS Standard data for validation.
- *Chapter seven* presents the conclusions and some recommendations for future research.

CHAPTER 2: LITERATURE REVIEW

2.1 Atmospheric Boundary Layer (ABL)

The boundary layer concept in the fluid flow can conceivably be credited to Froude, who performed a series of laboratory towing tests in the early 1870s to investigate the frictional resistance of a tinny plate towed in still water [11]. The ABL is the layer of air up to 1000-2000 m above the earth's surface that is generated by the friction between the airflow and the ground [12]. With increasing height above the earth's surface, the effect of friction on decelerating airflow movement decreases. The airflow velocity gradually retrieves to the gradient wind at the top of the ABL. The ABL thickness range varies according to the following terrain roughness categories:

1. Smooth terrain (open sea, ice, or desert),
2. Open country or rural terrain (villages, low scrub, or scattered trees),
3. Suburban terrain (residential areas, small towns, or well-wooded areas),
4. Urban terrain (numerous tall buildings, city centers, or industrial areas) [13].

Figure 2.1 shows the simplified illustration of the ABL structure over some roughness, where the ABL can be separated into the inner layer and the outer layer [14].

The inner layer (sometimes described as the atmospheric surface layer or Prandtl layer) is the lowest 10% of the ABL depth [15]. This layer also can be separated into the interfacial (roughness) sublayer and the inertial sublayer. The interfacial sublayer (commonly introduced as the canopy layer) is sited nearly the earth's surface with a span 2 to 5 times the average building height [16], and its depth is called the (zero-plane displacement). The inertial sublayer is the zone above the interfacial sublayer, and this layer with the interfacial sublayer is directly influenced by characteristics of ground surface.

The outer layer is the region over the inner layer, sometimes called the Ekman layer, where flow properties are not affected by the surface roughness.

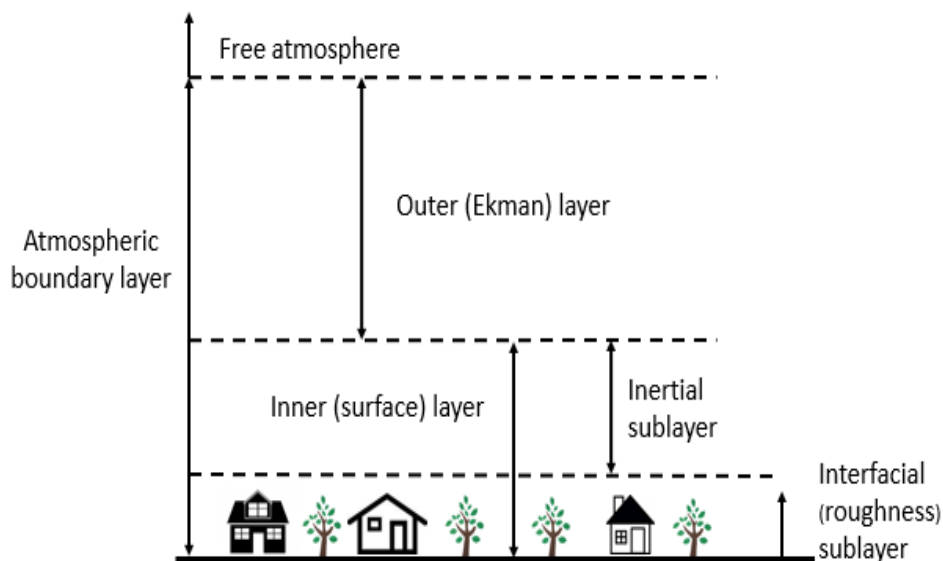


Figure 2.1 Schematic illustration of the ABL structure

The flow in the ABL is represented by two standard laws for velocity profile, the logarithmic law (log law), which is more suited in the inner layer of the ABL, and the power law, which is better in the outer layer [17], as shown in Figure 2.2. Mathematically, the logarithmic law is written as:

$$\frac{U(z)}{u_*} = \frac{1}{k} \ln\left(\frac{z-d}{z_0}\right) \tag{2-1}$$

where:

$U(z)$ - is the mean wind velocity at any height z ,

u^* - is friction or shear velocity, which is a scaling velocity of the surface shear stress,

k - is Von Karman's constant, typically equal to 0.4,

d - is zero-plane displacement, equal to the average height of roughness elements,

z_0 - is roughness length. It is the height above the surface where the flow velocity is zero.

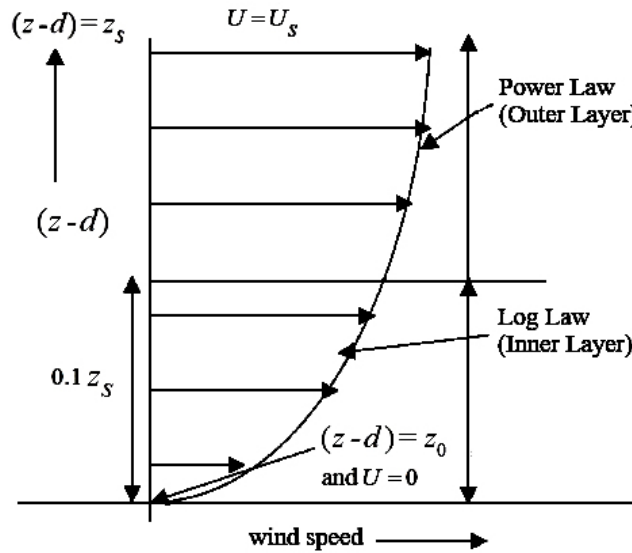


Figure 2.2 Log law and power law regions in the mean wind velocity profile

The roughness length z_0 changes according to the type of terrain, and its appropriate values have been suggested by many studies, as given in Table 2-1, taken from the Australian Standard for Wind Loads, AS1170.2, 1989, [3].

Table 2-1 Terrain types, roughness length, [8]

Terrain types	roughness length (m)
Smooth terrain	0.001-0.005
Open country terrain	0.01-0.05
Suburban terrain	0.1-0.5
Urban terrain	1-5

Despite the accuracy and reliability of the logarithmic law to describe the mean wind profiles in the ABL surface layer, the meteorologists consider the power law as a more accurate depiction of strong wind profiles in the lower atmosphere [18].

The power law mathematically can be described as:

$$\frac{U(z)}{U_s} = \left(\frac{z-d}{z_s}\right)^\alpha \tag{2-2}$$

where:

U_s - is the mean wind velocity at a chosen reference height z_s ,

α - is the power index or exponent, which is used to describe the shape of the mean velocity profile and is related to surface roughness (i.e. terrain type).

The corresponding values of α for different terrain types are shown in Figure 2.3.

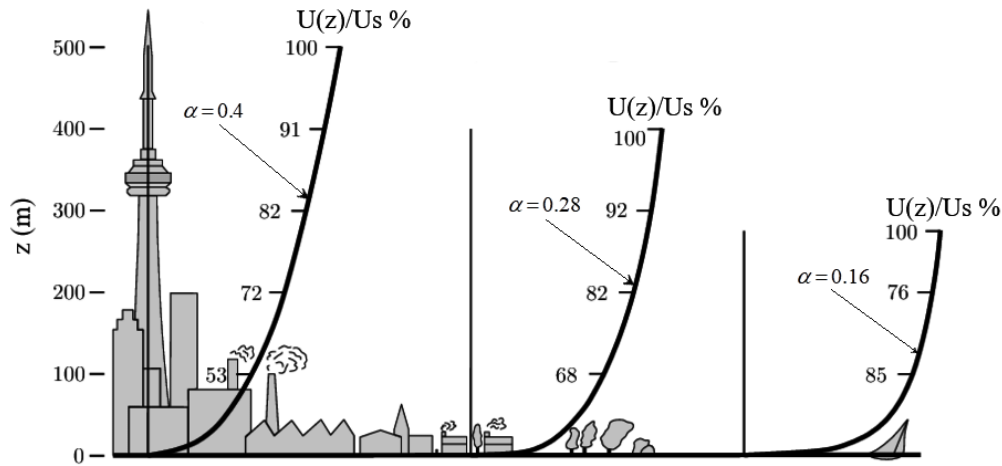


Figure 2.3 The power law profiles over different terrain types

The other parameter that characterizes the ABL besides the mean velocity profile is a turbulence intensity profile. The longitudinal turbulent intensity $I_u(z)$ is used to quantify the amount of turbulence in the wind. It is indicated as the ratio of standard deviation of longitudinal wind velocity to the mean velocity:

$$I_u(z) = \frac{\sigma_u(z)}{\bar{U}(z)} \quad (2-3)$$

where:

$\sigma_u(z)$ - is the root mean square of fluctuating velocity $\sqrt{u'^2(z)}$, known as the longitudinal standard deviation of wind velocity at height z ,

$\bar{U}(z)$ - is the mean velocity of longitudinal component at any height z .

Since the fluctuation of velocity increases with the increasing of the ground roughness, which causes an increase of the standard deviation, the turbulence intensity reduces with the height as $\sigma_u(z)$ decreases and $\bar{U}(z)$ increases with the height [1,19].

2.2 Simulation of Atmospheric Boundary Layer in Wind Tunnel

Although several theoretical and empirical formulas have been established by meteorological surveys for the ABL's characteristics, other efforts have been attained to create a 'model' ABL in a wind tunnel to explain other complex effects attendant fluid flow that remain uncertain [20].

The concept of using the wind tunnel for boundary layer testing dates to the beginning of 1940s when Wieghardt in Göttingen used the natural boundary layer at the wind tunnel floor to investigate the spread of plumes [10]. However, the length scale of wind tunnel was very small to allow wider applications, e.g. for building aerodynamics [18]. Major modifications happened when Jensen (1958) performed experiments on building models, noticing that "the current model test for phenomena in the wind must be carried out in a turbulent boundary layer and the model law requires the boundary layer to be scaled with regards to the velocity profile" [1,10]. Ever since, more accurate simulation of the atmospheric boundary layer in wind tunnels began its upward trajectory. Jensen, Cermak in the USA (1958), and Davenport (1965) in Canada were the early adopters in designing special Atmospheric boundary layer wind tunnels (ABLWTs) for wider applications in building aerodynamics [21]. ABLWTs are typical of a subsonic or low-speed type, dividing according to the air blowing into open loop or closed loop wind tunnels [22].

In general, simulation of ABL in the wind tunnels can be reached by a natural formation or human-made devices. The natural formation of ABL requires a wind tunnel with a 20 to 30 m long test section to produce simulated ABL with a small thickness in the range of 0.5-1 m at an ambient

wind speed of about 10 m/s [23]. The various types and shapes of human-made devices, such as barrier walls, spires, uniform grid or screens, and roughness elements, or the combination of some of them, were instituted in an attempt to generate accurate wind velocity and turbulence profiles of the simulated ABL by several authors [24–27]. The role of the barrier walls is to provide an initial momentum close the lowest of ABL to regulate the shape of the wind velocity profile, and the spires play a significant task in creating the boundary layer height. The uniform grid or screens were also used to create thick velocity profiles over a short generation distance and turbulence of a specific scale and intensity. Additionally, dense roughness elements are used to modify the lower part of the wind velocity profile [22,28].

However, a detailed description of similarity of atmospheric and wind tunnel boundary layers is published in [22]. Applicable similarity criteria as matching velocity profiles, turbulence intensities, integral length scale, power spectrum, and Reynolds numbers for both the model and nature scale are more trial and error than exact science [18]. Theoretically, the Reynolds number similarity is impossible to reach. Otherwise, the Reynolds number similarity for sharp-edged structures modeled in boundary layer flow is not a severe restriction and can be relaxed [29]. Some researchers, [1,18], recommended that the model Reynolds numbers (Re_M) must surpass 11,000 for sharp-edged structures or 100,000 for round structures, and another research [30] recommended $Re_M > 15,000$ for sharp-edged structures.

Furthermore, testing of buildings in wind tunnels requires a building model scaled by matching the Jensen number ($Je=h/z_0$), which is described as the ratio of the building height (h) and the surface roughness length (z_0) of the surrounding terrain. Actually, its variation causes the variation of the pressure coefficients in the building model [31]. The blockage ratio, defined as the ratio between the projected model area and the wind tunnel cross-section area, should also be considered smaller than 5% during the experiments [32]. In contrast, when the blockage ratio is higher, the accelerated flow in the constricted segment between the model and the wind tunnel walls will increase the model structure load [33].

2.3 Wind Pressure Effects on Buildings

The wind is one of critical ambient forces to be considered in building design. Actual wind conduct is altered by the boundary-layer conditions and building geometry.

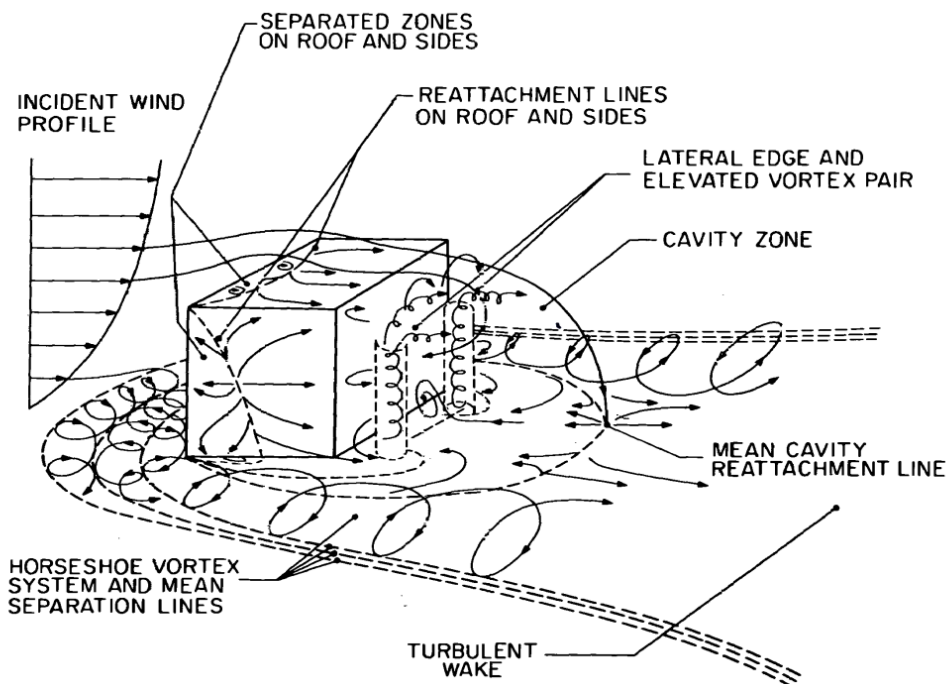


Figure 2.4 Flow pattern around cuboidal building

Figure 2.4 [34] shows the flow patterns and some of its principal phenomena around a simple building (cuboidal building) immersed in a deep turbulent ABL. The flow approaching the building separates from its facade at a distance upwind of the building, depending on building height to width ratio and upstream surface roughness. The exposed facade will experience a pressure higher than the ambient as the approaching flow decelerates. Since the incident wind speed minimizes with decreasing height, a downward-directed pressure gradient will be recognized as the flow reduces near the upwind face. This gradient drives a downward-directed flow along the face (at the ground), which will move out from the building and roll-up into a vortex [18,35].

Above this vortex, the incident flow hits the building's face and moves outward toward its edges. The flow separates at these front edges and may or may not reattach to the building roof or sides before reaching their back edges. Reattachment depends on building height to length ratio, length to width ratio, and the turbulence intensity in the approaching flow. The separated boundary layers move out into the nearby fluid as free shear layers, the separated layers curve inward toward the wake axis, feeding into a "cavity" or recirculation "bubble" directly downwind of the building. In cases where the flow reattaches to the building sides and roof, the wake cavity may be more complex due to the existence of vertical vortices behind the lee side edges. These vortices combine with the main flow near the roof level and bend over, and they work to remove flow from the cavity to the wake region. The frontal vortex is also enfolded around the building by interacting with the approaching flow near the building's sides into a horseshoe shape. The horseshoe vortex can be bounded in the flow at some distance downwind [35–37].

The profile of the boundary separating from the streamlined flow and the vortex regions should be recognized prior to velocities and pressures can be determined. Therefore, applying this basic idea will help in predicting where pressures and suctions occur. Pressure occurs when streamline flow boundary is pushed up, while suction occurs when it curves back. The suction or pressure would be higher at the sharper curvature of the boundary [38].

Figure 2.5 [39] presents the pressure distribution on the flat roof low rise building, where the windward wall is the only surface exposed to pressure, since all other surfaces are in the wake with pressures being inferior to the ambient.

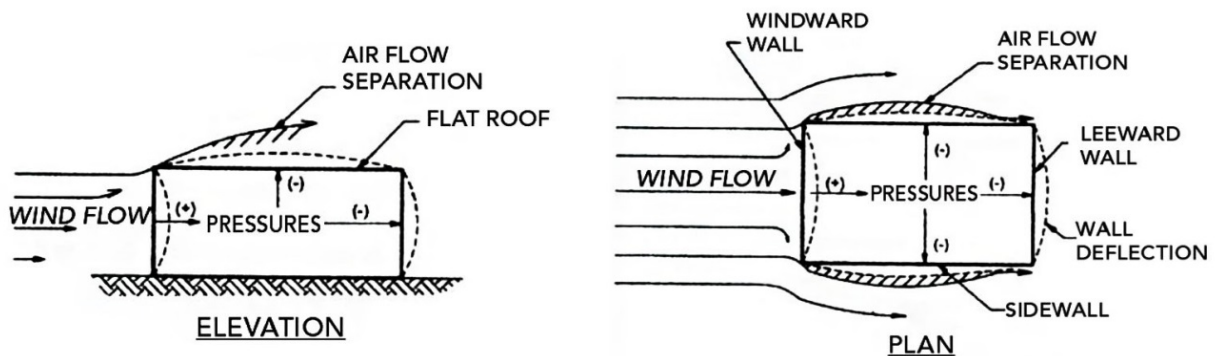


Figure 2.5 Distribution of pressures (+) and suctions (-) on flat roof low rise building

Wind pressures on a building rely on the contact between wind and building and wind speed. Since wind is moving air, the exertive pressures are related to its kinetic energy. If one considers that the total kinetic energy is transformed into pressure, the resulting increase is defined by the expression ($q_{ref} = \frac{1}{2} \rho u^2$), where ρ is the air density, and u is the velocity of the undisturbed air. This is known as the stagnation pressure and is the maximum positive pressure increase over the atmospheric pressure (P_o) that can be exerted on a building surface by the wind of any certain speed [40].

The pressure at any position in the streamlined flow can be calculated from the velocity due to the constant total energy, being the sum of velocity energy and pressure energy. Therefore, to calculate the local surface pressure, the atmospheric pressure (P_o) will be applied as a reference pressure, so that from Bernoulli's equation, one gets:

$$P_{surface} - P_o = 1/2 \rho (u_0^2 - u_{surface}^2) = 1/2 \rho u_0^2 [1 - (u_{surface}/u_0)^2] \quad (2-4)$$

Furthermore, the surface pressure can be formulated by a non-dimensional pressure coefficient C_p , as:

$$C_p = 1 - (u_{surface}/u_0)^2 = \frac{P_{surface} - P}{1/2 \rho u_0^2} = \frac{\Delta P}{q_{ref.}} \quad (2-5)$$

Pressure coefficients utilized in practice have been evaluated by testing the models of various types of structures in wind tunnels. Sometimes it is more suitable to evaluate the pressure in coefficients form than absolute values because the wind's pressure fluctuations are much smaller than the absolute atmospheric pressure.

Figure 2.6 [41] displays an example of the pressure coefficient distributions on surfaces of the flat roof low-rise building. The contours of C_p on the cube walls are plotted when the flow is blowing normal and at 30° to the cube. It should be noted that the strong suction on the corner of the roof is produced by the conical vortices (delta-wing), which arise when the flow blowing skewed at angles other than normal to one of the walls, as shown in Figure 2.6 (b).

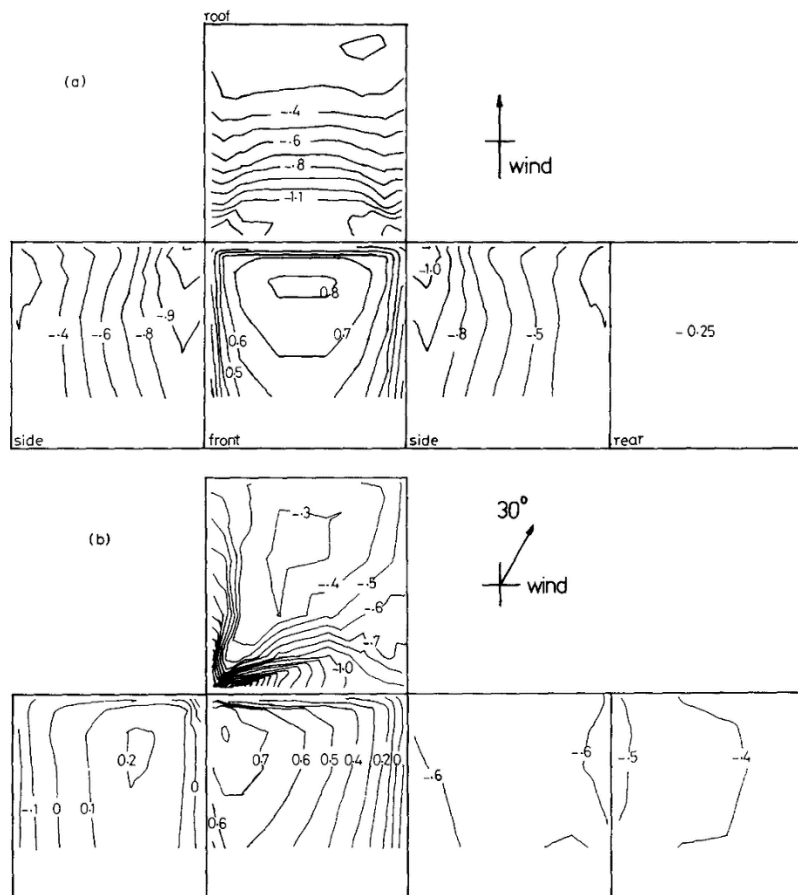


Figure 2.6 Mean pressure coefficient contours on a cube: (a) when the flow is blowing normal to the front face, (b) when the flow is blowing at 30° to the cube

In general, local pressure distributions acting on the low-rise building are functionally reliant on building dimensions and flow parameters. Building dimensions are the ratio of height, width, and length to each other, also with the height of the building relative to boundary layer thickness or its roughness length. In contrast, flow parameters are wind velocity at roof height, wind velocity profile exponent, longitudinal turbulence intensity, and wind direction [42].

After testing several types of enclosed low rise building models in the turbulent boundary layer, mainly when the wind blow is normal to buildings, the following common characteristics of wind-induced pressure distributions have been observed [40,43,44]:

- Pressures on the windward wall (front wall) of building models are positive due to pushing influence, but decrease gradually as the flow accelerates around the sides and the upper edge of the face.
- Pressures on the leeward wall (rear wall) are negative, noting the slight decrease of their absolute value downwards.
- Pressures on the roof with low slope and side walls are mostly negative with very large localized suction due to flow separating from their leading edges.
- Also, for low-rise buildings with steep roofs, as the roof slope increases away from the critical angle, the windward roof pressure increases in a positive direction and the suction on the leeward roof has no obvious changes.

2.4 Previous and Related CFD Studies

2.4.1 Previous CFD Studies for ABL Simulated in the Wind Tunnels

The CFD with wind tunnel tests in wind engineering and aerodynamics has been extensively utilized in the last ten years to investigate a wide variety of processes in the lower parts of the ABL, such as pollutant dispersion and deposition, wind-driven rain, building ventilation, and wind loading on buildings or bridges. CFD methods are often used in association with physical experimentation like wind tunnel studies to validate and assess simulation data. Furthermore, CFD is sometimes used as a tool to assistance wind tunnel design testing and interpretation of results [4].

However, the CFD use in simulating ABL or studying wind effects on buildings is not an easy task. It needs some knowledge about all potential difficulties that users need to bear in mind commonly, such as the computational domain size, selection of the turbulence model, grid resolution, boundary conditions, and all other options set by the user [45].

Generally, the entire computational domain size is not a simple substance in the numerical solution of turbulent flow; it depends on the area of interest and boundary conditions. The ABL numerical simulation is sometimes implemented by modeling only the empty test section (conventional approach) and applying similar boundary conditions at the inlet as measured in the wind tunnel test section (inflow boundary conditions). Therefore, the mean velocity profile prescribed by power or logarithmic law, roughness length z_0 , and information about turbulence quantities is required at the inlet [8]. However, if the above conditions are not well-known, this approach may no longer be suitable, and a more general CFD modeling approach is needed.

Also, several solution strategies have been applied in this field by different CFD codes, as steady Reynolds-averaged Navier-Stokes (RANS), unsteady Reynolds-averaged Navier-Stokes (URANS), and Large Eddy Simulation (LES) or hybrid URANS/LES approaches. The RANS is the most common approach applied in CFD, despite its deficiencies. Studies that have employed URANS are rare. Otherwise, LES is increasingly used, but by far not as often as steady RANS [46,47]. First-order closure is the most straightforward approach for RANS models, wherein the turbulence models need to suggest expressions for the turbulent (eddy) viscosity and are named eddy viscosity models, such as the one-equation Spalart-Allmaras model, Standard $k-\varepsilon$ model, Renormalization Group (RNG) $k-\varepsilon$ model, Realizable $k-\varepsilon$ model, Standard $k-\omega$ model, and the $k-\omega$ shear stress transport (SST) model. Some of them will be described in the next chapter.

Shojaee et al. [48] modeled only the short test section of the Ankara Wind Tunnel to create the ABL for three different exposure categories, according to the American Society of Civil Engineers (ASCE) definition, by designing different configurations of spires and surface roughness elements at the inlet of the test section. That was achieved by using the $k-\varepsilon$ model turbulence model in commercial CFD Fluent software. Experiment tests were lately carried out after the design. The measured results of the velocity profiles showed acceptable agreement with CFD predictions and power-law (from ASCE) results.

Abdulrahim et al. [49] modeled two computational domains for two different wind tunnels, small and large-scale. Each computational domain consisted of the test section with an additional 3 m cross-section, which was added upstream of the spires and roughness elements. This extension was managed to compensate for the inlet contraction but not affecting the results, as long as the distance between spires and measurement locations is kept the same, as suggested by Amerio [50]. The CFD simulations using RANS equations with the *SST k- ω* model in the commercial CFD package FINE/Open were performed for both wind tunnels. The CFD simulations of different ABLs inside the small wind tunnel test section were primarily performed to validate the CFD approach. Furthermore, after the good agreement between the CFD and experimental results, the same CFD approach was applied to simulate the desired ABL for the large wind tunnel. In both cases, a constant velocity measured at the inlet of the boundary layer development section in the first wind tunnel was set as the inflow boundary conditions.

Yassen et al. [51] examined different turbulent models for their relative suitability for the ABL airflow using the Fluent software, and numerical results were compared with the available experimental data from Pires et al. [52]. The computational domain was modeled to the test section with three spires, a screen, and a carpet. Two sets of the CFD simulations have been accomplished to predict the velocity profile and turbulent intensity behind the test section's passive devices. The CFD simulations based on the modified *k- ϵ* turbulence model were performed in the first set when the screen was positioned at two different distances from the spires, and two different inlet boundary conditions (uniform flow and non-uniform flow) were applied. Predictive results of using the non-uniform inlet flow showed better agreement with experimental measurements for both screen positions. In the second set, other CFD simulations based on different models (modified *k- ϵ* , realizable *k- ϵ* , RNG, *k- ω* , *SST k- ω* , RMS, Spalart-Allmaras, and LES) were performed using only the non-uniform inlet flow. In this set, predictive results based on the modified *k- ϵ* turbulence model were the closest to the experimental measurements.

Yang et al. [53] modeled the conventional approach for the TJ-1 wind tunnel at Tongji University using the Fluent code to computationally verify the capability of the new inflow turbulence boundary conditions to model an equilibrium ABL. The new set of inflow turbulence boundary conditions is a theoretically derived solution to the standard *k- ϵ* model transport equations. Besides setting inflow velocity profiles, the new expression for the turbulent kinetic energy (*k*) was set at the inlet, allowing taking into account the decrease of *k* with height. In contrast, the profile for *k* is constant with height in the ordinary standard *k- ϵ* model. After simulations are performed, the numerical results of predicted outlet mean velocity and turbulent kinetic energy profiles are sustained throughout the domain, and their curves fit with wind tunnel test data.

Calautit et al. [54] modeled the entire closed-loop subsonic wind tunnel to perform a numerical investigation into the design and simulation of the flow parameters using the *k- ϵ* turbulence model in Fluent software. A uniform boundary condition of the measured pressure was imposed along the inlet surface (intake fan), and the pressure outlet was set to zero gauge pressure. Several guide vanes configurations were modeled and tested in the wind tunnel corners to eliminate the flow separations and improve the up-flow, cross-flow, and turbulence in the test section. The results of predicted and measured mean velocity and turbulence intensity profiles at the test section showed a good agreement. Furthermore, these results also showed that the flow quality was more influenced by adding the guide vanes in upstream corners in line with the test section than downstream. Another set of CFD simulations was performed to validate wind tunnel measurements of velocity, turbulence intensity, and pressure coefficients around the block model in the test section. The results showed the ability of this CFD model to replicate wind tunnel measurements with small errors.

Moonen et al. [55] modeled both the entire closed-loop subsonic wind tunnel and the conventional approach to establish a methodology for numerically modeling flow conditions in a wind tunnel. The CFD simulations using standard and realizable *k- ϵ* models were performed for validation with two sets of experiments comprising measurements in the empty test section and

around a block-type building model placed in the test section. Uniform boundary condition of the measured pressure was imposed along the inlet surface (intake fan) for the closed-circuit domain and available uniform velocity profile from the experiment at the inlet boundary condition for the conventional approach domain. The outlet zero static pressure was set for both domains. The predicted and measured results of velocities at all positions around the building model were compared, and the match of the results from the full wind tunnel model simulation was 2–4 times better than the conventional CFD analysis of the test section only.

Besides the previous researches that focused on modeling the entire wind tunnels, the conventional approach, or only the test sections with the placed passive devices, other researchers recommended modeling the contraction (effuse) with the test section to simulate accurate ABL in the test section. Blanco [56] modeled the contraction section of the open-loop low-speed wind tunnel using both 2-D and 3-D domains. Computational investigations were done in ANSYS Fluent based on the *SST k- ω* for 2-D computations and the BSL model for 3-D computations. Various inflow boundary-layer thicknesses and Reynolds numbers were set as boundary conditions for the inlet of the contraction to investigate the influence of inflow velocity profiles entering the contraction on the characteristics of the flow entering the test section. However, the results suggested that the uniform velocity profile into the contraction is a sufficient boundary condition since the displacement thickness of the boundary layer exiting the contraction is independent of the inlet displacement thickness, which is also confirmed by Pook et al. [57].

2.4.2 Previous CFD Studies for Medium-rise buildings

The great majority of CFD investigations have been established around either relatively tall or moderately low-rise buildings. Medium-rise buildings are those with heights between 20 and 120 m and a ratio of height to minimum width less than or equal to four [28], so only a few CFD investigations for buildings fall in this category.

Downie et al. [58] performed CFD simulations to replicate the results obtained in the wind tunnel tests to calculate allowable facade loads for a medium-rise building, using the *SST k- ω* model in Ansys CFX software. Experimental tests were carried out in a blockage tolerant boundary layer wind tunnel, where vertical spires, barriers, and roughness blocks were modeled to generate an open terrain category upstream of the building model. For the CFD, spatial computational domain, modified boundary conditions, and 3-grid independence were designed to ensure the consistency of the results. Mean pressure coefficients were measured and predicted on the windward, sides, leeward, and roof of the rectangular cylinder model with 60 m full scale's height, at varying degrees of incidence 0°, 30°, 60°, and 90°. Excellent results agreement was showed in central windward locations, and the results for all faces and all angles of incidence converged more as measured locations moved away from sharp edges.

Druenena et al. [59] applied different geometry modifications to a medium-rise building with 60 m height to reduce pedestrian-level wind (PLW) speed around it, like canopies, podiums, and permeable floors. CFD simulations using different turbulence models were performed to simulate mean wind speed around the building without modification (reference case) and validation with experiments in a wind tunnel. The realizable *k- ϵ* turbulence model was the accurate turbulence model and later used to study the effect of these modifications on PLW conditions. These modifications include: (i) different sizes of the canopy around the building at a fixed height above the pedestrian level, (ii) different sizes of the podium attached to the base of the building with the same height, and (iii) the introduction of a permeable floor in different floors of the target building. However, mean wind speeds at pedestrian level simulated for each modified case and compared with the reference case. The results showed that the canopy and podium modifications have a much higher effect on the PLW speed than introducing a permeable floor.

Hubova et al. [60] measured external pressure coefficients on an atypical cross-section medium-rise building with 91.5 m height in the open-circuit wind tunnel (SvF STU) built-in Bratislava (Slovakia) for comparison with achieved results by CFD simulations. The 3D transient RANS equations with the *SST k- ω* turbulence model using the Ansys Fluent software were

performed for two types of model surfaces (smooth and rough ones). The results of the external pressure coefficients at two levels on the building walls for four wind directions achieved by CFD were in good coincidence with the measured results.

2.4.3 Previous CFD Studies for Low-rise buildings

The common structures built all over the world can be categorized as low-rise buildings used for residential, commercial, and other purposes. Therefore, extensive numerical simulation work has been done for low-rise buildings with various shapes and placed in different terrain and topography types.

In this case, it is preferable to review only some of the previous CFD studies related to the types of low-rise buildings used in this thesis: gable, mono-slope, and curve roofs low-rise buildings.

Ozmen et al. [44] investigated the turbulent flow fields on the gabled roof low-rise building models having various pitch angles (15° , 30° , and 45°) submerged in ABL, experimentally and numerically. In the experiments, measurements of velocity and surface pressure with flow visualization around the models were carried out. The 3D solutions of the flow fields using the Ansys Fluent with two different turbulence models (realizable $k-\varepsilon$ and standard $k-\omega$) were achieved. The numerical results showed that the Realizable $k-\varepsilon$ predicted the mean velocity and turbulence kinetic energy better while the standard $k-\omega$ predicted the mean pressure coefficients better.

Similar work was performed by Tominaga et al. [61] on other gabled roof low-rise building models having various pitch angles (16.7° , 26.6° , and 36.9°). The CFD simulations using four turbulence models (the standard $k-\varepsilon$, RNG $k-\varepsilon$, realizable $k-\varepsilon$, and $SST k-\omega$) were performed for the 26.6° roof pitch model to compare results with the experiments. The turbulent kinetic energy obtained with the RNG $k-\varepsilon$ and the $k-\omega$ SST models show better performance than the other two models. On the other hand, the velocity results obtained with RNG $k-\varepsilon$ are slightly better than the results of other models.

Yang et al. [62] studied the influences of two different forms of inflow boundary conditions on modeling the equilibrium ABL and the specification of the $SST k-\omega$ turbulence model parameters by comparing numerical results and the wind tunnel test data of wind pressure distributions on the gabled roof low-rise building with 26.7° roof pitch. The two forms employed to define the inflow velocity conditions are the power-law model (POW-SST2) and the logarithm-law model (LOG-SST2). The wind pressures predicted by the LOG-SST2 are more coincide with the experimental data.

Peren et al. [63] studied the influence of different asymmetric opening window positions and different roof inclination angles on natural ventilation in the mono-sloped roof low-rise building models. First, CFD simulations were performed using different turbulence models for validation with previously published wind-tunnel measurements of the flat roof low-rise building model. The validation of results showed that the accuracy of the $SST k-\omega$ turbulence model is better than others. Other CFD simulations by the same accurate turbulence model were implemented to analyze the volume flow rate through the windows, wind velocity inside the building, and pressure coefficient on the building's windward and leeward walls when building geometry changes.

Holmes et al. [64] carried out computational investigations of mean pressure coefficients on various curved roof low-rise building configurations through 3D steady-state equations with the $k-\varepsilon$ turbulence model. Effects of three wind directions normal to the arch axis of the typical configuration building model and the effect of changed length/span ratio and rise/span ratio of building model on external pressure coefficients were computed. Moreover, the building's external and internal pressures with an open-end for two wind directions were also computed.

Ntinis et al. [65] examined experimentally and numerically three types of common low-rise buildings, curved, gabled, and flat roofs (with the same height, width, and length) to validate different turbulence models for predicting airflow patterns. An acceptable agreement was found between the experimental and CFD results regarding the velocities and the turbulence kinetic energies (TKE) around all building types. The results also showed that the $SST k-\omega$ model provides

better accuracy in predicting TKE, while the realizable $k-\varepsilon$ and RNG $k-\varepsilon$ models have better accuracy in predicting velocities.

Fouad et al. [66] performed an intensive study for common structures such as gabled and mono-sloped roof low-rise buildings, trusses, and domes to explain the capability of obtaining useful design data using the CFD technique. Preliminary CFD investigations were performed for validation with wind tunnel experiments. That was done by calculating pressure coefficients on a gabled roof building and circular silos using three types of flow: laminar flow, turbulent RNG $k-\varepsilon$, and LES flow types. The comparison of results showed that the laminar flow approach gave more conservative values than other applied models, so this approach was adopted for other CFD investigations. The predicted pressure coefficients on the four structures compared with the European (EURO) and the American Society of Civil Engineering Standard (ASCE) Codes values, and results showed very good agreement.

Abohela et al. [67] investigated the influence of the roof shape, wind direction, building height, and surrounding urban configurations on the wind flow above the roof of low-rise building models to identifying the optimum mounting location of roof-mounted wind turbines using CFD simulations. The realizable $k-\varepsilon$ turbulence model was used after their results of pressure coefficients on a cube have the best agreement to the data of 15 wind tunnel tests. However, in the first, stream-wise velocities and turbulence intensities were simulated for six different roof shapes covering a cubic building (flat, domed, gabled, pyramidal, curved, and mono-sloped roofs). The maximum normalized velocities that provide higher potential energies were achieved above the center of the domed and curved roofs in all wind directions. Then other simulations were then performed on curved roof models with different heights. The results showed increasing normalized stream-wise velocity with increasing building height at the same location above the building roof. The last simulations were performed on the curved roof building model surrounded by other cubical building models with different heights and configurations. Results showed that the normalized stream-wise velocities for all cases were less than the isolated building model case.

CHAPTER 3: NUMERICAL SIMULATION

3.1 Introductory remarks

Computational fluid dynamics provides different numerical methods to investigate complex fluid flows, including finite difference method (FDM), finite volume method (FVM), and finite element method (FEM). In CFD, the first step in solution process is discretization of a domain, and then numerical methods are applied to transform the partial differential equations into a series of discrete algebraic equations, to be solved numerically, with specified boundary conditions to simulate the flow field [68].

Among these methods, the FVM has some characteristics that make it the preferred method in CFD. It can be formulated in the physical space on unstructured meshes, where the spatial domain is discretized into non-overlapping elements (or finite volumes or cells). Another essential attribute of the FVM is that it is strictly conservative since the flow flux is entering a given volume matches that leave the adjacent volume. These face fluxes are predestined at the finite volume faces and calculated from some conservation equation terms. Finally, the unknown variables in the FVM are estimated at the central of the cells, not at their boundary faces, so it is easy to apply various boundary conditions in a non-invasive manner [69].

In this thesis, the numerical simulation is performed using the commercial Ansys Fluent code based on the FVM, developed for fluid flow and heat transfer modeling in complex geometries.

The pre-process needs to be prepared before start any numerical calculations, including:

- selection of the physical phenomena of interest to be numerically formulated (i.e., various concepts related to ABL or wind-induced pressures on the building),
- defining geometry of region (computational domain),
- generating mesh for the domain (domain discretization)
- defining boundary conditions.

3.2 Governing Equations

The governing equations of continuum mechanics can be written in the differential form as [69–72]:

1. Conservation of mass or continuity equation

$$\frac{\partial \rho}{\partial t} + \nabla \cdot (\rho \vec{V}) = 0 \quad (3-1)$$

2. Conservation of linear momentum

$$\frac{\partial \rho \vec{V}}{\partial t} + \nabla \cdot (\rho \vec{V} \vec{V}) = -\nabla p + \nabla \cdot \bar{\bar{\tau}} + \rho \mathbf{g} + \vec{F} \quad (3-2)$$

3. Conservation of energy

$$\frac{\partial \rho e}{\partial t} + \nabla \cdot (\rho e \vec{V}) = \nabla \cdot (\bar{\bar{\tau}} \cdot \vec{V}) - \nabla \cdot (p \cdot \vec{V}) - \nabla \cdot \dot{q}_s + \dot{q}_v \quad (3-3)$$

where:

ρ -is the density,

\vec{V} -is the velocity vector, $\vec{V} = ui + vj + wk$,

∇ -is the gradient of a scalar, $\nabla = (\partial / \partial x)i + (\partial / \partial y)j + (\partial / \partial z)k$,

P -is the pressure,

g -is the gravity,

\vec{F} -is external body forces,

e -is the total energy,

\dot{q}_s -is the rate of heat transfer,

\dot{q}_v -is the rate of heat source or sink,

$\bar{\tau}$ -is the stress tensor, and it is given by

$$\bar{\tau} = \mu \left[(\nabla \vec{V} + \nabla \vec{V}^T) - 2/3 (\nabla \cdot \vec{V}) I \right] \quad (3-4)$$

where μ is the molecular viscosity coefficient, I is the unit or identity tensor, and the gradient of a vector \vec{V} is a tensor given by

$$\nabla \vec{V} = \begin{bmatrix} \frac{\partial u}{\partial x} & \frac{\partial v}{\partial x} & \frac{\partial w}{\partial x} \\ \frac{\partial u}{\partial y} & \frac{\partial v}{\partial y} & \frac{\partial w}{\partial y} \\ \frac{\partial u}{\partial z} & \frac{\partial v}{\partial z} & \frac{\partial w}{\partial z} \end{bmatrix}, \text{ and its transpose } \nabla \vec{V}^T = \begin{bmatrix} \frac{\partial u}{\partial x} & \frac{\partial u}{\partial y} & \frac{\partial u}{\partial z} \\ \frac{\partial v}{\partial x} & \frac{\partial v}{\partial y} & \frac{\partial v}{\partial z} \\ \frac{\partial w}{\partial x} & \frac{\partial w}{\partial y} & \frac{\partial w}{\partial z} \end{bmatrix}$$

Also, the energy equation in terms of temperature reduces to

$$\frac{\partial}{\partial t} (\rho c_p T) + \nabla \cdot (\rho c_p T \vec{V}) = \nabla \cdot (k \nabla T) + Q^T \quad (3-5)$$

where c_p is the specific heat at constant pressure, T is the temperature, k is the thermal conductivity of the fluid, and Q^T is given by

$$Q^T = \rho T \frac{Dc_p}{Dt} - \left(\frac{\partial(\ln \rho)}{\partial(\ln T)} \right) \frac{Dp}{Dt} - 2/3 \Psi + \mu \Phi + \dot{q}_v \quad (3-6)$$

$$\Psi = \left(\frac{\partial u}{\partial x} + \frac{\partial v}{\partial y} + \frac{\partial w}{\partial z} \right)^2 \quad (3-7)$$

$$\Phi = 2 \left[\left(\frac{\partial u}{\partial x} \right)^2 + \left(\frac{\partial v}{\partial y} \right)^2 + \left(\frac{\partial w}{\partial z} \right)^2 \right] + \left(\frac{\partial u}{\partial y} + \frac{\partial v}{\partial x} \right)^2 + \left(\frac{\partial u}{\partial z} + \frac{\partial w}{\partial x} \right)^2 + \left(\frac{\partial v}{\partial z} + \frac{\partial w}{\partial y} \right)^2 \quad (3-8)$$

For natural ABL, the flow is incompressible, with neglect of the Coriolis effects by assuming the surface layer to be fully turbulent and adjacent enough to the earth's surface, and no heat added. The dissipation term Ψ has negligible from equation (3-1) when the density is constant. Moreover, the term $(\partial(\ln \rho)/\partial(\ln T))=0$ as the density is constant [68,69,73]. Therefore, the time-averaged governing equations become:

$$\frac{\partial \rho}{\partial t} + \nabla \cdot (\rho \vec{V}) = 0 \quad (3-9)$$

$$\frac{\partial \rho \bar{V}}{\partial t} + \nabla \cdot (\rho \bar{V} \bar{V}) = -\nabla p + \nabla \cdot \left\{ \mu \left[(\nabla \bar{V} + \nabla \bar{V}^T) \right] \right\} + \rho g \quad (3-10)$$

$$\frac{\partial}{\partial t} (\rho c_p T) + \nabla \cdot (\rho c_p T \bar{V}) = \nabla \cdot (k \nabla T) + \Phi \quad (3-11)$$

3.3 Turbulence Models

Various types of turbulent models are used in CFD codes. Fluent provides different turbulent models, as explained in detail in the Ansys Fluent Theory Guide [74]. From historically perspective, the two-equation turbulence models are the most extensively used in industrial applications. These models are based on solution of two transport equations and they model the Reynolds Stresses using the eddy viscosity approach.

In deriving the governing equations in section 3.2, it was not mentioned if the flow was laminar or turbulent. For turbulent flow, the flow behavior is random and chaotic, precluding an efficient calculation of all fluid particles motion. Osborn Reynolds (1894) suggested the turbulent flow can be defined in terms of the mean values of flow properties $\bar{V}, \bar{P}, \bar{e}, \bar{T}$, etc., and some statistical properties of their fluctuations V', P', e', T' , etc., simplifying problem thereby [75]. This simplified formulation is called the Reynolds decomposition. Applying this in equations (3-9), (3-10), and (3-11) will give,

$$\frac{\partial \rho}{\partial t} + \nabla \cdot (\rho (\bar{V} + V')) = 0 \quad (3-12)$$

$$\frac{\partial \rho (\bar{V} + V')}{\partial t} + \nabla \cdot [\rho (\bar{V} + V') (\bar{V} + V')] = -\nabla (\bar{p} + p') + \nabla \cdot \left\{ \mu \left[(\nabla (\bar{V} + V')) + (\nabla (\bar{V} + V'))^T \right] \right\} + \rho g \quad (3-13)$$

$$\frac{\partial}{\partial t} [\rho c_p (\bar{T} + T')] + \nabla \cdot [\rho c_p (\bar{T} + T') (\bar{V} + V')] = \nabla \cdot [k \nabla (\bar{T} + T')] + \bar{\Phi} \quad (3-14)$$

The Reynolds averaged forms of these equations are obtained as,

$$\frac{\partial \rho}{\partial t} + \nabla \cdot (\rho \bar{V}) = 0 \quad (3-15)$$

$$\frac{\partial \rho \bar{V}}{\partial t} + \nabla \cdot (\rho \bar{V} \bar{V}) = -\nabla \bar{p} + \nabla \cdot (\bar{\tau} - \rho \overline{V'V'}) + \rho g \quad (3-16)$$

$$\frac{\partial}{\partial t} (\rho c_p \bar{T}) + \nabla \cdot (\rho c_p \bar{V} \bar{T}) = \nabla \cdot [k \nabla \bar{T} - \rho c_p \overline{V'T'}] + \bar{\Phi} \quad (3-17)$$

The extra averaged products of the fluctuating components due to the non-linear terms are known as Reynolds stress tensor $\tau^R = -\rho \overline{V'V'}$ and turbulent heat flux vector $\bullet q^R = -\rho c_p \overline{V'T'}$, and their expanded forms are given by

$$\tau^R = -\rho \begin{pmatrix} \overline{u'u'} & \overline{u'v'} & \overline{u'w'} \\ \overline{u'v'} & \overline{v'v'} & \overline{v'w'} \\ \overline{u'w'} & \overline{v'w'} & \overline{w'w'} \end{pmatrix}, \quad \bullet q^R = -\rho c_p \begin{pmatrix} \overline{u'T'} \\ \overline{v'T'} \\ \overline{w'T'} \end{pmatrix} \quad (3-18)$$

These new unknowns need other equations to specify and model them in terms of mean flow quantities, in order to close the open set of governing equations. There are four main categories of these models: algebraic (Zero-Equation) models, one-Equation models, two-Equation models, and second-order closure models.

3.3.1 Boussinesq Hypothesis

Boussinesq hypothesis relates the Reynolds stresses to the mean velocity gradients [69,76], so that the equation for incompressible flows becomes:

$$\tau^R = -\rho \overline{V'V'} = \mu_t (\nabla V + \nabla V^T) - 2/3 \rho k I \quad (3-19)$$

where μ_t is the turbulent eddy viscosity, and k is the turbulent kinetic energy defined as $k = 1/2 \overline{V'V'}$.

Similarly, the turbulent thermal fluxes are considered in equivalence with Fourier's law as

$$\mathbf{q}^R = -\rho c_p \overline{V'T'} = k_t \nabla T \quad (3-20)$$

where k_t is the turbulent thermal diffusivity.

3.3.2 The Shear Stress Transport (SST) k - ω Model

The simulations in this study were done using the *SST* k - ω model, combining the k - ε model in the free-stream region and k - ω model in the near-wall region, in order to take benefits of their advantages. The *SST* k - ω model includes some modifications to the standard k - ω model that makes it more accurate and reliable for a more comprehensive class of flows when two transport equations are solved to determine the two large turbulence scales (the turbulent kinetic energy k and the specific dissipation rate ω) [69,74]. Many researches show the accuracy of this turbulence model to simulate various ABL and predict pressures on building as in [9,77]. The two transport equations for this model are written as follows:

$$\frac{\partial \rho k}{\partial t} + \nabla \cdot (\rho \vec{V} k) = \nabla \cdot (\mu_{eff,k} \nabla k) + \tilde{G}_k - Y_k \quad (3-21)$$

$$\frac{\partial \rho \omega}{\partial t} + \nabla \cdot (\rho \vec{V} \omega) = \nabla \cdot (\mu_{eff,\omega} \nabla \omega) + \tilde{G}_\omega - Y_\omega + D_w \quad (3-22)$$

where $\omega = k/\varepsilon$, it is the rate at which turbulence kinetic energy is transformed to internal thermal energy per unit volume and time, and it is better qualified for predicting separated flows. ε is the rate of dissipation of turbulence kinetic energy per unit mass due to viscous stresses, formed as

$$\varepsilon = \frac{1}{2} \frac{\mu}{\rho} \left(\nabla \vec{V}' + (\nabla \vec{V}')^T \right) : \left(\nabla \vec{V}' + (\nabla \vec{V}')^T \right) \quad (3-23)$$

In these two equations, $\mu_{eff,k}$, $\mu_{eff,\omega}$ are the effective diffusivity of k and ω , respectively. \tilde{G}_k is the generation or production of turbulence kinetic energy due to mean velocity gradients, and \tilde{G}_ω is the production of ω . Y_k and Y_ω are the dissipation of k and ω due to turbulence. D_w is the cross-diffusion term.

3.3.2.1 Modeling the Effective Diffusivity

$$\mu_{eff,k} = \mu + \frac{\mu_t}{\sigma_k} \quad (3-24)$$

$$\mu_{eff,k} = \mu + \frac{\mu_t}{\tilde{\sigma}_\omega} \quad (3-25)$$

where the turbulent viscosity μ_t is computed as follows:

$$\mu_t = \frac{\rho k}{\omega} \frac{1}{\text{Max} \left[\frac{1}{\alpha^*}, \frac{S_t F_2}{a_1 \omega} \right]} \quad (3-26)$$

and $\tilde{\sigma}_k, \tilde{\sigma}_\omega$ are the turbulent Prandtl numbers for k and ω , respectively, they are computed as:

$$\tilde{\sigma}_k = \frac{1}{F_1 / \sigma_{k,1} + (1 - F_1) / \sigma_{k,2}} \quad (3-27)$$

$$\tilde{\sigma}_\omega = \frac{1}{F_1 / \sigma_{\omega,1} + (1 - F_1) / \sigma_{\omega,2}} \quad (3-28)$$

In equation (3-26): $a_1 = 0.31$, and S_t is the magnitude of the strain rate defined by

$$S_t = 1/2 (\nabla \vec{V} + \nabla \vec{V}^T) \quad (3-29)$$

The coefficient α^* damps the turbulent viscosity causing a low-Reynolds number correction. It is given by

$$\alpha^* = \alpha_\infty^* \left[\frac{\alpha_0^* + Re_t / R_k}{1 + Re_t / R_k} \right] \quad (3-30)$$

where $\alpha_\infty^* = 1$, $\alpha_0^* = 0.024$, $Re_t = \rho k / \mu \omega$, and $R_k = 6$.

The blending function F_2 given as,

$$F_2 = \tanh(\gamma_2^2) \quad (3-31)$$

where

$$\gamma_2 = \max \left[2 \frac{\sqrt{k}}{0.09 \omega y}, \frac{500 \mu}{\rho y^2 \omega} \right] \quad (3-32)$$

and y is the distance to the next wall.

Moreover, in equations (3-27) and (3-28): The blending function F_1 given as,

$$F_1 = \tanh(\gamma_1^4) \quad (3-33)$$

where

$$\gamma_1 = \min \left[\max \left[\frac{\sqrt{k}}{0.09 \omega y}, \frac{500 \mu}{\rho y^2 \omega} \right], \frac{4 \rho k}{\sigma_{\omega,2} D_\omega^+ y^2} \right] \quad (3-34)$$

$$D_\omega^+ = \max \left[2 \rho \frac{1}{\sigma_{\omega,2}} \frac{1}{\omega} \nabla k \cdot \nabla \omega, 10^{-10} \right]$$

and the model constants are $\sigma_{k,1} = 1.176$, $\sigma_{k,2} = 1$, $\sigma_{\omega,1} = 2$, and $\sigma_{\omega,2} = 1.168$.

3.3.2.2 Modeling the Turbulence Production

The term \tilde{G}_k is described as:

$$\tilde{G}_k = \min(G_k, 10\rho\beta^*k\omega) \quad (3-35)$$

where the G_k for incompressible flow can be obtained by

$$G_k = \mu_t \Phi \quad (3-36)$$

Here, Φ is computed from equation (3-8) and β^* is given by

$$\beta^* = \beta_i^* [1 + \zeta^* F(M_t)] \quad (3-37)$$

$$\beta_i^* = \beta_\infty^* \left[\frac{4/5 + (Re_t / R_\beta)^4}{1 + (Re_t / R_\beta)^4} \right] \quad (3-38)$$

where $F(M_t)$ is the compressibility function, which is zero for incompressible flow, so $\beta^* = \beta_i^* = \beta_\infty^* = 0.09$.

The term \tilde{G}_ω is defined as:

$$\tilde{G}_\omega = \frac{\rho\alpha}{\mu_t} \tilde{G}_k \quad (3-39)$$

where

$$\alpha = \frac{\alpha_\infty}{\alpha^*} \left[\frac{\alpha_0 + Re_t / R_\omega}{1 + Re_t / R_\omega} \right] \quad (3-40)$$

and $R_\omega=2.95$, $\alpha_0=1/9$, α^* and Re_t are given by equation (3-30), and α_∞ is defined as

$$\alpha_\infty = F_1\alpha_{\infty,1} + (1 - F_1)\alpha_{\infty,2} \quad (3-41)$$

where

$$\alpha_{\infty,1} = \frac{\beta_{i,1}}{\beta_\infty^*} - \frac{\kappa^2}{\sigma_{\omega,1}\sqrt{\beta_\infty^*}} \quad (3-42)$$

$$\alpha_{\infty,2} = \frac{\beta_{i,2}}{\beta_\infty^*} - \frac{\kappa^2}{\sigma_{\omega,2}\sqrt{\beta_\infty^*}} \quad (3-43)$$

where $\kappa=0.41$, $\beta_{i,1}=0.075$, and $\beta_{i,2}=0.0828$.

3.3.2.3 Modeling the Turbulence Dissipation

The term Y_k is defined as:

$$Y_k = \rho\beta^*k\omega \quad (3-44)$$

The term Y_ω is defined as:

$$Y_\omega = \rho \beta \omega^2 \quad (3-45)$$

where $\beta = \beta_i$ which is given by

$$\beta_i = F_1 \beta_{i,1} + (1 - F_1) \beta_{i,2} \quad (3-46)$$

3.3.2.4 Cross-Diffusion Modification

The blending of the k - ε model with the k - ω model leads to introduce a cross-diffusion term D_ω , which is defined as

$$D_\omega = 2(1 - F_1) \rho \frac{1}{\sigma_{\omega,2}} \frac{1}{\omega} \nabla k \cdot \nabla \omega \quad (3-47)$$

In addition, in the *SST* k - ω model, the turbulent thermal conductivity in equation (3-20) is computed as:

$$k_t = \frac{\mu_t}{Pr_t} \quad (3-48)$$

where $Pr_t = 0.9$.

3.3.3 General Conservation Equation or General Scalar Transport Equation

The general scalar equation is the equation that can denote any of the conservation equations or turbulence transport equations [69,74,76]. The equations (3-15), (3-15), (3-16), (3-17), (3-21), and (3-22) can be expressed in general equation for a scalar property ϕ as

$$\underbrace{\frac{\partial \rho \phi}{\partial t}}_{\text{temporal term}} + \underbrace{\nabla \cdot (\rho \vec{V} \phi)}_{\text{convection term}} = \underbrace{\nabla \cdot (\Gamma^\phi \nabla \phi)}_{\text{diffusion term}} + \underbrace{S_\phi}_{\text{source term}} \quad (3-49)$$

where ϕ denotes the unknown variables u , v , w , T , k , ω , etc., Γ^ϕ is diffusion coefficient for ϕ , $\nabla \phi$ is the gradient of ϕ , and S_ϕ is the source of ϕ per unit volume.

This equation is used for computational procedures in the FVM to develop CFD codes by concentrating on the general equation instead of the individual equations representing conservation laws.

3.4 Numerical Solution Methodology

Ansys Fluent is solving the integral equations of conservation laws and other scalars such as turbulence using the FVM technique comprising the following steps:

1. Division of the domain into discrete elements to construct the mesh.
2. Integration of the equations over each element to form a set of algebraic equations for the discrete dependent variables, i.e. “unknowns”: velocities, pressures, temperatures, and other conserved scalars.
3. Linearization of discretized equations and solving the resulting linear equation system to calculate updated values of dependent variables.

3.4.1 The Density-Based Solver

In Ansys Fluent, the density-based solver technology is used in this study to solve the coupled governing equations simultaneously and afterward to solve the turbulence equations sequentially, [74]. Due to the non-linearity of the governing equations, several iterations must be performed until convergence criteria are met. The solution steps of every one iteration are shown in Figure 3.1.

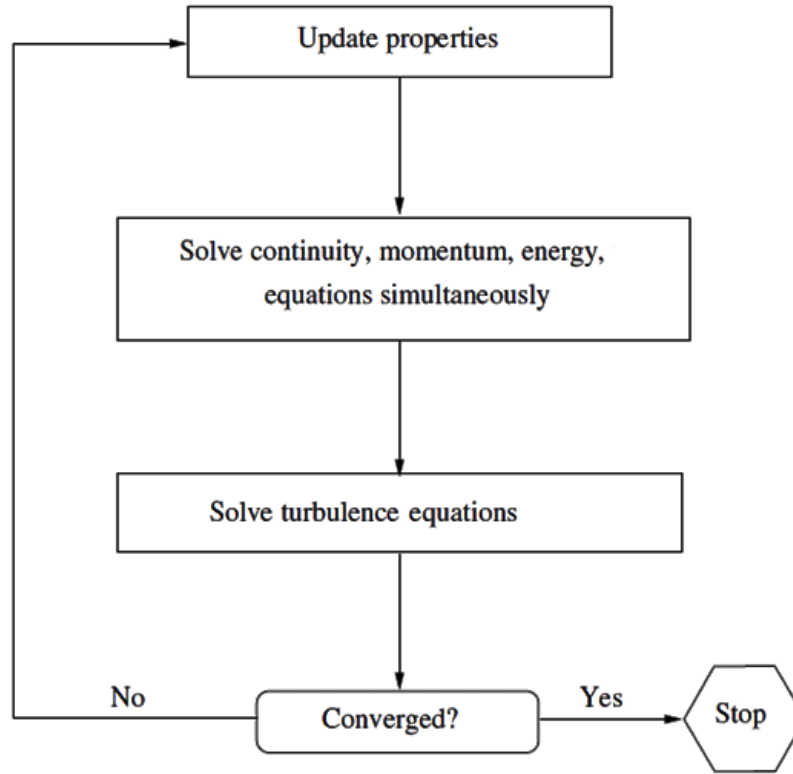


Figure 3.1 Illustration of the density-based solver

Implicit formulation was used to linearize the non-linear governing equations, applied to the coupled set of governing equations. This process will result in a linear equations system with N equations, where N is the number of coupled equations in the set, which are solved by symmetric block Gauss-Seidel in conjunction with an algebraic multi-grid (AMG) method. The transport equations for extra scalars such as turbulence are linearized and solved implicitly using the method described in section 3.4.2 below.

3.4.2 The Discretization of the General Scalar Transport Equation

After discretization of the solution domain into a finite number of discrete regions, called control volumes or cells, the general scalar transport equation is discretizing over each cell in the computational domain to result an algebraic equation that links the value of a variable in a cell to the values of the variable in the neighboring cells.

The process of equation discretization starts by integrating equation (3-49) over a cell that allows recovering its integral balance form [74], which is termed as

$$\int_V \frac{\partial \rho \phi}{\partial t} .dV + \oint \rho \vec{V} \phi . d\vec{A} = \oint \Gamma^\phi \nabla \phi . d\vec{A} + \int_V S_\phi .dV \quad (3-50)$$

where \vec{A} is the surface area vector, and V is the cell volume.

This equation is employed for each cell in the computational domain. An example of such a cell is the two-dimensional triangular shape is shown in Figure 3.2. Discretization of Equation (3-50) on a certain cell yield to

$$\frac{\partial \rho \phi}{\partial t} V + \sum_f^{N_{faces}} \rho_f \vec{V}_f \phi_f . \vec{A}_f = \sum_f^{N_{faces}} \Gamma^\phi \nabla \phi_f . \vec{A}_f + S_\phi .V \quad (3-51)$$

where

N_{faces} -is the number of faces enclosing cell,
 ϕ_f -is the value of ϕ at the center of the face f ,
 $\rho_f \vec{V}_f \phi_f$ -is the mass flux through the face,
 \vec{A}_f -is the area normal vector of face f , $|A| = |A_x \hat{i} + A_y \hat{j} + A_z \hat{k}|$ in 3D,
 $\nabla \phi_f$ -is the gradient of ϕ at face f ,
 V -is the cell volume.

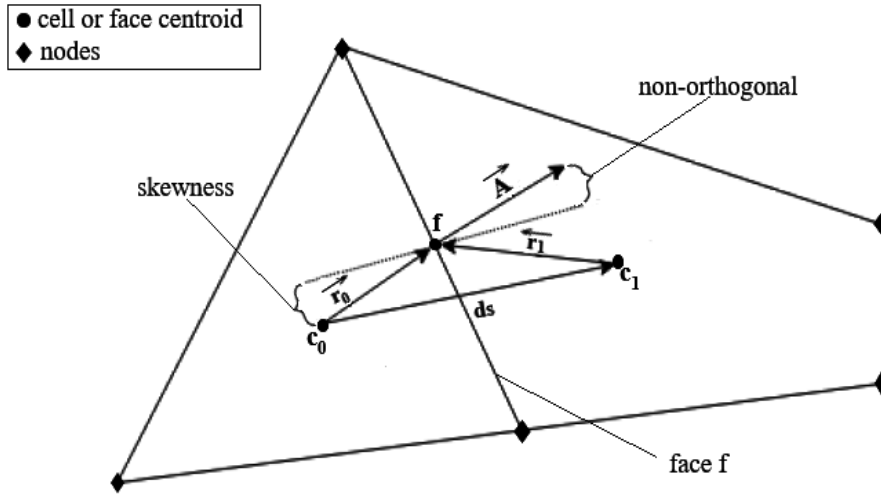


Figure 3.2 Adjacent Cells c_0 and c_1 with Vectors

3.4.2.1 Discretization of the Temporal Term

The spatial discretization for the time-dependent equations is identical to the steady-state case. Discretization in time uses integration of each term in the equations over a time step Δt .

A general expression for the time derivative of a variable ϕ is defined as follows:

$$\frac{\partial \phi}{\partial t} = F(\phi) \tag{3-52}$$

where function F includes any discretization in space. If the time derivative is discretized using implicit time integration, the first-order accurate discretization in time is given by:

$$\frac{\phi^{n+1} - \phi^n}{\Delta t} = F(\phi^{n+1}) \tag{3-53}$$

where $n+1$ is the next time level value, $t + \Delta t$, and n is the current time level value, t .

The value of ϕ^{n+1} in a given cell is interrelated to values of ϕ^{n+1} in neighboring cells through $F(\phi^{n+1})$,

$$\phi^{n+1} = \phi^n + \Delta t F(\phi^{n+1}) \tag{3-54}$$

Equation (3-54) can be solved iteratively through the time domain in unconditionally stable concerning time step size.

3.4.2.2 Discretization of the Convection Term

The discrete values of scalar ϕ are stored by default at the centers of the cells (c_0 and c_1 in Figure 3.2) in Ansys Fluent, so the face values ϕ_f for the convection term in equation (3-51) are need to be interpolated from the cell center values. That is obtained using an upwind scheme.

Several upwind schemes are available in Fluent; in general upwinding means that the face value ϕ_f is calculated from quantities in the cell upstream in respect to the normal velocity direction. For triangular and tetrahedral meshes, the second-order discretization will provide better results since the flow is never aligned with the mesh. Second-Order Upwind Scheme was selected to compute the face values using the following expression:

$$\phi_{f,SOU} = \phi + \nabla \phi \cdot \vec{r} \quad (3-55)$$

where ϕ and $\nabla \phi$ are the cell-centered value and its gradient within the upstream cell, and \vec{r} is the displacement vector from the upstream cell centroid to the face centroid.

Gradients are required not just to calculate a scalar at the cell faces, but also to calculate secondary diffusion terms and velocity derivatives. The gradient $\nabla \phi$ is employed to discretize both the convection and diffusion terms within the flow conservation equations. The gradients were calculated at the cell center using the Green-Gauss theorem as follows:

$$\nabla \phi = \frac{1}{V} \sum_f \bar{\phi}_f \vec{A}_f \quad (3-56)$$

where $\bar{\phi}_f$ is the value of ϕ at the cell face centroid, and computed by the arithmetic average of the nodal values on the face (this is called Green-Gauss Node-Based Gradient Evaluation),

$$\bar{\phi}_f = \frac{1}{N_f} \sum_n^{N_f} \phi_n \quad (3-57)$$

where N_f is the number of nodes on the face, and $\bar{\phi}_n$ is formed from the weighted average of the cell values surrounding the nodes.

The use of the node-based gradient, particularly in irregular (skewed and non-orthogonally cells) unstructured meshes, is more accurate than other Green-Gauss gradients.

3.4.2.3 Discretization of the Diffusion Term

In the unstructured mesh, as shown in Figure 3.2, the non-orthogonal is the angle between the face normal vector \vec{A}_f and the element center-to-center vector \vec{ds} , and the skewness is the distance between the face center f and the element center-to-center vector \vec{ds} .

These metrics can lead to a loss in solution accuracy if not adequately handled because of their effect on calculating the projection of the gradient over the normal face area vector through a given face f , which is attendant to the diffusive term of a transport equation.

For equation (3-51) in the discretized diffusion term, the gradient along the face normal direction is calculated by

$$\nabla \phi_f = \frac{(\phi_1 - \phi_0)}{ds} \frac{\vec{A}}{A \cdot \vec{e}_s} + \left(\bar{\nabla} \phi - \bar{\nabla} \phi \cdot \vec{e}_s \frac{\vec{A}}{A \cdot \vec{e}_s} \right) \quad (3-58)$$

where ds is the distance between the cell centroids, \vec{e}_s is the unit normal vector directed from cell c_0 to c_1 , and $\bar{\nabla} \phi$ is the average of the gradients at the two adjacent cells (the gradient for each cell can be computed from equation (3-56)). This approximation will preserve the second order of accuracy [74,78].

3.4.2.4 Discretization of the Source Term

All terms of discretized equation that cannot be written as convection or diffusion terms are treated as sources. These source terms manipulate the physics of the problem and the numerical

$$\frac{\partial}{\partial t} \int_V W \cdot dV + \oint (F - G) \cdot dA = \int_V H \cdot dV \quad (3-63)$$

where W , F , and G are defined as

$$W = \begin{Bmatrix} \rho \\ \rho u \\ \rho v \\ \rho w \\ \rho e \end{Bmatrix}, \quad F = \begin{Bmatrix} \rho u \\ \rho u u + P \hat{i} \\ \rho u v + P \hat{j} \\ \rho u w + P \hat{k} \\ \rho u e + P u \end{Bmatrix}, \quad G = \begin{Bmatrix} 0 \\ \tau_{xi} \\ \tau_{yi} \\ \tau_{zi} \\ \tau_{ij} u_j + q \end{Bmatrix} \quad (3-64)$$

with the total energy e correlated to the total enthalpy h by $e = h - p/\rho$, and the vector H comprises energy sources and body forces.

The Navier-Stokes equations, in equation form (3-63), become (numerically) very stiff at low Mach number and also for incompressible flows due to the disparity between the fluid velocity and speed of sound, [74]. This issue was resolved in density-based solver by using time-derivative preconditioning technique to provide an efficient solution of flows at all speeds, both compressible and incompressible. In this technique, the time-derivative term in equation (3-63) is modified by pre-multiplying it with a preconditioning matrix, providing the same effect of re-scaling the acoustic speed (eigenvalue) of the system of equations to reduce the numerical stiffness encountered in low Mach numbers and incompressible flow. Thus, the preconditioned system in conservation form becomes

$$\Gamma \frac{\partial}{\partial t} \int_V Q \cdot dV + \oint (F - G) \cdot dA = \int_V H \cdot dV \quad (3-65)$$

where Q is the vector $\{P, u, v, w, T\}^T$ and Γ is the preconditioning matrix given by:

$$\Gamma = \begin{bmatrix} \Theta & 0 & 0 & 0 & \rho_T \\ \Theta u & \rho & 0 & 0 & \rho_T u \\ \Theta v & 0 & \rho & 0 & \rho_T v \\ \Theta w & 0 & 0 & \rho & \rho_T w \\ \Theta h - \delta & \rho u & \rho v & \rho w & \rho_T h + \rho C_p \end{bmatrix} \quad (3-66)$$

For an incompressible fluid $\delta = 0$, ρ_T is the derivative of density with respect to temperature at constant pressure, and the parameter Θ is defined as

$$\Theta = \left(\frac{1}{U_r^2} - \frac{\rho_T}{\rho C_p} \right) \quad (3-67)$$

here, U_r is the reference velocity that is chosen locally.

However, the resultant eigenvalues of the preconditioned system (equation (3-65)) are given by

$$\lambda \left(\Gamma^{-1} \frac{\partial F}{\partial Q} \right) = u, u, u, u' + c', u' + c' \quad (3-68)$$

where

$$u = u \cdot \hat{n}, \quad u' = u(1 - \xi), \quad c' = \sqrt{\xi^2 u^2 + U_r^2}, \quad \xi = (1 - \zeta U_r^2)/2, \quad \zeta = \left(\rho_p + \frac{\rho_T}{\rho C_p} \right)$$

For an ideal gas, $\zeta = (\gamma RT)^{-1} = 1/c^2$. Thus, when $U_r = c$ (the sonic speed), $\xi = 0$ and the preconditioned system's eigenvalues take their traditional form, $u \pm c$. At low speed, as $U_r \rightarrow 0$, $\xi \rightarrow 1/2$, all eigenvalues have values of the same order as u . For constant-density flows, $\zeta \rightarrow 0$, $\xi = 1/2$, independent of the values of U_r . If the reference velocity is of the same order as the local velocity, all eigenvalues are of the order u . Therefore, the eigenvalues of preconditioned system is well-conditioned at all speeds.

3.4.3.2 The Discretization of the General Vector Equation

The governing equation (3-65) is discretized in space using a FV technique, with the physical domain is subdivided into cells, and the integral equations employed to each cell. Thus moderated to the following system

$$\Gamma \frac{\partial Q}{\partial t} \mathbf{V} + \sum_f^{N_{faces}} (\hat{F}_f - \hat{G}_f) = H \mathbf{V} \quad (3-69)$$

where \hat{F}_f and \hat{G}_f are the convective and diffusive face fluxes [79–81].

3.4.3.3 Spatial Discretization

The solution vector Q_f used to evaluate the fluxes at cell faces is computed using equations (3-55), (3-56), and (3-57) by replacing ϕ by Q .

The diffusive face flux \hat{G}_f appearing in equation (3-69) can be written in terms of spatial gradients of the primary variables as follows:

$$\hat{G}_f = R_{ij} \cdot \nabla Q_f \quad (3-70)$$

where R_{ij} are sparse matrices containing face area projections, and viscous and thermal diffusion coefficients.

$$R_{ij} = \begin{bmatrix} R_{xx} & R_{yx} & R_{zx} \\ R_{xy} & R_{yy} & R_{zy} \\ R_{xz} & R_{yz} & R_{zz} \end{bmatrix} \quad (3-71)$$

Also, ∇Q_f is computed from equation (3-58) by replacing ϕ by Q .

The convective fluxes appearing in equation (3-69) are assessed by a standard upwind flux difference splitting. This concedes that F comprises information propagating through the domain with speed and direction according to the system's eigenvalues. By separating F into two parts, each will contain information traveling in a particular direction, while upwind is differencing the separated fluxes consistently with their corresponding eigenvalues. Therefore, the following expression was obtained for the flux \hat{F}_f at each face:

$$\hat{F}_f = \frac{1}{2} (F_R - F_L) \cdot \vec{A}_f - \frac{1}{2} \Gamma |\hat{A}| \delta Q \quad (3-72)$$

Where $\delta Q = Q_R - Q_L$, $F_R = F(Q_R)$ and $F_L = F(Q_L)$ are calculated using the reconstructed solution

vectors Q_R and Q_L on the "right" and "left" side of the face. The matrix $|\hat{A}|$ is defined by

$$|\hat{A}| = M |A| M^{-1} \quad (3-73)$$

where

$$A = \text{diag}(u, u, u, u' + c', u' + c') \quad (3-74)$$

and M is the modal matrix that diagonalizes $\Gamma^{-1}A$, where A is the inviscid flux Jacobian

$$A = \frac{\partial F}{\partial Q} \cdot \vec{A}_f \quad (3-75)$$

For the non-preconditioned system and an ideal gas, equation (3-72) reduces to Roe's flux-difference splitting when Roe-averaged values are used to evaluate $\Gamma |\hat{A}|$ arithmetic averaging of states Q_R , and Q_L .

In the given form, equation (3-72) can be interpreted as a second-order central-difference plus added matrix dissipation [74,82–85].

3.4.3.4 Linearization

In Ansys Fluent, the coupled set of equation (3-65) is discretized in time for both steady and unsteady state calculations. In the steady state case, the time marching progresses until a steady-state solution is obtained. Discretization of the coupled equations in time is made by applying implicit or explicit time-marching algorithm.

In the implicit time-marching algorithm, as used in this study, Euler implicit discretization in time is merged with a Newton-type linearization of the fluxes to yield the following linearized system in the following delta form

$$\left[D + \sum_f^{N_{\text{faces}}} S_{f,j} \right] \Delta Q^{n+1} = -R^n \quad (3-76)$$

where $\Delta Q^{n+1} = Q^{n+1} - Q^n$. The center and off-diagonal coefficient matrices, D and $S_{f,j}$ are given by

$$D = \frac{V}{\Delta t} \Gamma + \sum_f^{N_{\text{faces}}} S_{f,i} \quad (3-77)$$

$$S_{f,j} = \left(\frac{\partial F_f}{\partial Q_j} + \frac{\partial G_f}{\partial Q_j} \right) A_f \quad (3-78)$$

and the residual vector R^n and time step Δt are defined as

$$R^n = \sum_f^{N_{\text{faces}}} (F(Q^n) - G(Q^n)) \cdot A_f - HV \quad (3-79)$$

$$\Delta t = \frac{2 CFL V}{\sum_f \lambda_f^{\text{max}} A_f} \quad (3-80)$$

where, the subscript j relates to the index of cell adjacent to cell- i across face- f , and λ_f^{\max} is the maximum of the local eigenvalues expressed by equation (3-68).

Equation (3-76) is solved using Incomplete Lower Upper factorization (ILU) by default or symmetric point Gauss-Seidel algorithm, in combining with an algebraic multi-grid method adapted for coupled sets of equations [74,86,87].

3.4.4 Solution Methods

3.4.4.1 The Multi-grid Methods

Multi-grid methods are designed to accelerate the convergence of the solver by computing corrections on a series of coarse grid levels. They use to reduce the number of iterations and the CPU time needed to reach a converged solution, mainly when the model includes a large number of cells [74,88].

Two multi-grid methods are used in Fluent, the geometric multi-grid (GMG) method, which is also called full-approximation storage (FAS), and the algebraic multi-grid method. GMG method implements by generating several levels of coarse meshes from the original finer mesh generated by users (final mesh) to reducing large wavelength errors on a coarse mesh instead of on the fine mesh since it is more effectively done. However, in AMG, the coarse level equations are produced without the use of any geometry or re-discretization on that level, which gives an advantage to AMG over GMG since no coarse meshes have to be assembled or stored, and no fluxes or source terms require to be assessed on the coarse levels [74,88,89].

These methods are established taking into account that the global error remaining on a fine mesh can be manageable as local error. Since there are fewer coarse cells overall, the global corrections can be communicated more rapidly between adjacent cells. Since calculations with coarser meshes are exponentially cheaper in respect to CPU time and memory storage, there is a possibility for efficient reduction of global error. In this case, the fine-grid relaxation scheme or “smoother” either the point implicit (Gauss-Seidel) or the Incomplete Lower Upper factorization scheme is not mandatory to be particularly effective at reducing global error and can be tuned for efficient reduction of local error [90].

3.4.4.1.1 Geometric Multi-Grid

Ansys Fluent’s work to forming the multi-grid grid hierarchy is simply to coalesce groups of fine level cells to form coarse level cells by agglomerating the cells surrounding a node, as shown in Figure 3.3. Depending on the grid topology, cells with irregular shapes and variable numbers of faces can result in cells [74].

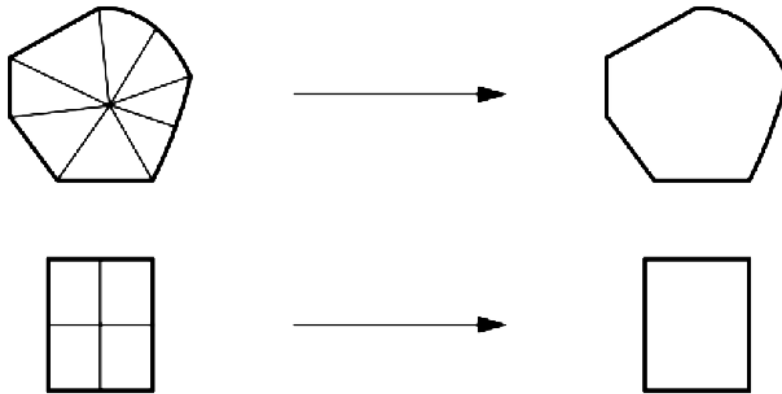


Figure 3.3 Node agglomeration to form coarse grid cells

As an example of the GMG cycles, the three-grid levels algorithm is organized in Figure 3.4 to illustrate the procedure steps in this cycle, which is called the V cycle [90].

1. In the first level, consider the set of discretized linear (or linearized) equations given by equation (3-61), these algebraic equations on the fine level are solved using iterative solver as Gauss-Seidel or ILU, but only to partial convergence. Partial convergence is known as smoothing and performed by one iteration since the overall iteration count is not guided by the solver but rather by the multi-grid treatment of the errors. So before the solution has converged, there will be a defect (residual on fine level) $[R]^1$ associated with the approximate solution $[\phi]_s^1$, which computed as

$$[R]^1 = [b] - [A]^1 [\phi]_s^1 \tag{3-81}$$

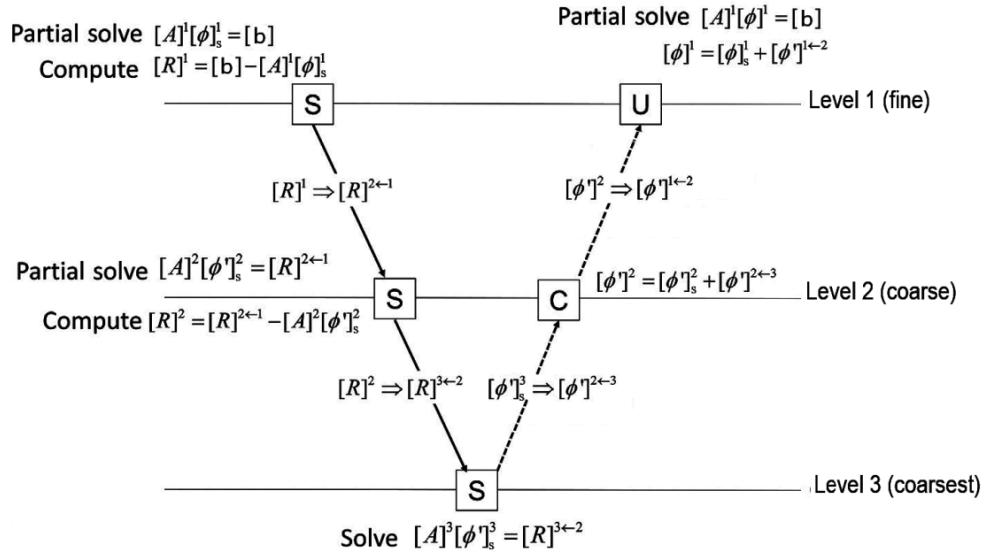


Figure 3.4 The three levels V-cycle GMG Algorithm

“S” denotes the smoothing operation, “C” denotes the error correction operation, and “U” denotes the final solution update

2. In the first way down to the second level, the residual computed on the fine level transfer to the coarse level, the procedure is called restriction. The residual in any coarse level cell is given by the sum of those from the fine level cells it includes. In the forthcoming, the residual transferred from the fine to the coarse level will be indicated by $[R]^{C\leftarrow F}$ (here $[R]^{2\leftarrow 1}$). These residuals are next smoothed on the coarse level using the same iterative solver with the specific aim to reduce the error rapidly. This operation requires the solution of the equation (3-82) to partial convergence.

$$[A]^2 [\phi']_s^2 = [R]^{2\leftarrow 1} \tag{3-82}$$

where $[A]^2$ is the coefficient matrix (coarse level operator) computed from a re-discretization of the governing equations on the coarse level mesh, and $[\phi']_s^2$ is the predicted correction on the coarse mesh. This equation principally represents the linear governing system in correction form. Then residual on the coarse level $[R]^2$ associated with the approximate solution $[\phi']_s^2$, will be computed as

$$[R]^2 = [R]^{2\leftarrow 1} - [A]^2 [\phi']_s^2 \tag{3-83}$$

3. In a second way down to the third level, by the same principles used in step 2, the residual computed on the coarse level transfer to $[R]^{3\leftarrow 2}$ on the coarsest level and coarsest level operator

$[A]^3$ computed on the coarsest mesh. The transferred residuals are then smoothed on the coarsest level using the same iterative solver by solving the equation (3-84) to partial convergence.

$$[A]^3 [\phi']_s^3 = [R]^{3 \leftarrow 2} \tag{3-84}$$

- In the first way up to the second level, the correction $[\phi']_s^3$ obtained on the coarsest level is next transferred to the coarse level. This procedure is known as prolongation, where coarse level corrections $[\phi']^{2 \leftarrow 3}$ are obtained by distance-weighted interpolation of coarsest level values. Then the predicted correction obtained in Step 2 updated by adding to it the coarse level corrections:

$$[\phi']^2 = [\phi']_s^2 + [\phi']^{2 \leftarrow 3} \tag{3-85}$$

- In a second way up to the fine level, the updated correction $[\phi']^2$ obtained on the coarse level is next prolonged to the fine level corrections $[\phi']^{1 \leftarrow 2}$. Then the predicted correction obtained in step 1 updated by adding to it the fine level corrections:

$$[\phi']^1 = [\phi']_s^1 + [\phi']^{1 \leftarrow 2} \tag{3-86}$$

Finally, at the end of this juncture, the updated predicted corrections $[\phi']^1$ are smoothed on the fine level using the same iterative solver and performed by (2 or 3) iteration. This operation called (post-relaxation sweeps) and requires the solution of the equation (3-87),

$$[A]^1 [\phi']^1 = [b] \tag{3-87}$$

- Convergence is evaluated by monitoring the residual computed as on step 1, and if the convergence criterion has not been satisfied, steps 2–6 must be repeated.

Hence, according to the purpose of multi-grid algorithms, the fine level solution will be convergence faster by increasing the number of coarse levels or increasing the number of cycles per level or both. However, the multi-grid cycle can be outlined as a recursive procedure applied at each grid level as it moves through the grid hierarchy. Four types of multi-grid cycles are offered in Ansys Fluent: the V, W, F, and flexible cycles, more details about these cycles can be found in [74].

In the present study, the GMG method was used in solution steering in the density-based implicit solver. Solution steering provides an expert system that will help navigate the flow solution from a starting initial guess to a converged solution with minimum user interaction. As the solver progresses with the solution iteration, specific solver parameters will be adjusted behind the scenes to confirm that a converged solution to a steady state is achievable.

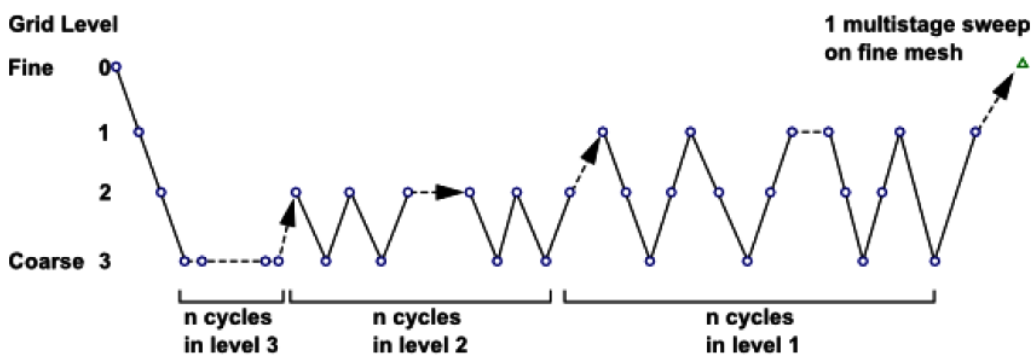


Figure 3.5 Illustration of the FMG Initialization

Solution steering uses a technique known as the full multi-grid (FMG) initialization, as shown in Figure 3.5. At the beginning of its process, the initial solution is restricted all the way down to the coarsest level, where the calculations start. The GMG multi-grid cycle is then applied until a set maximum number of cycles is accessed. Solutions are transferred to successively finer grid levels, and on the finest level, the prolonged solution is used as the premier guess for the start of the iterative process (AMG process) [74].

3.4.4.1.2 Algebraic Multi-Grid

The AMG method takes advantage of the powerful multi-grid idea of targeted decrease of large errors while deleting any connection of the method to the dependent grid so that the method can be used as a plugin-type solver and remarkably attractive for use on unstructured meshes, [77].

The prime step in AMG is that the coarse-grid equivalent equations are constructed from the fine-grid equations at the algebraic equation level by combining (agglomerating) fine-grid equations in some fashion, since the fine-grid equations are our starting point and are always available. In this process, each cell in fine level is grouped with one or more of its “strongest” neighbors, with a preference given to currently ungrouped neighbors.

The AMG algorithm attempts to gather cells into groups of fixed size. In the setting of grouping, strongest denotes to the neighbor j of the current cell i for which the coefficient A_{ij} is largest. For sets of coupled equations, A_{ij} is a block matrix, and the determination of its magnitude is solely taken to be the magnitude of its first element [74].

In Ansys Fluent, inter-level transfer of AMG is accomplished by piecewise constant interpolation and prolongation. The Residuals in any coarse level cell are obtained as on the GMG, while corrections of fine level are given by injection of coarse level values. The coarse level operator A^H is constructed to a sum of diagonal and corresponding off-diagonal blocks for all fine level cells within a group to form the diagonal block of that group’s coarse cell.

3.4.4.2 The Gauss-Seidel Method

This method is used to solve a linear system of equations one at a time, in a sequence. The point Gauss-Seidel method in Ansys Fluent is used as a smoother to solve the scalar AMG system of equations or the coupled AMG system of equations. It implements two sweeps on the unknowns, in forward and backward directions.

In this study, this method was chosen to solve the scalar AMG system, equation (3-61). The forward sweep can be written as:

$$\phi_i^{k+1/2} = \left(b_i - \sum_{j<i} a_{ij} \phi_j^{k+1/2} - \sum_{j>i} a_{ij} \phi_j^k \right) / a_{ij} \quad (i = 1, \dots, N) \quad (3-88)$$

where k and N are the iteration numbers and unknowns, respectively. The forward sweep is followed by a backward sweep, which can be written as:

$$\phi_i^{k+1} = \left(b_i - \sum_{j<i} a_{ij} \phi_j^{k+1/2} - \sum_{j>i} a_{ij} \phi_j^{k+1} \right) / a_{ij} \quad (3-89)$$

Following from equation (3-88) and equation (3-89), symmetric Gauss-Seidel can be given in matrix form as a two-step recursive solution of the system:

$$(D_A + L_A)D_A^{-1}(D_A + U_A)(\phi^{k+1} - \phi^k) = b - A\phi^k \quad (3-90)$$

where D_A , L_A , and U_A represent diagonal, lower tridiagonal, and upper tridiagonal parts of matrix A , respectively.

Symmetric Gauss-Seidel has a slightly limited smoothing rate of residuals between AMG

levels unless the coarsening factor is set to 2.

3.4.4.3 The Incomplete Lower Upper Method

The ILU smoother is using the default smoother to solve the coupled systems, enabling shorter solution times and more robust performance than the Gauss-Seidel smoother. In common, any iteration method can be expressed as

$$M(\phi^{k+1} - \phi^k) = b - A\phi^k \quad (3-91)$$

where matrix M is a specific approximation of the original matrix A from

$$A\phi = b \quad (3-92)$$

Matrix M should be close to the original matrix A , while the calculation of M^{-1} should have a low operation count. Considering matrix M as an incomplete lower upper factorization of the matrix A such that

$$M = LU = (D + L_A)D^{-1}(D + U_A) \quad (3-93)$$

The diagonal matrix D is intended to satisfy the following condition for diagonal D_M of matrix M :

$$D_M = D_A \quad (3-94)$$

In this case, the i th element of the diagonal of D can be calculated using the following expression

$$d_{ii} = a_{ii} - \sum_{j < i} \left(\frac{a_{ij} a_{ji}}{d_{jj}} \right) \quad (3-95)$$

In 3D problems, ILU smoother for block-coupled systems solved by coupled AMG has coarsening factors between 8 and 12 compared to 2 for Gauss-Seidel.

CHAPTER 4: CFD MODELING OF ATMOSPHERIC BOUNDARY LAYER

The numerical analysis by CFD was performed for two types of subsonic wind tunnels with various obstacles and different speeds in their test sections, using the *SST k- ω* turbulence model. The measured velocity profiles within the ABLs generated in both wind tunnels were compared with CFD results for verifications. The provided CFD analysis also evaluated contours of velocity magnitude and eddy viscosity along wind tunnels test sections.

4.1 Wind Tunnels Experiments

The two wind tunnels were chosen for this study, where several tests have been done to simulate different ABLs inside their test sections. The first wind tunnel is the Assiut University wind tunnel, where three types of ABLs have been generated in its test section by three different low speeds for each ABL. The second wind tunnel is the Belgrade University wind tunnel that has generated another type of ABL in the central of its test section at a higher speed.

4.1.1 The Assiut University Wind Tunnel

This wind tunnel has been built in the laboratory of environmental studies and research at the Mechanical Engineering Department of Assiut University, Egypt. It is a subsonic open-loop, low-speed (up to 4 m/s). The wind tunnel construction consists of an upstream settling section (honeycomb and screens), a contraction cone, a heating unit, a second settling section, a boundary layer development section, a test section, a transition and flexible connection, and an axial flow fan, as shown in Figure 4.1.

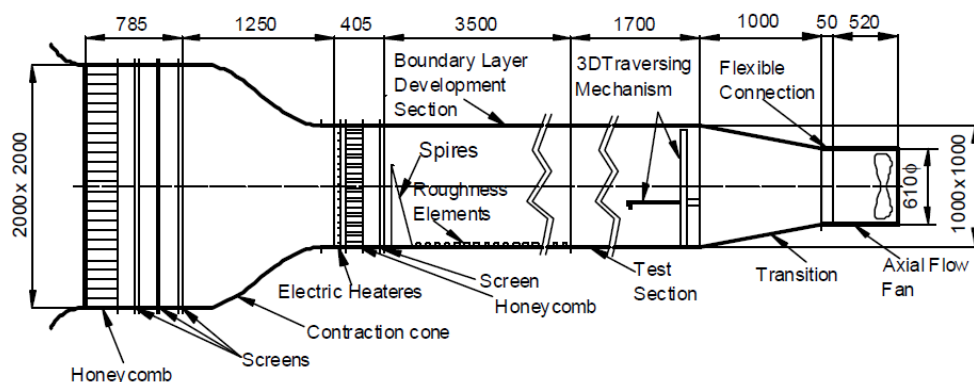


Figure 4.1 Construction components and their details of the Assiut University wind tunnel, all dimensions in mm

The boundary layer development section and the test section have a 1×1 m square cross-section area. The three ABLs were generated along the boundary layer development section: first without using any passive devices, second using three triangular flat spires only, and the third by combining the three spires with 710 cubes (roughness elements), as shown in Figure 4.2. The design and arranging of the spires and roughness elements are described in [91].

The experiments aimed to measure mean vertical velocity distribution for three different fan speeds at varying heights in the middle of the test section, at a distance of 3.6 m from the inlet of the boundary layer development section. These results are obtained in the empty wind tunnel, wind tunnel with spires only, and wind tunnel with the arrangement of spires and arrays of roughness elements.

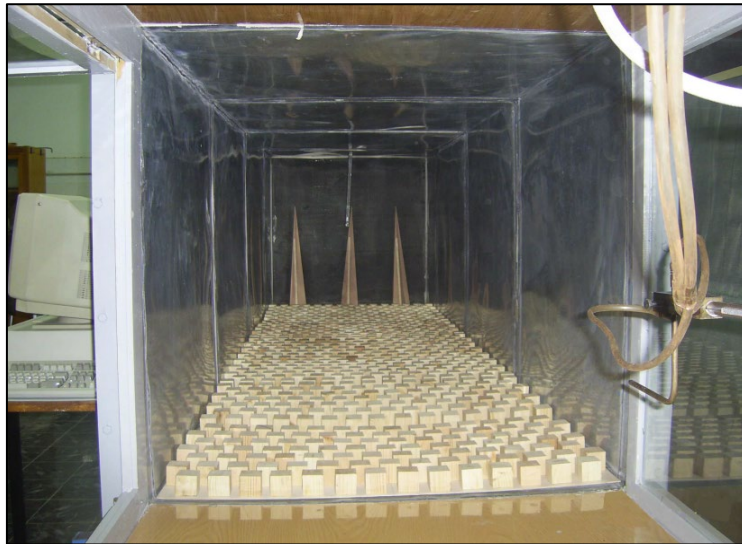


Figure 4.2 Photograph of the boundary layer development section with the passive devices and test section at Assiut University wind tunnel

4.1.2 The Belgrade University Wind Tunnel

This wind tunnel has built at the Aeronautical Institute of the Faculty of Mechanical Engineering, University of Belgrade, which was designed for aeronautical and environmental studies and research. It is of a subsonic closed-loop type, with a max. speed of 60 m/s as applies for the old electrical installation when the tests were accomplished (more details described in [92]). It involves an upstream settling chamber, an effuser, a test section, a small diffuser, corners, a channel, an axial flow fan, and the main diffuser, as shown in Figure 4.3.

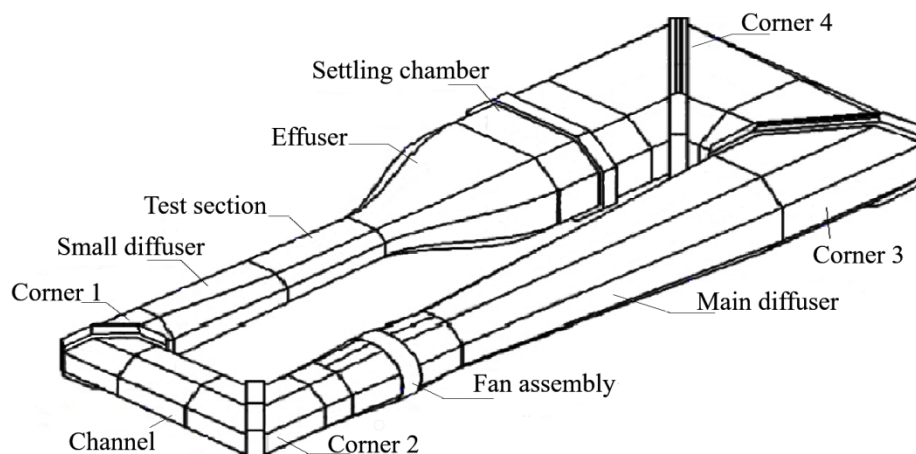


Figure 4.3 Components of the Belgrade University wind tunnel

This wind tunnel test section has an octagonal cross-section 2 m high, 2.8 m wide and 6 m long. The ABL here was generated in the central of the test section using four flat plates (barrier walls), seven semi-elliptical spires, and 1156 small pyramidal elements (roughness elements), as shown in Figure 4.4. All components dimensions of the wind tunnel and the design of the used passive devices are described in [92].

The experimental tests here were carried out to measure mean vertical velocity at different vertical positions from the test section floor, in the middle of its length (3 m from the test section inlet).

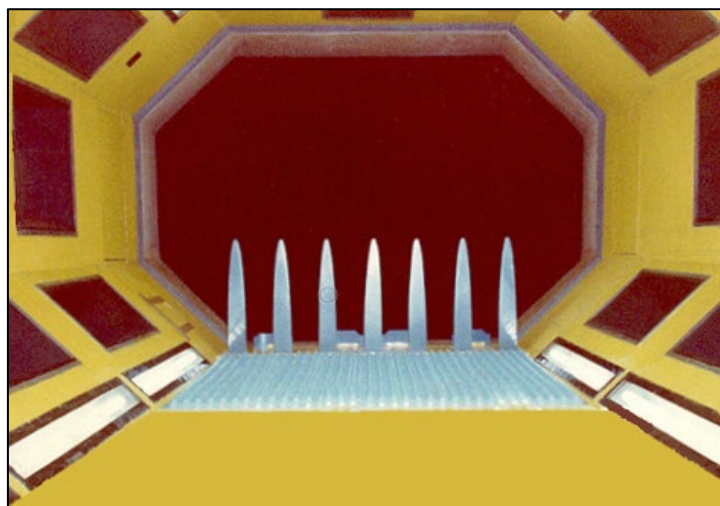


Figure 4.4 Picture of the test section with the passive devices at Belgrade University wind tunnel

4.2 The CFD Simulations and Verifications

In this chapter, the CFD simulations have been done in ANSYS Fluent using 3D analyses with the *SST $k-\omega$* turbulence model. Three cases were modeled and simulated for verifications. Two modeled cases of them for Assuit wind tunnel: spires only case and spires with roughness elements case, while the third case of not using any passive devices was ignored due to developed laminar flow in the test section associated with low speed fan. The third modeled case is with barrier walls with spires and roughness elements at Belgrade University wind tunnel.

4.2.1 Computational Domain and Mesh Configuration

The half of the effuser and test section were modeled at scale 1:1 (i.e., using the actual wind tunnel model dimensions) to achieve proper atmospheric boundary layers simulations by CFD for both wind tunnels because of the vertical symmetry of the flow, as well as to lower the number of mesh elements in the computational domain.

The unstructured meshes were created for all computational domains, as shown in Figure 4.5 and Figure 4.6. More concern was given to a local intensify in the number of elements on the floor of test sections, sharp and elliptical edges of spires, and roughness elements, keeping the total number of elements at moderately low values with adequate mesh quality.

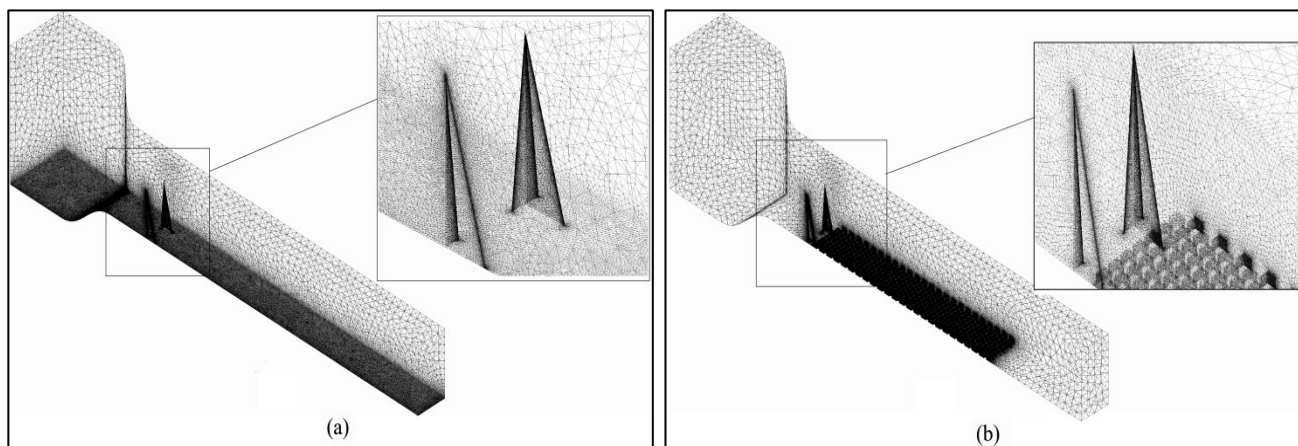


Figure 4.5 The unstructured meshes for two cases tested at the Assuit wind tunnel, (a) – Case of spires only, and (b) – case of spires and surface roughness.

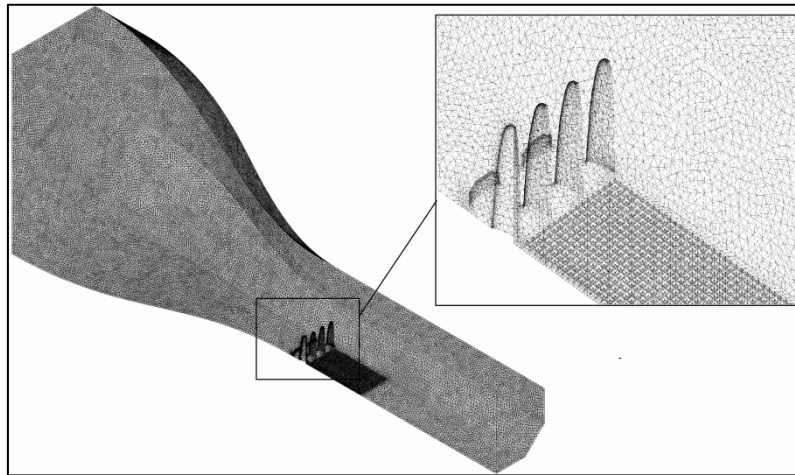


Figure 4.6 The unstructured mesh for the Belgrade wind tunnel model

The computational domain for each case depends on the effuser and test section dimensions with the sizes and shapes of the used passive devices, so the number of mesh elements differs on each computational domain, as presented in Table 4-1.

Table 4-1 The number of mesh elements on every computational domain

computational domains	numbers of mesh elements
Case 1 (spires only at Assiut wind tunnel)	3,600,000
Case 2 (spires and roughness elements at Assiut wind tunnel)	4,800,000
Case 3 (Belgrade wind tunnel)	1,600,000

4.2.2 Setup and Solution

The CFD simulations were done in ANSYS Fluent using 3D steady-state, density-based solver, RANS approach with the *SST $k-\omega$* model as a viscous model that involving curvature correction and production limiter. The fluid was air, and a Sutherland law by three coefficient methods used to describe its viscosity.

The ‘inlet velocity’ boundary condition was set at various velocities at the collector inlet corresponding to measured velocities at the inlet of the wind tunnels test section, considering the equal volume flow rate through the collector. Furthermore, the ‘pressure outlet’ boundary condition was set as zero gauge pressure. Also, the values of turbulence quantities at the boundary were specified uniformly. Since the accurate profiles of these quantities are unknown, turbulent intensity and viscosity ratios were set equal to 1% at the inlet and equal to 10% at the outlet of the computational domain.

Second-order discretization schemes were used for the convective and diffusion terms of the governing equations. Also, Full Multi-Grid solution initialization and solution steering were used to achieve a good initial solution at a low cost, with control of setting the Courant number to achieve the convergence level.

Numerical convergence was attained when the solution monitor for outlet mass flow rate displayed no variation and continued constant observing a significant number of iterations digits.

4.3 Results and Discussion

4.3.1 Comparison of CFD and Wind Tunnel Experiments Results

The CFD result of simulating the ABL presented in this chapter have been compared with the established experimental data for 3 general cases to validate here established computational method over a wide range of subsonic speeds: 1 - 4 m/s in the Assiut University investigations, and 45 m/s in the Belgrade University wind tunnel.

The flow velocities for every case of the Assuit University wind tunnel were acquired through three altered fan speeds of 500, 1000, 1440 rpm during the tests. At 1440 rpm, the maximum flow rate of about 4 m³/s has been reached in the test section with a 1×1 m cross-section, so the corresponding flow speed of the order of 4 m/s.

Figure 4.7 made in Fluent displays the velocity distributions in the symmetry plane for case 1. These contours have been presented to clearly show the flow field domains behind the spires for the three different fan speeds.

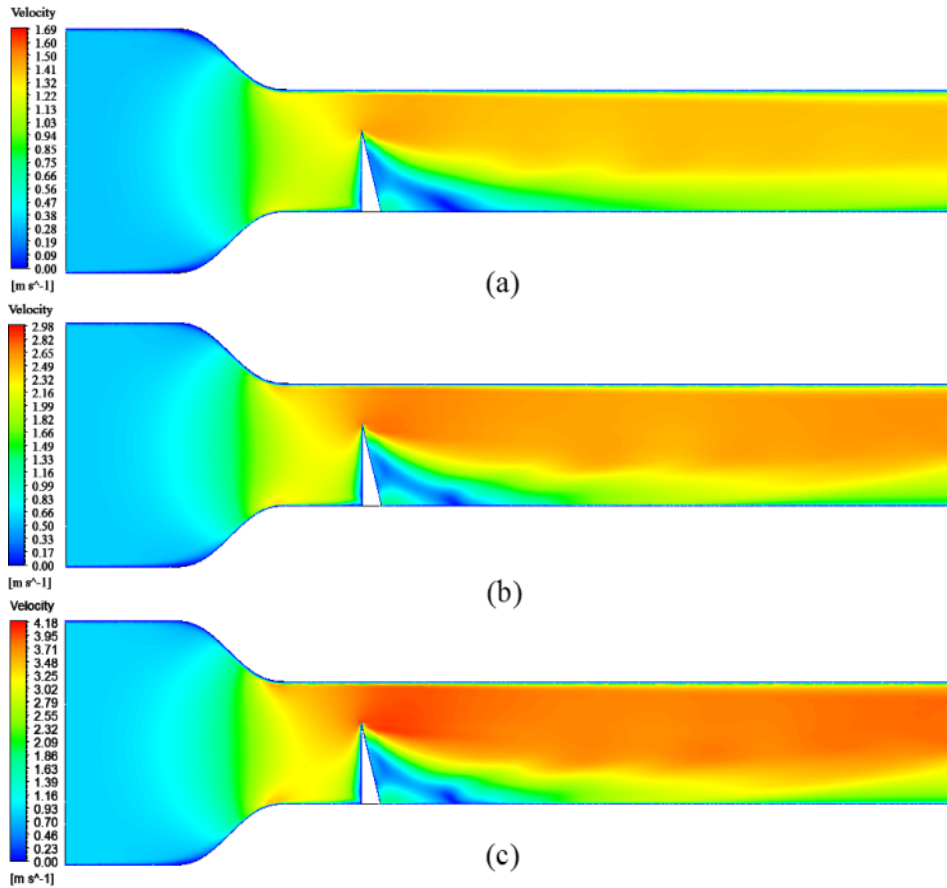


Figure 4.7 Contours of velocity magnitude for case 1, for the three different fan speeds 500, 1000, and 1440 rpm, respectively

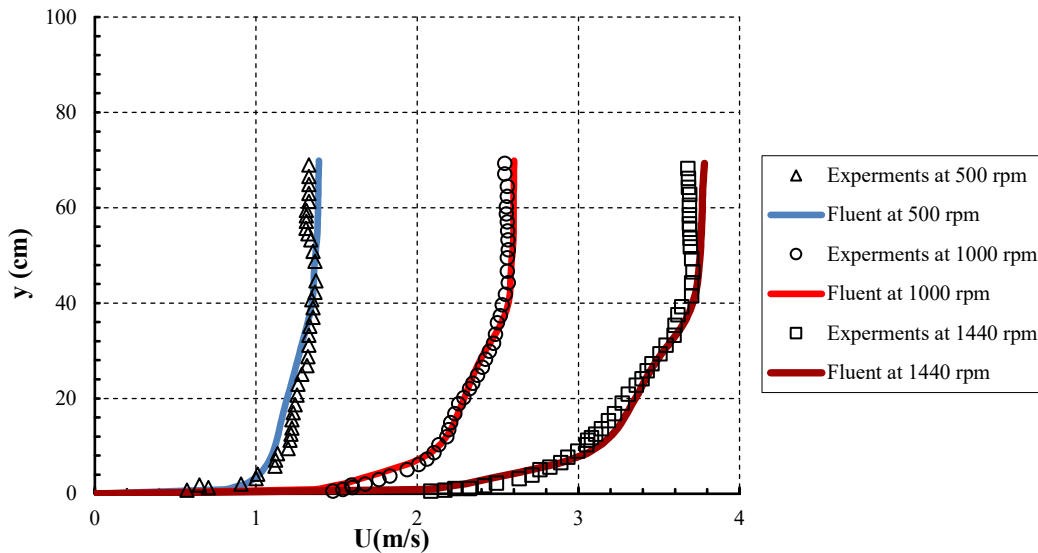


Figure 4.8 Comparisons of mean velocity profiles for case 1, for the three different fan speeds

Figure 4.8 shows the comparison between the simulated and measured vertical velocity at a different height at the test section inlet (i.e., at 3.6 m away from the inlet of the boundary layer development section) for the three fan speeds. In this case, when the only spires were used at the Assuit University wind tunnel, the boundary layer thickness was approximately 35 cm. The velocity profiles show fair agreements excluding the region near the floor wall, where the CFD analyses were performed assuming a smooth wall since no surface roughness value was indicated in actual experiments. This assumption has caused a slight predictable difference between the calculated and measured velocities in that region.

Figure 4.9 displays the velocity magnitude contours in the symmetry plane for case 2, where both spires and roughness elements were used during the experiment. The effect of this combination in the flow field domains behind the spires for the three different fan speeds is shown here.

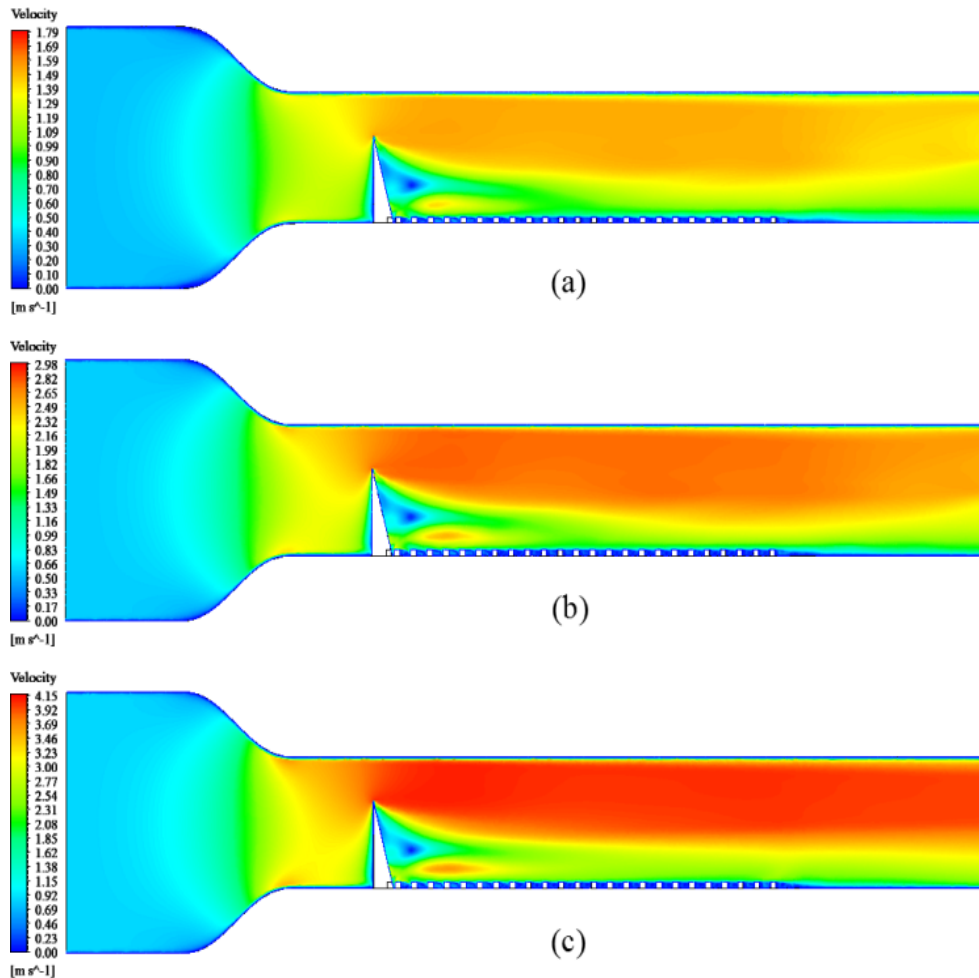


Figure 4.9 Contours of velocity magnitude for case 2, for the three different fan speeds 500, 1000, and 1440 rpm, respectively

Figure 4.10 shows the comparison between the simulated and measured vertical velocity at a different height in the same location at the inlet of the Assuit University wind tunnel test section for the three fan speeds. In this case, the spires with roughness elements were used to generate a thicker boundary layer thickness of about 60 cm. The velocity profiles show fair agreements over the complete profile heights for all three fan speeds. Almost all profiles share the same velocity distributions at all elevations less than 5 cm.

Figure 4.11 displays contours of the mean velocity in several cross-sections at 1440 rpm fan speed for cases 1 and 2. Spire wakes in case 1 are adjacent to the floor, while in case 2, they are detached above the roughness elements to the distance of about 1 m from the development section inlet. The generated boundary layer is more dense and homogeneous in the vicinity of the floor as the flow moves down the development section.

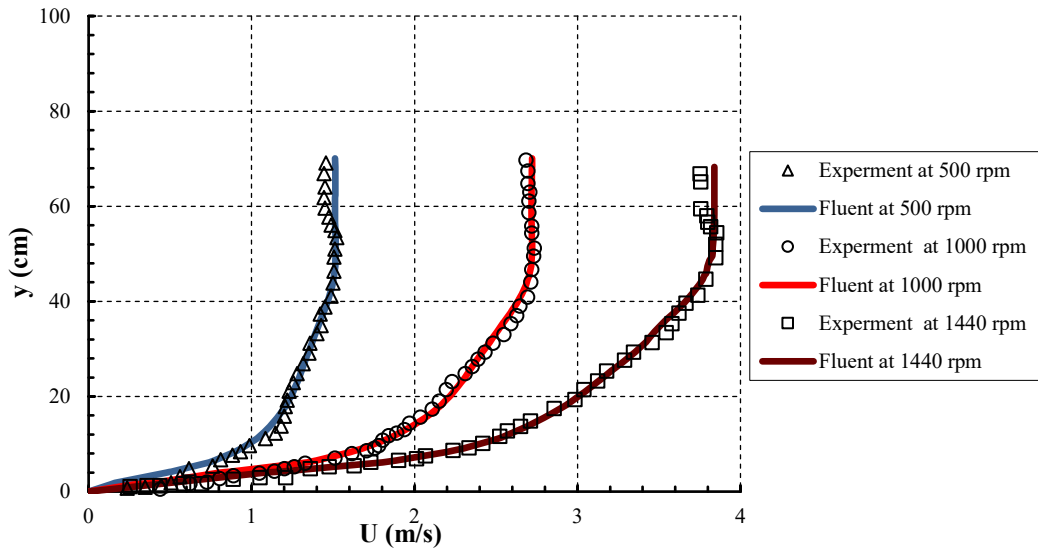


Figure 4.10 Comparisons of mean velocity profiles for case 2, for the three different fan speeds

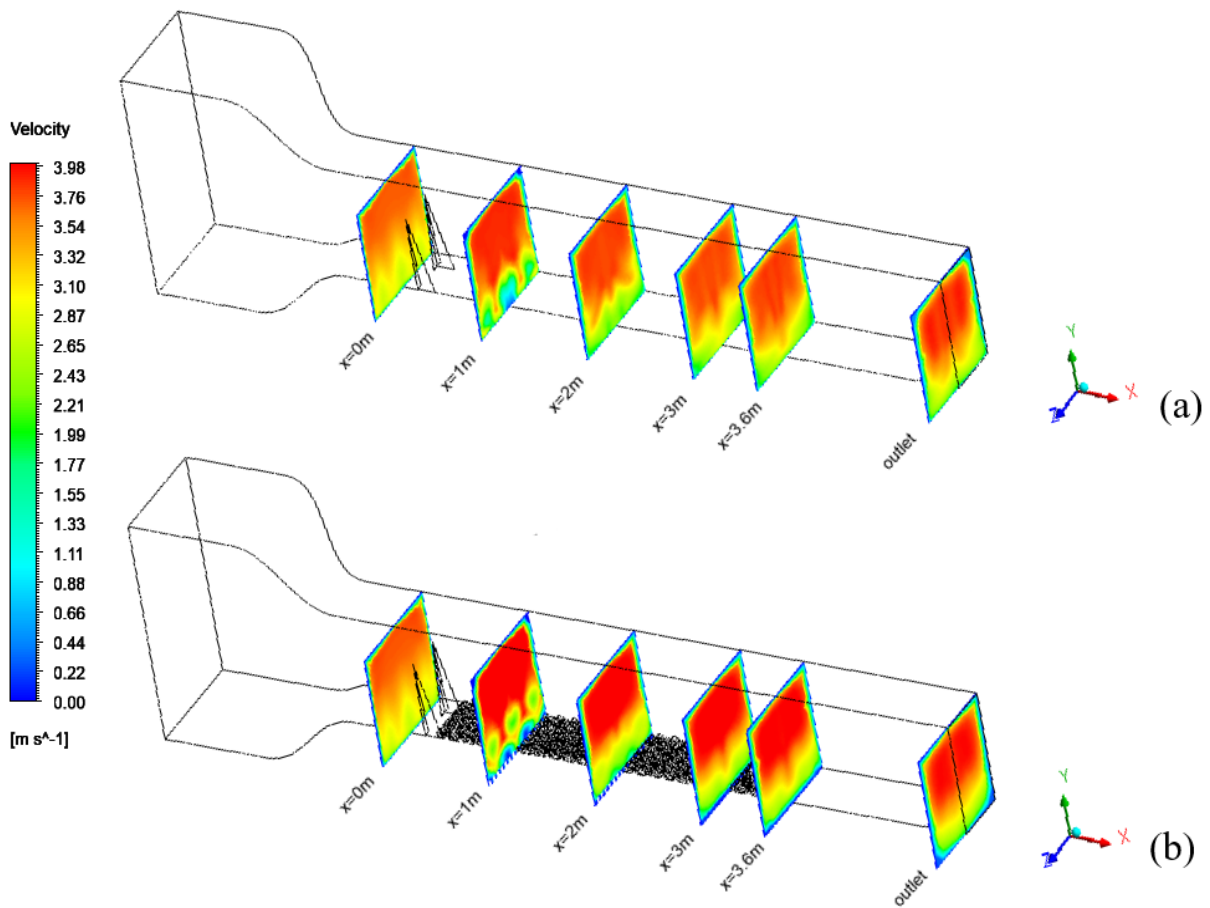


Figure 4.11 Contours of mean velocity at various cross-sections, at 1440 rpm fan speed, (a) for case 1, and (b) for case 2

After verifying the CFD simulations on low speed flows developed at the Assuit University, the ABL simulation was performed for practically ten times higher speed flow in the wind tunnel test at Belgrade University.

Figure 4.12 displays the velocity distributions in the plane of symmetry for the combination of wall barriers, elliptical spires, and arrays of small pyramids used at the Belgrade University wind tunnel, at the speed of 45 m/s.

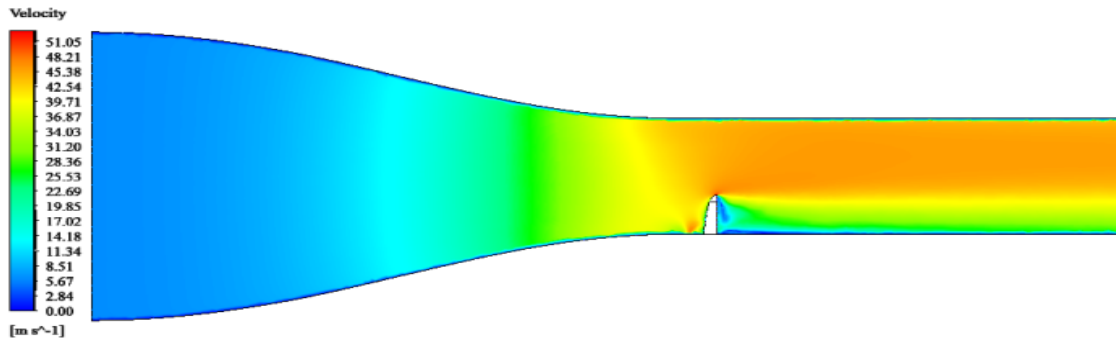


Figure 4.12 Contours of velocity magnitude for case 3, in the plane of symmetry

Figure 4.13 presents experimentally and numerically obtained values of the relative velocity (vertical velocity in the middle of the test section, divided by the velocity at the inlet of test section [92]) along with the relative height (vertical distance from the floor, divided by the height of the spire). The CFD results for this case also demonstrate quite fair agreement with the wind tunnel measurements for the engineering design requests.

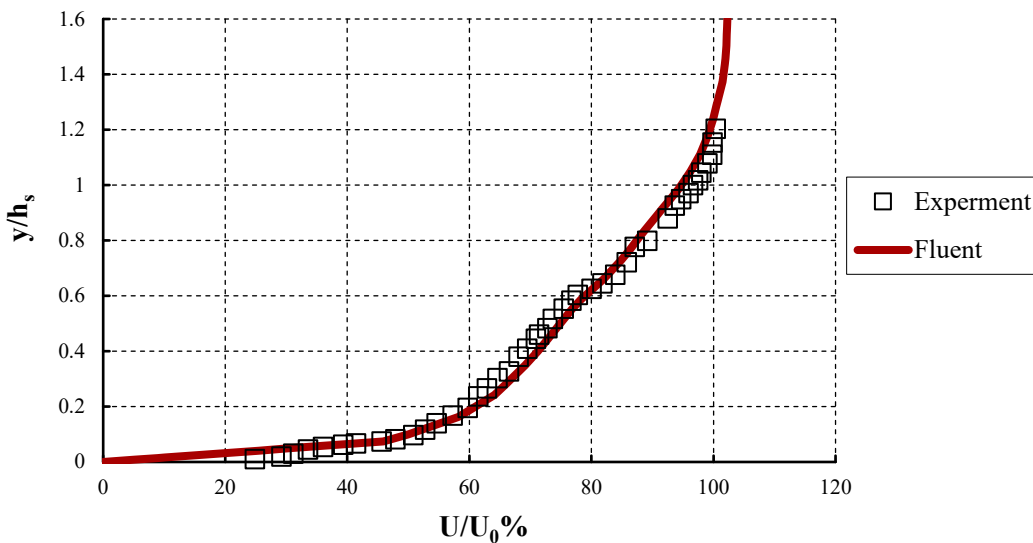


Figure 4.13 Comparisons of the relative velocity profiles for case 3

Figure 4.14 displays contours of velocity magnitude in several cross-sections along the test section. The wakes generated by the wall barriers, elliptical spires, and roughness elements are homogenous as the flow passes them. Also, the thickness of the developed boundary layer is relatively uniform for a long distance along the test section width, which allows us to make wider models on this test section.

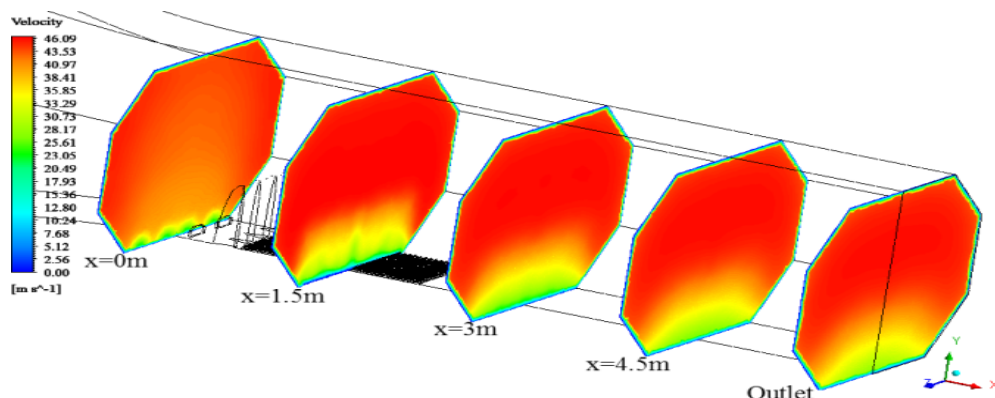


Figure 4.14 Contours of mean velocity for case 3 in various cross-sections, inside the test section

Figure 4.15 shows the contours of locally obtained eddy viscosity by the CFD analysis at the Assuit University test section when the fan speed was 1000 rpm. For the case 1, the domain of large eddy viscosities arises behind the spires and near the floor, and then it disappears along the development section. For the case 2, the eddy viscosity has a uniform diffuse downstream and reaches its higher values behind the spires mid-height.

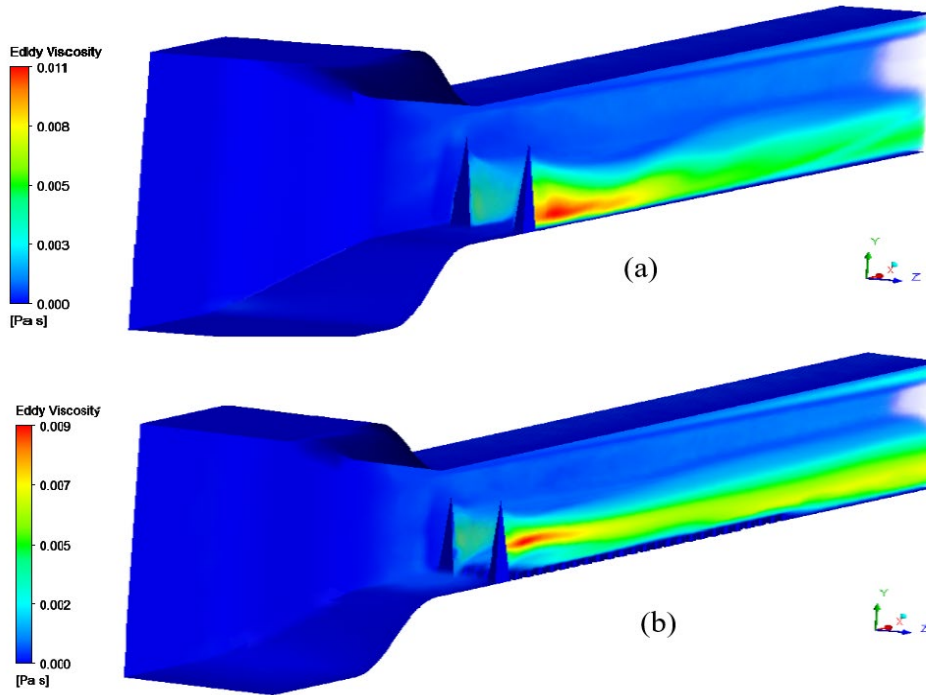


Figure 4.15 Contours of local eddy viscosity at 1000 rpm fan speed, (a) case 1, and (b) case 2

Figure 4.16 shows the local eddy viscosity contour of the Belgrade University wind tunnel. The domain behind spires has the same principle applied in case 2, except that the free-developed turbulent boundary layer on the upper wall is thicker than both cases at the Assuit University wind tunnel due to the smaller ratio of the spire height to the test section height.

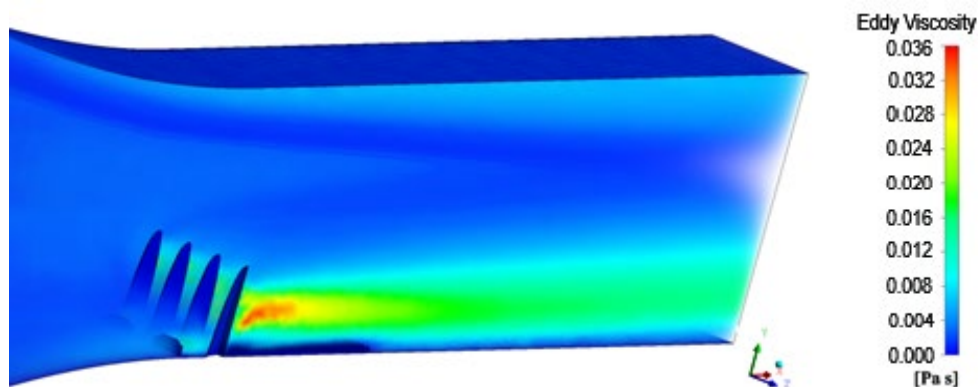


Figure 4.16 Contour of local eddy viscosity for case 3

4.3.2 Valuation of Wind Velocity Profile Parameters

The velocity profile in the ABL, as discussed earlier, is described by logarithmic (log) law and power law. These laws are expressed using several parameters such as u^* , z_0 , d , and α , which are essential in selecting the type of terrain types used to generate this velocity profile and scale models of structures in the wind tunnels.

The logarithmic law can be expressed as follows:

$$z = z_0 \exp\left(\frac{k U(z)}{u^*}\right) + d \tag{4-1}$$

and the power law can be expressed as:

$$\alpha = \ln(U(z)/U_s) / \ln\left(\frac{z-d}{z_s}\right) \tag{4-2}$$

The indirect approach is used to guess u^* , z_0 , and d by matching the logarithmic law in the inner layer with either experimental data or numerical results of the velocity profile. This approach uses the generalized reduced gradient (GRG) non-linear least squares method built in the Microsoft Office Excel Solver add-in [93]. It computes the values of the three parameters that best describe the experimental data by minimizing the sum of squared differences between determined height (height where velocity is determined) and predicted height for the same velocity in the logarithmic law using equation (4-1).

Table 4-2 presents the computed values of u^* , z_0 , and d for the three cases of simulating atmospheric boundary layers that best describe the experimental data after minimizing the sum of squared residuals using the Solver add-in.

Table 4-2 Values of u^* , z_0 and d

	Shear velocity u^* (m/s)	Roughness length z_0 (m)	Zero-plane displacement d (m)
Case 1	0.108	0.0000285	0
Case 2	0.239	0.0062	0
Case 3	4.753	0.0101	0

Figure 4.17 shows the fitting log law profiles for cases 1 and 2, where the log law profile passes through predicted height values that give the best fit to the determined height values. The determined height values were taken from the experimental results of the Assuit University wind tunnel, obtained at 1000 rpm fan speed.

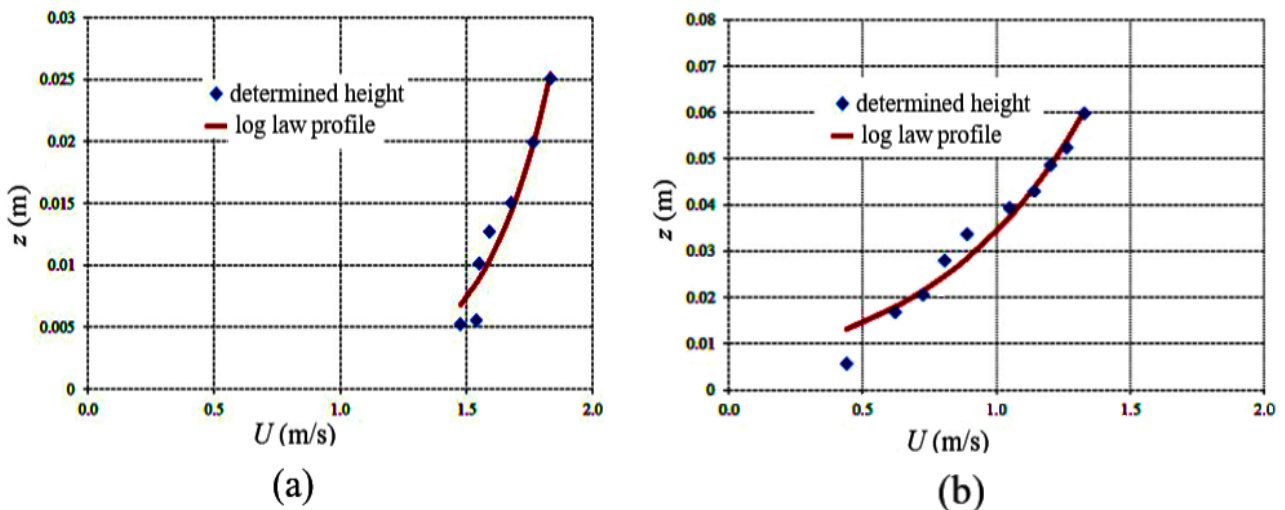


Figure 4.17 Best fitting log law profiles, (a) for case 1, and (b) for case 2

Figure 4.18 shows the fitting log law profile for the case 3, where the determined height values were taken from the experimental results from the Belgrade University wind tunnel.

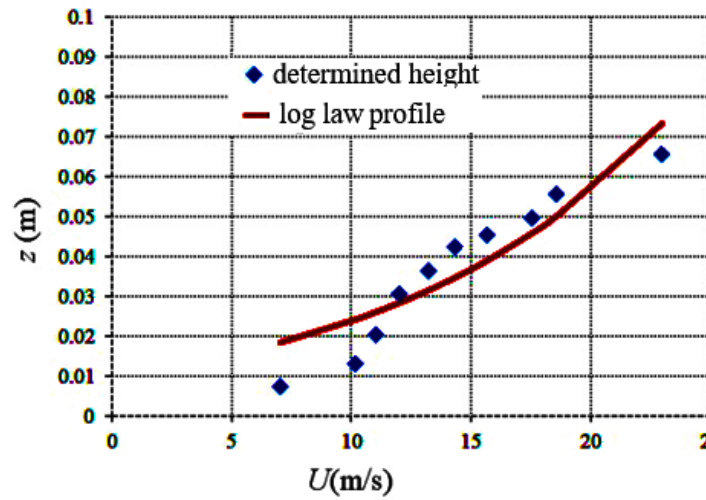


Figure 4.18 Best fitting log law profile for case 3

Assuming a scale model 1:100 of an object within the simulated ABL in wind tunnels, the computed roughness length z_0 for case 1 would be compatible with a very flat terrain range when comparisons are made with (Table 2-1above). Also, the value of z_0 for case 2 would close to the value of the suburban types, while the z_0 value for case 3 would agree with the value of the dense urban type. Alternatively, all computed zero-plane displacements are equal to zero for the measurements made downstream from the roughness surfaces in wind tunnel test sections.

Also, the power law represents the velocity profile in the outer ABL layer and it is used to define which terrain type or category is generated by that ABL. The fitting procedure is also practical for the power law profiles to estimate the values of α , using equation (4-2) after obtaining the zero-plane displacement d .

Figure 4.19 shows the fitting power law profiles for cases 1 and 2, compared with the determined relative velocity profiles from the Assuit University wind tunnel, at 1000 rpm fan speed. For case 1, the power law gave a computed value of $\alpha = 0.12$, which characterizes a flat area (Figure 2.3), while for case 2, the computed value $\alpha = 0.24$ characterizes the suburban area.

Figure 4.20 shows the fitting power law profile for case 3, compared with the calculated relative velocity profiles from the Belgrade University wind tunnel. In this case, power law provides value of $\alpha = 0.37$, characterizing a large city area.

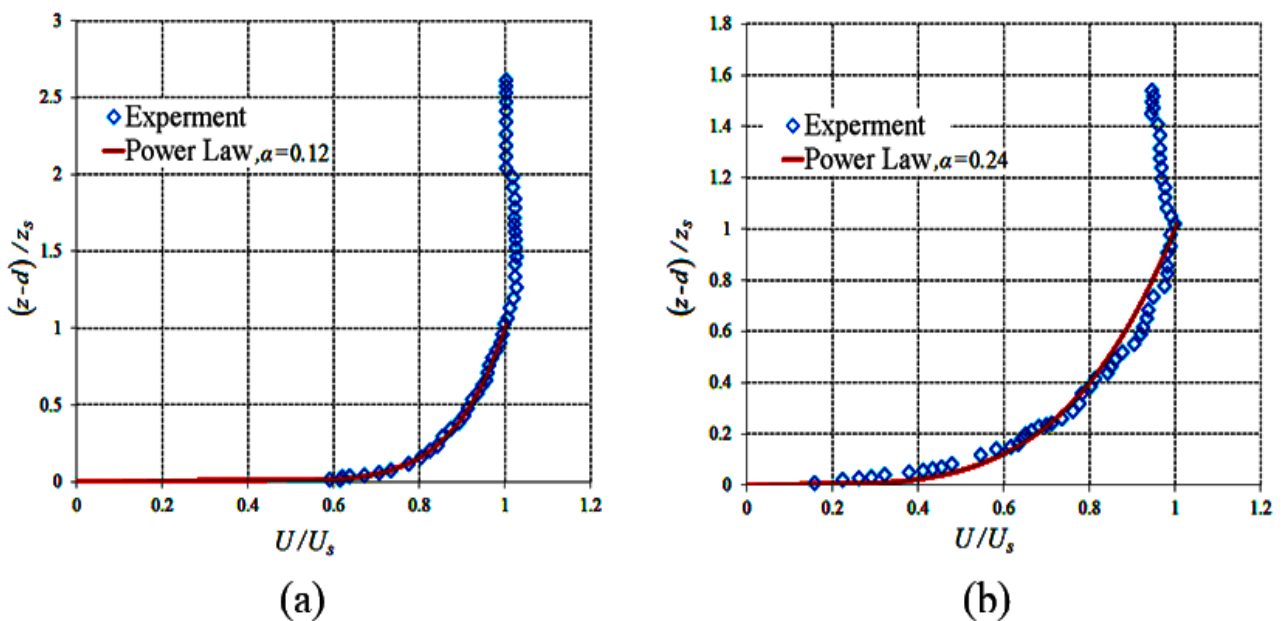


Figure 4.19 Best fitting power law profiles, (a) for case 1, and (b) for case 2

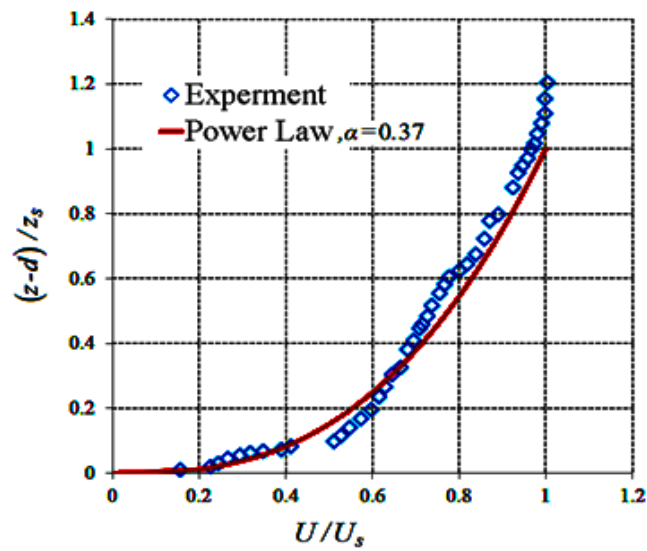


Figure 4.20 Best fitting power law profile for case 3

These calculations show a very good match to log law profiles for the inner ABL layer and power law profiles for the outer ABL layer with different terrain categories.

CHAPTER 5: EXPERIMENTAL AND NUMERICAL ANALYSIS OF A MEDIUM RISE-BUILDING WIND LOADINGS

This chapter describes several experimental tests that have been conducted on a medium-rise building at Belgrade university wind tunnel, where the pressure was measured at different locations on the model. Then CFD analyses were performed for comparison with experimental results.

5.1 The Wind Tunnel Experiment

All experiments presented in this chapter have been carried out recently in the Belgrade University wind tunnel to fulfill the research goals within this Ph.D. thesis. While the same passive devices that were used and described in chapter four are still existing, and the boundary layer with the urban area exposure category ($\alpha = 0.37$, $z_0 = 0.0101$ m) was simulated and obtained.

As most hotels and residential buildings in urban areas fall in the intermediate height classification, it is interesting to examine and investigate the wind effects upon such structures. So the medium-rise building as Metropol Palace Hotel at Belgrade, Serbia, as shown in Figure 5.1, was chosen to model in the wind tunnel test section.

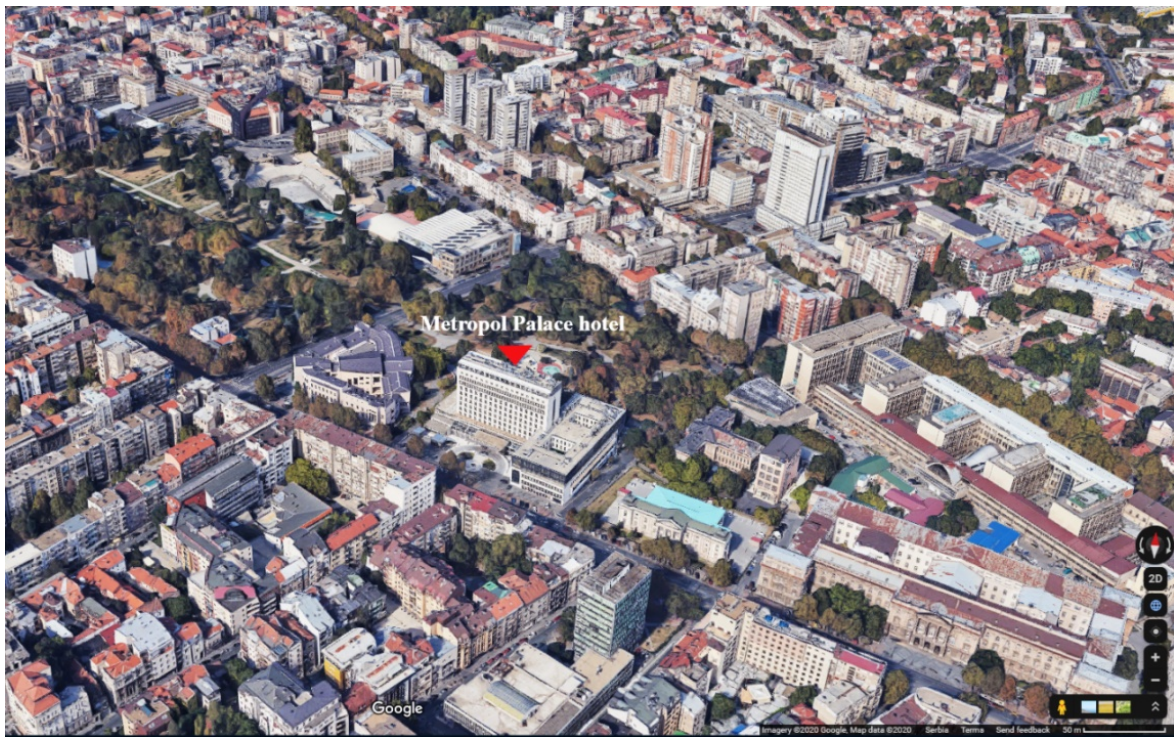


Figure 5.1 Metropol Palace Hotel at Belgrade, Serbia

5.1.1 Building Model

The Metropol Palace hotel has a height of 42 m, so a 1:100 geometrical scale model was chosen according to matching the Jensen number in the simulated boundary layer in the wind tunnel with a natural boundary layer

$$J_m = J_n \square \frac{h_m}{z_{0m}} = \frac{h_n}{z_{0n}} \Rightarrow \frac{h_m}{0.01} = \frac{42}{1} \Rightarrow h_m = 0.42 \text{ m}$$

The locations and patterns of pressure taps were elected to identify better the possibility of interpolating pressures between them. However, each pressure tap was numbered to recognize where the pressure will be measured.

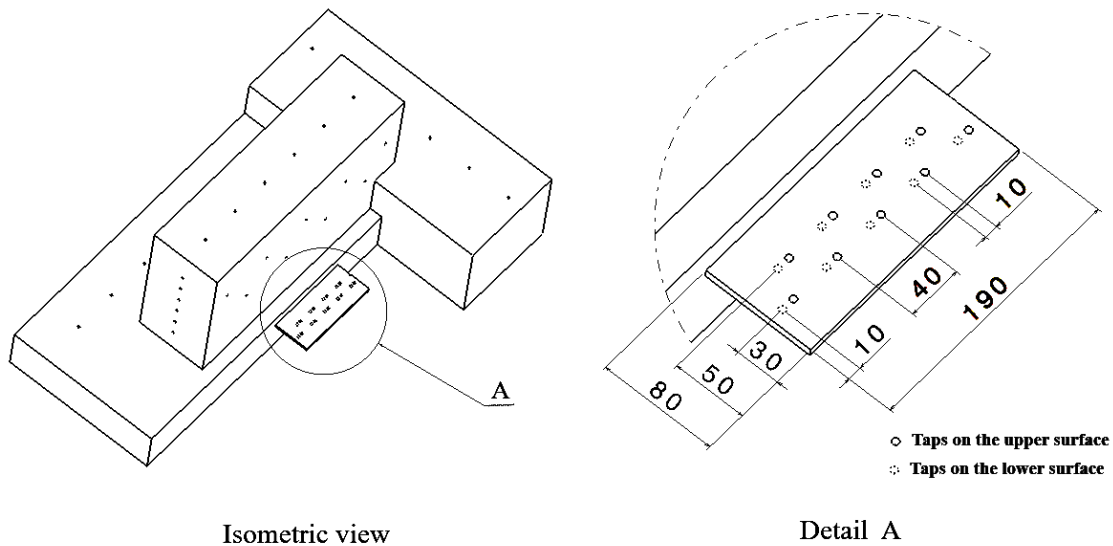


Figure 5.4 Taps locations on the canopy surfaces, all dimensions in mm

5.1.2 Experiment Instruments

The major goal of this experimental investigation is to measure the pressure at different locations on the model building. The pressure measurement system consists of a tubing system, a multi-manometer box, and a microcontroller linked to a computer.

The tubing system is compiled of an adapter and a silicone tube. The adapter connects a 5 mm inner diameter (ID) silicone tube with the 3 mm pressure tap on the model surface, and was manufactured by soldering two copper pipes a 3 mm pipe (2 mm ID) with a 6 mm pipe (4 mm ID). Afterward, the adapter was inserted and glued to the model tap, and the 0.5 m length of the silicone tube was pushed and stretched to fit with the large copper pipe, as shown in Figure 5.5.

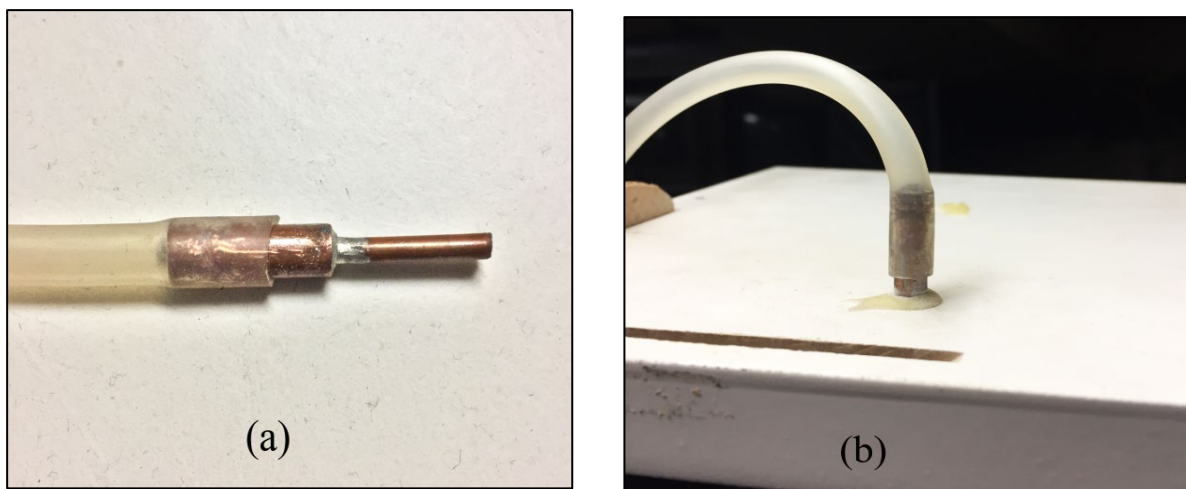


Figure 5.5 (a) Adapter used to connect the 5 mm silicone tubing with the 3 mm pressure tap, (b) Adapter glued to the model wall

The adapter diameters, together with the silicone tube's diameter and length, were chosen according to their influence on pressure reading from previous experiments carried out by other researchers as [94,95], to avoid reverberation in pressure waves and attenuation in the fluctuating pressures.

The multi-manometer box was manufactured to house 60 pressure sensors. It contains two connecting parts: Cap box with ports to receive pressure input through the tube system attached to taps on the building model, see Figure 5.6, and the sensors housing box has channels where the sensors are inserted and glued well inside them, as shown in Figure 5.7.

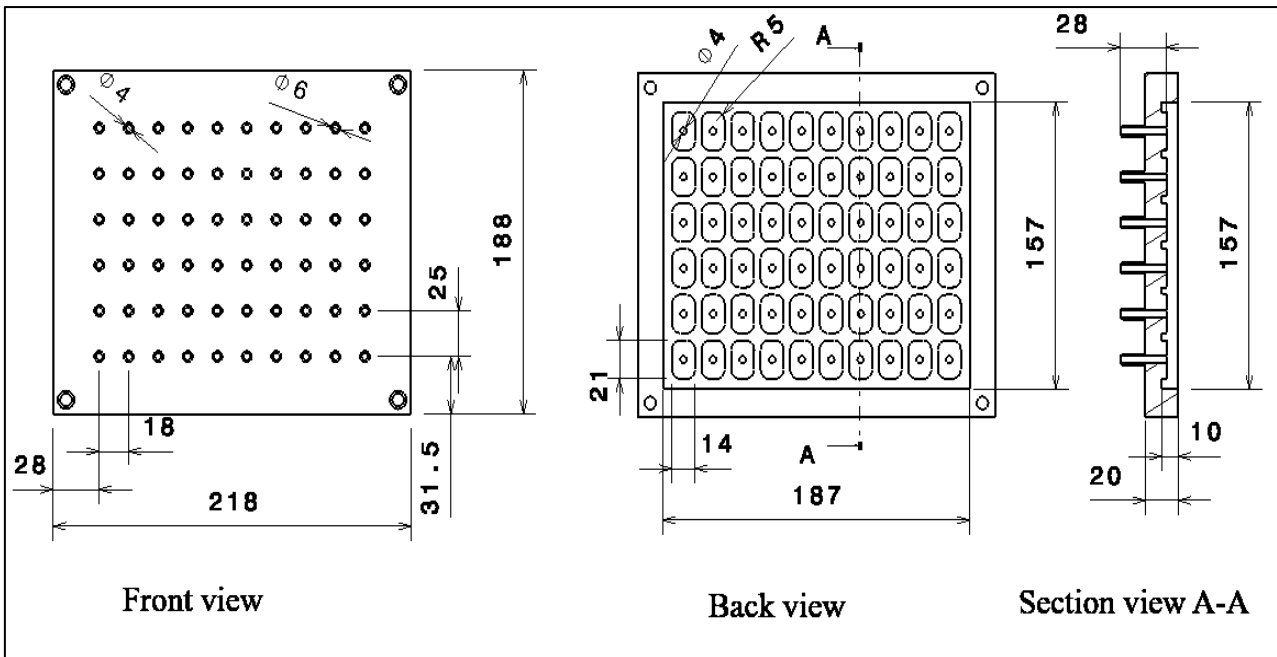


Figure 5.7 Cap box of the multi-manometer

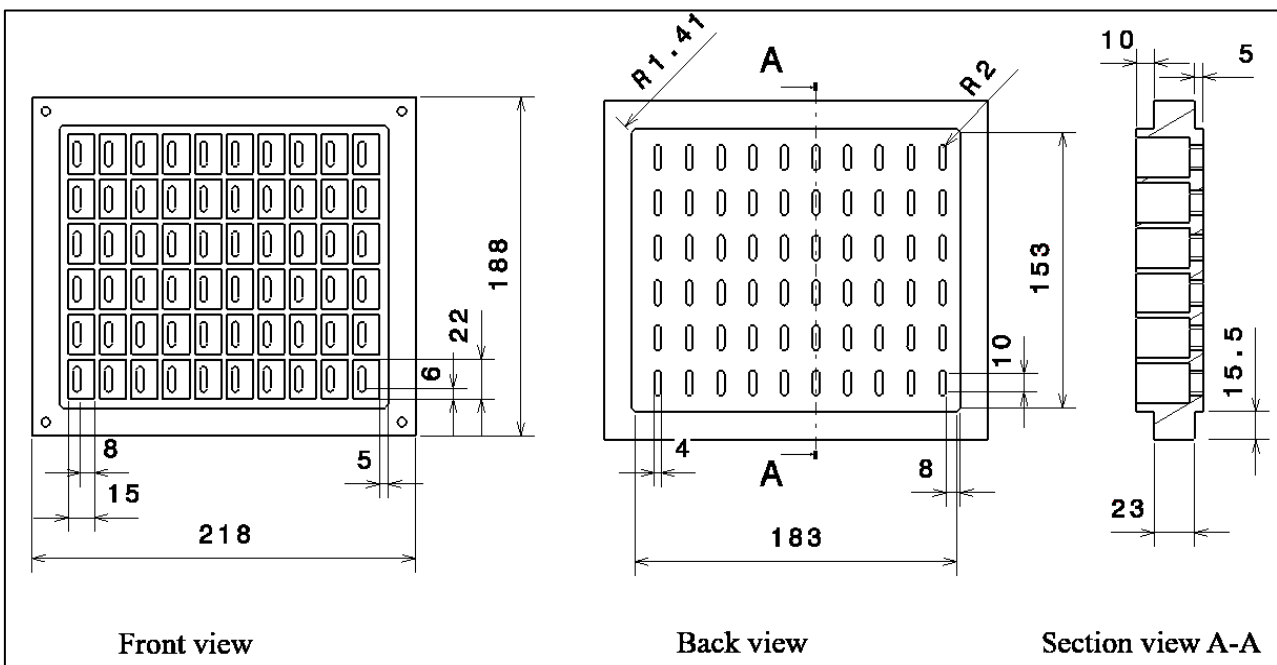


Figure 5.6 Sensors housing box of the multi-manometer

The sensors were connected to an Arduino Mega 2560 microcontroller board, as shown in Figure 5.8, and the Arduino was linked to the computer by an AB USB cable (called a USB printer cable), used to program the board and not just to power it up.

The Arduino software provides the ability to write code in the program language C and has a graphical interface conducive to the visualization of parameters measured by the sensor. The library (code) used to run a BMP 280 sensor was downloaded and redesigned for fifty-eight sensors using

the SPI protocol. VISUAL BASIC was used to collect a large quantity of data as a text file for further processing.

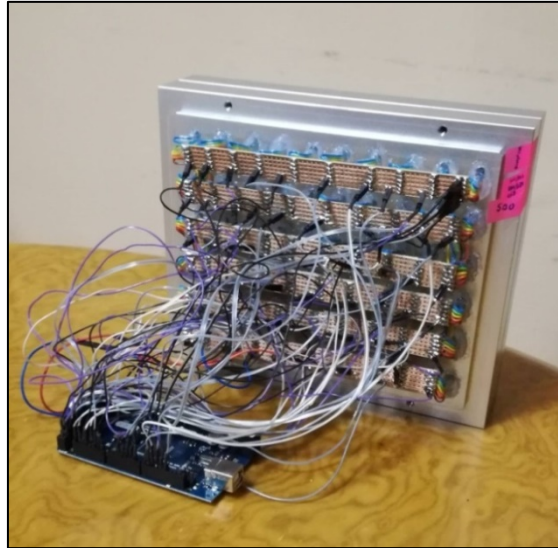


Figure 5.8 Sensors connection to the Arduino

5.1.3 Sensors Testing

The sensors are the main devices to measure the pressure in our experiments, so it was necessary to use an accurate and attainable sensor. BOSCH BMP280 sensor has been chosen and tested, which is an absolute barometric pressure sensor, see Figure 5.9, with technical data shown in Table 5.1, [96].

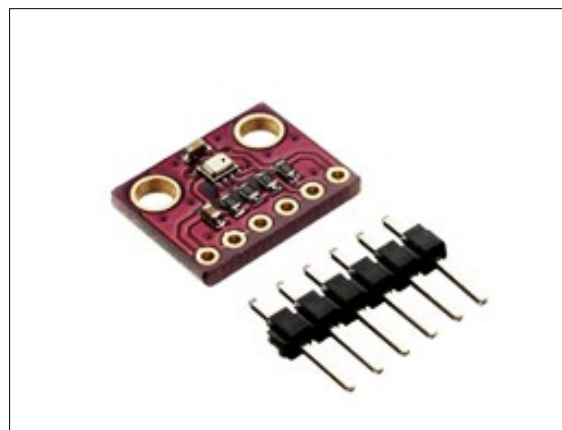


Figure 5.9 BOSCH BMP280 sensor

Table 5.1 Technical data of BOSCH BMP280 sensor

Operation range	Pressure: 300...1100 hPa Temperature: -40...85°C
Absolute accuracy	±1 hPa
Digital interfaces	I ² C (up to 3.4 MHz) SPI (3 and 4 wire, up to 10 MHz)

5.1.3.1 Velocity Calibration for the Sensors

This calibration process aims to formulate a relationship between the velocity calculated by sensors connected to a secondary pitot tube and the nominal speed measured by a wind tunnel

device (a primary Pitot tube).

The secondary Pitot tube was settled in the middle of the empty wind tunnel test section and connected to two silicone tubes to measure the static and total wind pressures at different wind velocities inside the wind tunnel, see Figure 5.10.

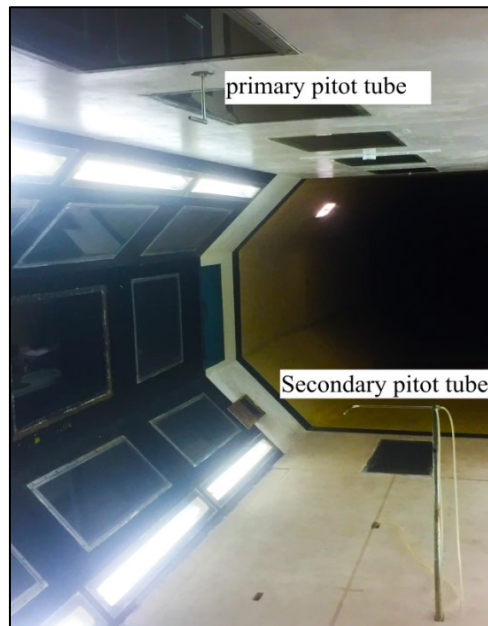


Figure 5.10 Pitot tube used for testing sensors

Four BMP280 sensors have been tested. Each sensor is inserted and glued inside an air capsule filter with two ports, as shown in Figure 5.11. One port was connected within a short silicone tube, and the sensor wires moved out from the other port to link with the Arduino Mega board and then to the computer.



Figure 5.11 The sensor inside an air capsule filter

In this test, the Arduino software was programmed to monitor and show four sensors reading. For recording the pressure values of the four sensors simultaneously, every two sensors were connected using their short silicone tubes with a multi-tubing connector, then static and total pressure silicone tubes of the Pitot tube were switched to each tubing connector. Likewise, this process was repeated for a different speed of blowing air.

The test was proceeded first by measuring a value of the atmospheric pressure inside the wind tunnel (i.e. the pressure at zero nominal speed) using a barometer. Then at each wind tunnel nominal speed, static and total pressure values were measured. Also, at the same time, the air temperature value was measured using a wind tunnel device.

Afterward, the calculation process was started by correcting the pressure values (static and total) using the difference between their measured values at zero nominal speed and atmospheric

pressure value. Then, the velocity was calculated using these modified pressure values with measured air temperature according to equation (5.1):

$$V = \sqrt{2 \times (P_t - P_s) / \rho} \tag{5.1}$$

where $\rho = \frac{P_{am}}{R T}$, and $R = 287 \text{ J.kg}^{-1}.\text{K}^{-1}$ for the air.

Figures 5.12 and 5.13 show the calculated velocities for the sensors. The calculated velocity values are a little bit lower than the wind tunnel nominal speeds.

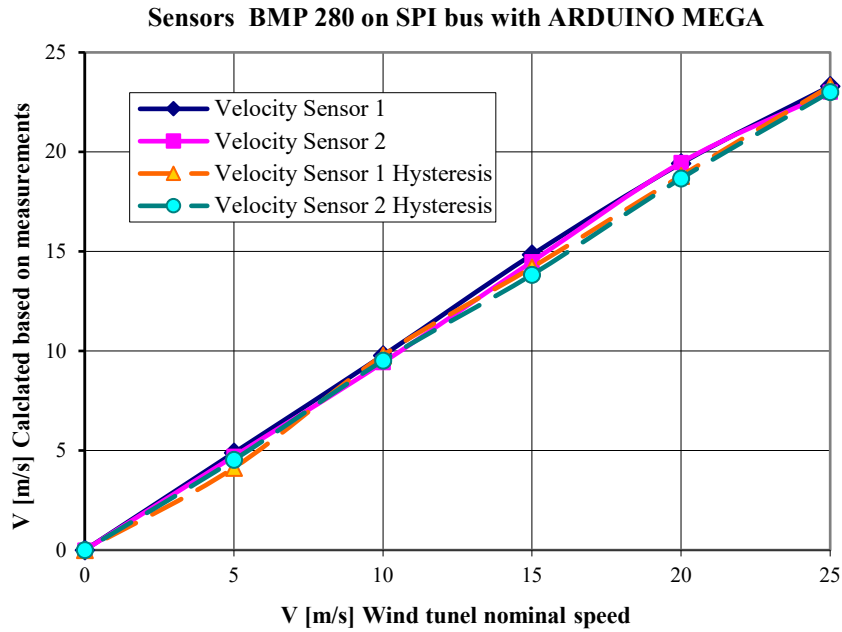


Figure 5.12 Velocity calculated for the first two sensors

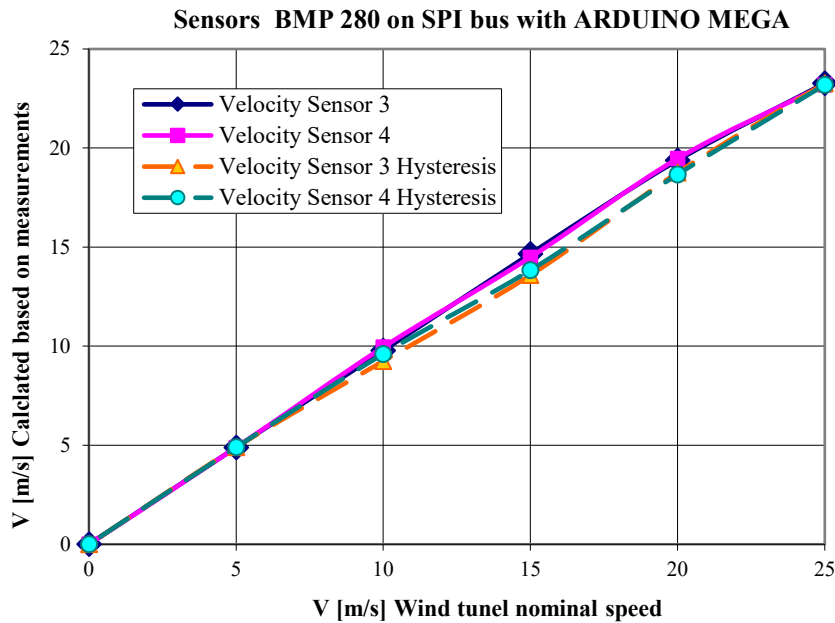


Figure 5.13 Velocity calculated for the second two sensors

5.1.3.2 Pressure Calibration for the Sensors

In addition to the previous testing work, other modifications to the measuring values of

pressures (static and total) were made by using a difference between their values at zero nominal speed and standard atmospheric pressure (sea level where $H=0$) to expose and compare measured pressures for the four sensors as the nominal speed increases. The result is shown in Figure 5.14.

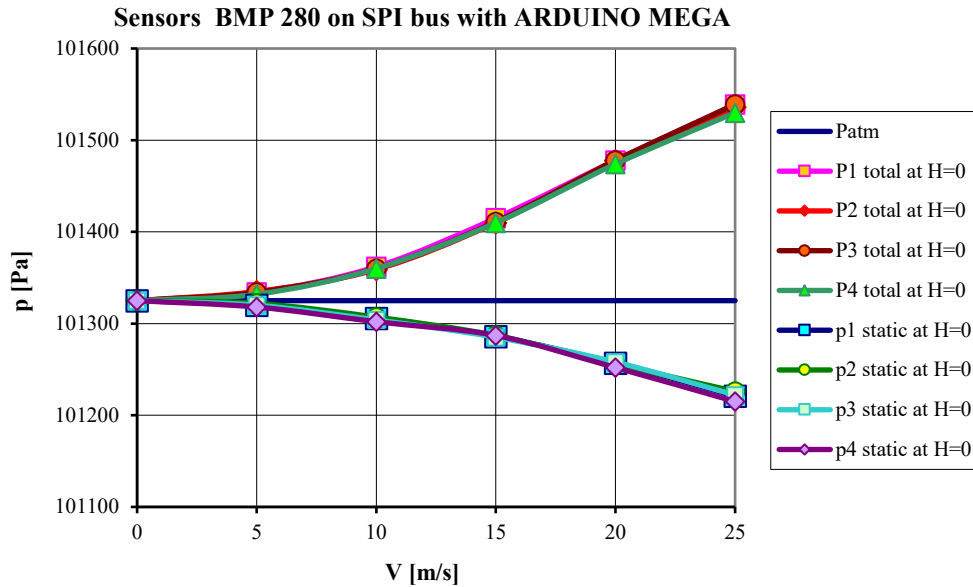


Figure 5.14 Comparison between measured pressures and the wind tunnel nominal speed

A second test was also done for the two BMP280 sensors at the Mathematical Faculty of Belgrade University using the Mensor series 600 Automated Pressure Calibrator (APC) (barometer SN: 610499). The APC contains a barometer uses to measure the atmospheric pressure so the Mensor 600 can calibrate gauge or Absolute pressure, and a transducer installed on a pressure regulator to measure the precise pressure used for the calibration by controlling the pressure comes from a vacuum pump [97].

The sensors capsule connected to the PC as in the previous test, while they were connected separately to the APC using their silicone tube, as shown in Figure 5.15, and the Mensor 600 was connected to the pressure supply system that includes the nitrogen cylinder and vacuum pump.

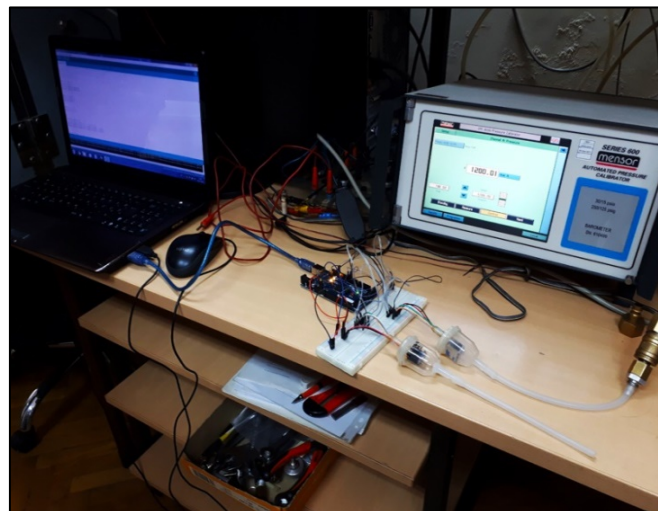


Figure 5.15 Sensors connections and calibration procedure

The calibration began by setting the pressure on the APC touch screen at zero absolute pressure value by pressing the control bottom. Then, by pressing step up and step down keys, the pump will pump up or down the nitrogen to the APC and the sensor capsule to regulate the pressure to the desired value, as shown in Figure 5.16. After stabilizing the pressure value on the screen, the

sensor pressure started recording. This process was repeated to all adjusted pressures for both sensors. The desired pressure was set up /down on the APC screen from 30000 to 110000 Pa stepping by 1000 Pa according to the operating pressure range for the BMP280 sensor.



Figure 5.16 Typical operation screen

The calibration sensors results are shown in Figures 5.17 and 5.18, where the difference between measured pressure by the sensor (P_s) and set pressure by the Mensor (P_m) decreases as Mensor pressure increases and vice versa.

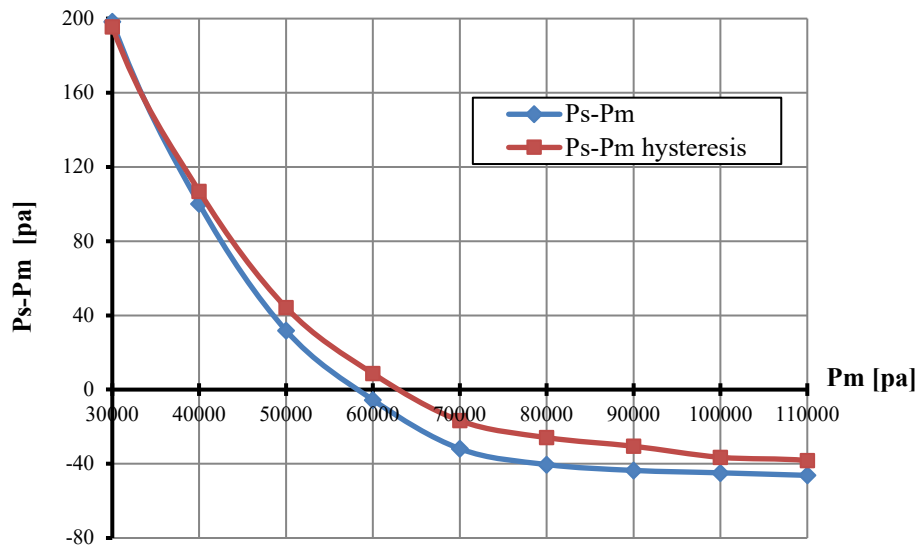


Figure 5.17 Calibration results for the first sensor

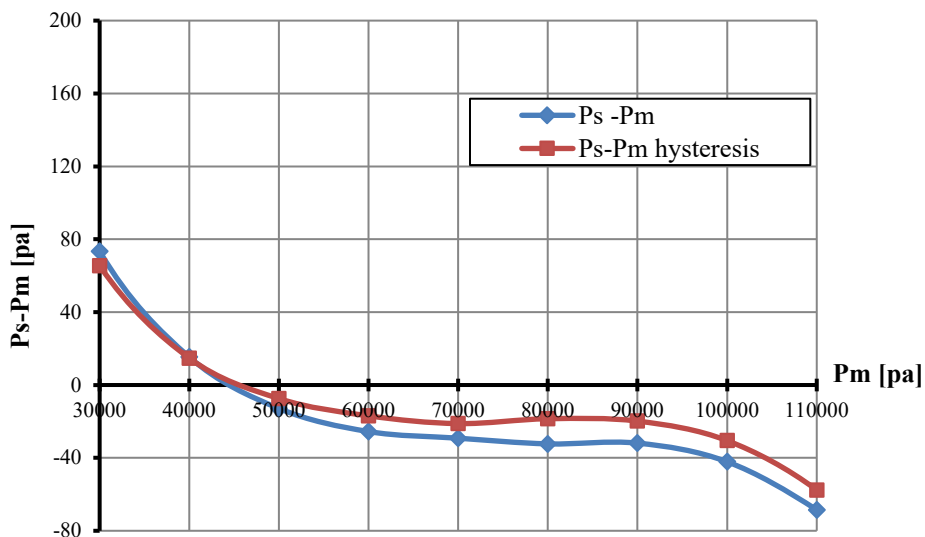


Figure 5.18 Calibration results for the second sensor

5.1.4 Experimental Procedures

To investigate the flow field around the model in the wind tunnel few preparation steps have been done: began by setting up the passive devices used to generate the urban boundary layer in the test section, connecting the multi-manometer box with taps on the model, positioning the multi-manometer box with the microcontroller inside the model building, gluing model with turntable and located in the central of the test section, and ended by connecting the microcontroller with the computer.

At the beginning of the experiments, since no blowing air occurred and the pressure inside the wind tunnel was atmospheric, fifty-seven absolute pressures were measured on the model while one sensor has failed (sensor no. 27). The absolute pressure measured by sensor (no. 39) was chosen and used as a reference pressure, as it is on the top face of the model and close to its center, as shown in Figure 5.19. The deviations of all measured pressures from the reference pressure value calculated and used to correct the next measuring absolute pressures after the blowing.

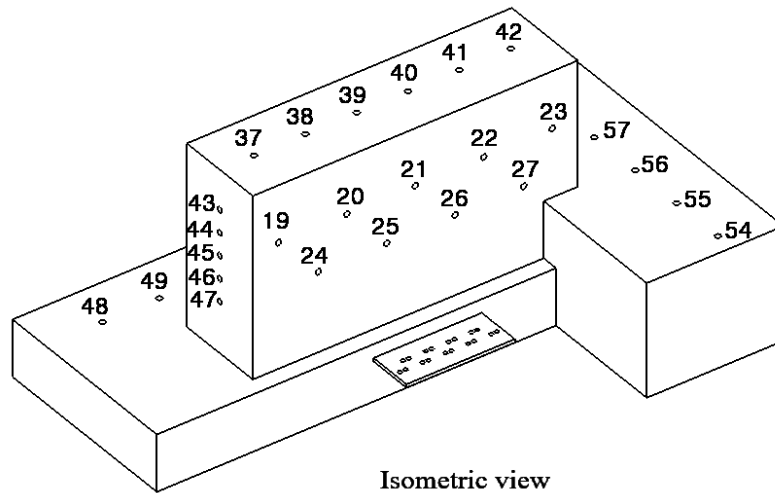


Figure 5.19 The model isometric view shows the locations of the sensors

Each sensor’s absolute pressure value is the average of approximately 25 measured values at 1 minute running on the Arduino program. Figure 5.20 presents those pressure measurements.

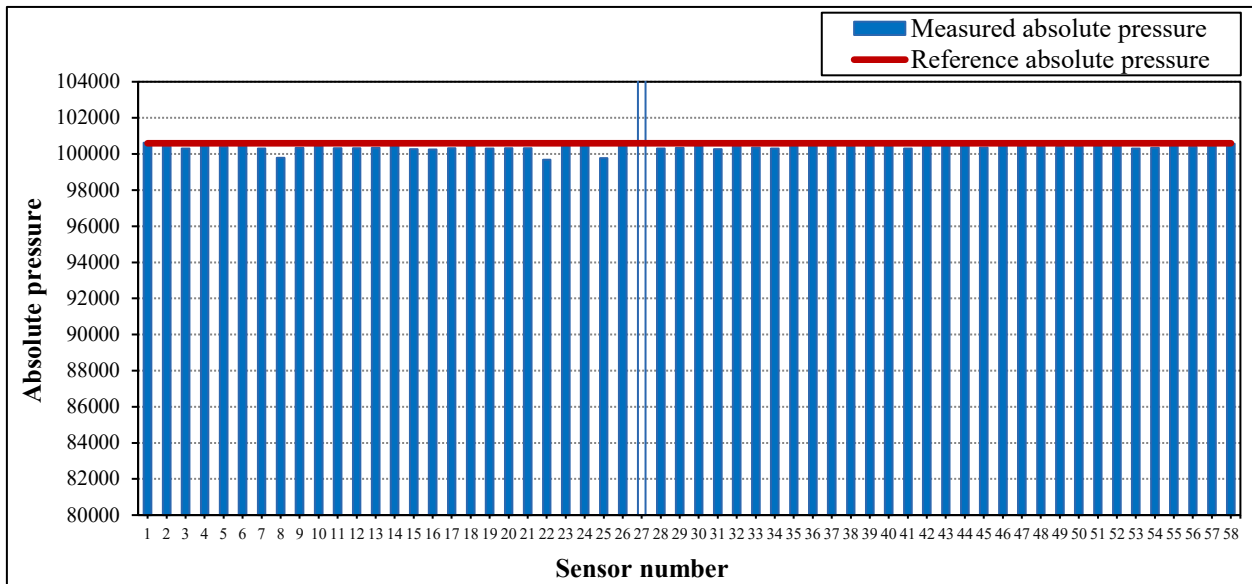


Figure 5.20 Absolute pressure measurements on the model at 0 m/s

The model experiments were carried out with the velocity varying from 5 to 20 m/s at an increment of 5 m/s to obtain measurable and reliable pressure difference. The pressure measurements were also achieved by rotating the turntable handy for four angles (0°, 45°, 90°, and 135°), as shown in Figure 5.21. The results of these experiments present later in this chapter.

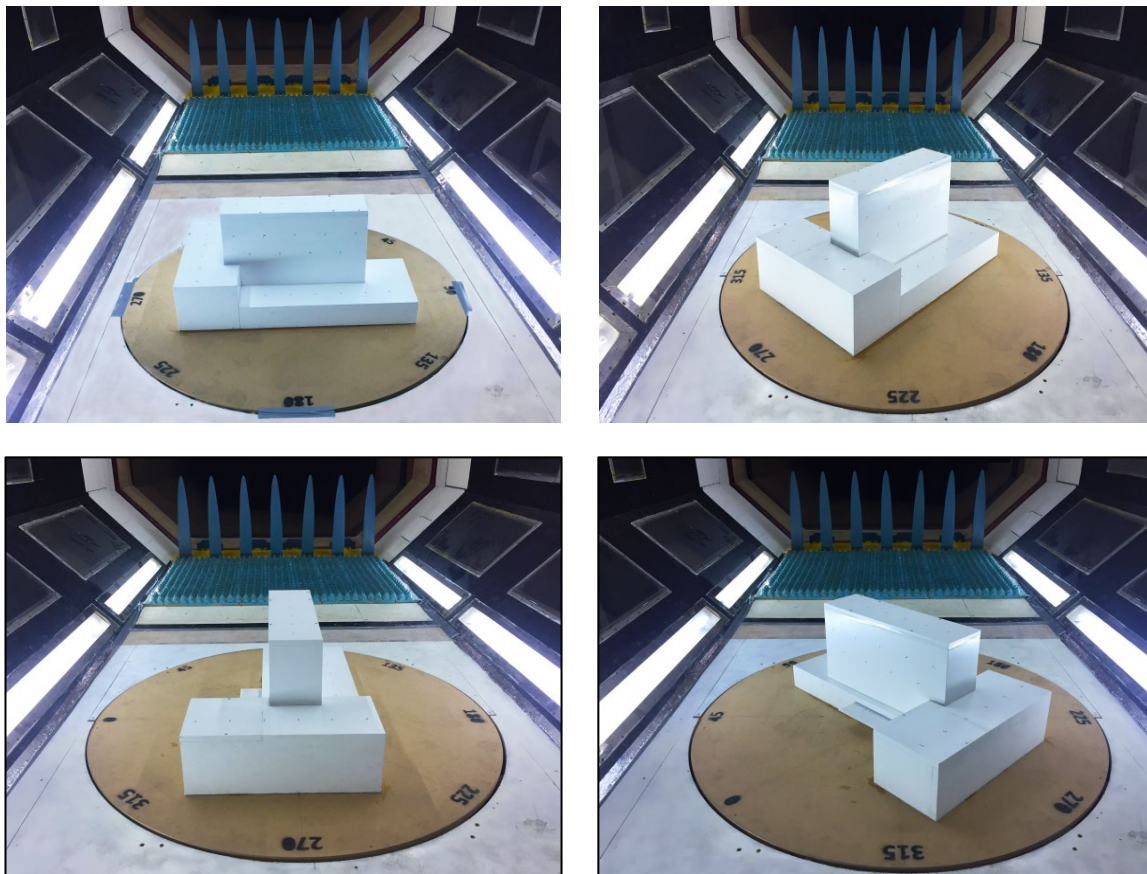


Figure 5.21 The model positions on the wind tunnel test section

5.2 Numerical Simulation of the Medium-Rise Building

Numerical simulation of the wind flow over the medium-rise building model is accomplished using the CFD code Ansys Fluent. The CFD simulation aims to compare calculated values with the experimentally measured pressures for validation.

5.2.1 Numerical Simulation Procedure

5.2.1.1 Computational Domains and Mesh Configuration

The scaled building, the full-scale of the wind tunnel test section with the same devices configurations inserted on its floor, and without/with the collector were adopted as the computational domain. The building model had been created by the Catia software and imported to the Fluent geometry to create the computational domain, as shown in Figure 5.22.

The two computational domains without and with the collector were performed at zero wind direction azimuth. The first computational domain has a smaller number of elements than the second one to reach a faster solution in less time. In contrast, meshing the added collector increase the number of elements in the second computational domain.

The unstructured mesh was created for both computational domains with a maximum element size of 10 cm and a minimum element size of 5 mm. Additionally, particular zones were resized in order to capture more geometrical details and approximate better the higher gradients of these zones. These zones sizing were:

- 2 cm for the collector floor, the spires, and the barrier walls,
- 1 cm for the test section floor with the small pyramids,
- 5 mm for canopy faces with 1cm for the rest of the building faces,
- 2 cm influence of half-sphere with 65 cm diameter around the building model, as shown in Figure 5.23.

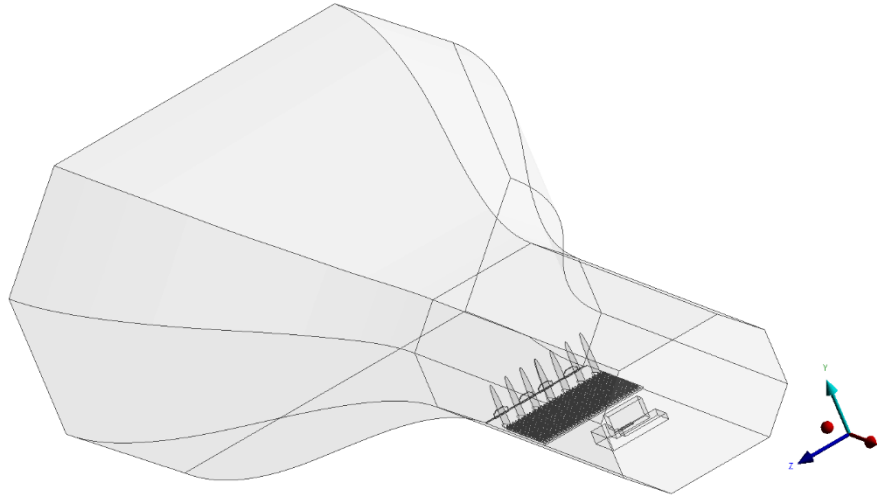


Figure 5.22 The computational domain when the collector included

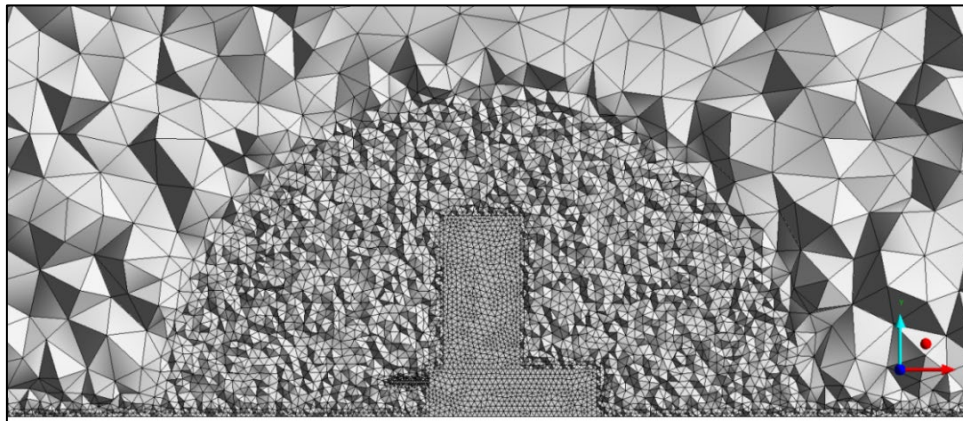


Figure 5.23 Unstructured mesh generated for the model building and the zone around it

As a result of using both computational domains at zero wind direction azimuth, which is shown and explained later, the second computational domain was more suitable to calculate the pressures, so it was applied for the four wind direction azimuths. The number of elements created in each unstructured mesh is presented in Table 5.2.

Table 5.2 Number of elements in every computational domain

The computational domain	Wind direction	Number of elements
without the collector	0°	3,041,766
with the collector	0°	5,152,543
with the collector	45°	5,151,570
with the collector	90°	5,155,451
with the collector	135°	5,151,064

5.2.1.2 Setup and Solution

These processes were performed using the same solver of (RANS) equations, turbulence model, solution methods, and boundary conditions described in the previous chapter, except the

inlet boundary condition. Considering the equal volume flow rate through the collector and according to the average of the velocity calculated based on measurements from Figures 5.12 and 5.13, the ‘inlet velocity’ boundary condition was set at various velocities at the collector inlet, corresponding to 5 m/s, 9.8 m/s, 14.5 m/s, and 19 m/s at the inlet of the wind tunnel test section.

The solution convergence was reached when the outlet mass flow rate on the solution monitor remained steady, using the criterion in order of 10^{-6} .

5.3 Results and Comparisons

The experimental results acquired from the wind tunnel and the numerical simulation CFD results are presented and analyzed here for the modeled building. All results are obtainable in the form of absolute pressure, using the absolute pressure at the building top as the reference pressure (Tap no. 39), where it was used in experiments results, as already discussed, and also used in Fluent software as the operating pressure.

Since the pressure taps have been located on the model faces in one row or staggered rows, the model faces and rows were numbered, including the sensors numbers in each row, as shown in Figures 5.24 and 5.25.

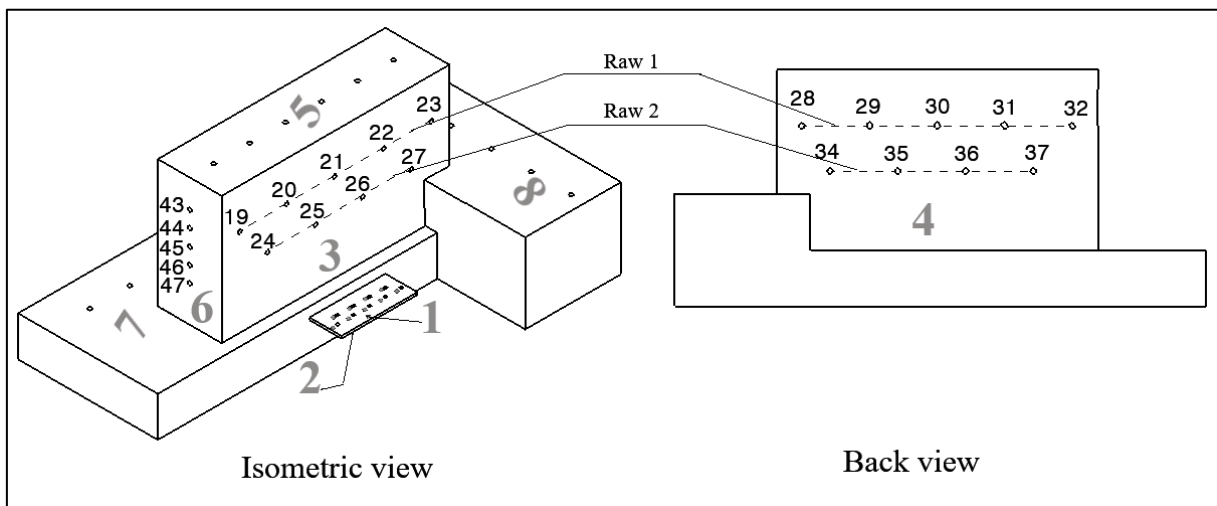


Figure 5.24 Isometric and back views of the model with faces, rows, and sensors numbers

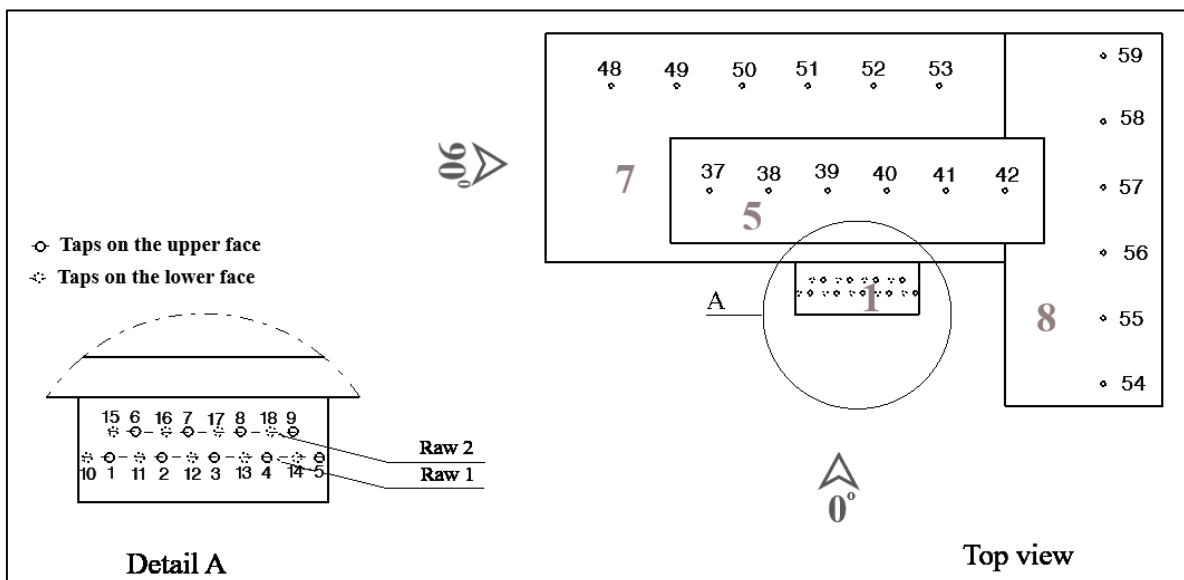


Figure 5.25 Top view of the model with faces, rows, and sensors numbers

The results were presented sequentially to illustrate the variation of absolute pressures on the model building faces with respect to the increase of velocities of blowing at each wind direction azimuth.

These absolute pressures were displayed on each face using the sensor's numbers and their rows on that face. On the first four faces the results are shown in two rows, while on the other four faces the results are shown in one row.

Figures 5.26 to 5.29 show the comparison between measured and calculated absolute pressures by CFD on the model faces at zero wind direction azimuth, using both the computational domains with and without the collector. The CFD calculations for the computational domain with the collector show better predicated to the absolute pressure values, so the CFD calculations with the collector are used in our work.

Moreover, the calculated absolute pressure values on all model faces are approximately the same as the measured values from the experiment, as shown in figures 5.26 and 5.27. Also, in figures 5.28 and 5.29, the calculated absolute pressure values correspond to the measured values. Nevertheless, in some faces, as shown in panels (a, b, c, d, e, f, g, and h), the calculated absolute pressure values on those model faces are a little higher than the measured values, with a maximum absolute difference (the maximum difference value between the calculated and measured absolute pressure values) is 25 and 30 Pa, respectively.

Figures 5.30 to 5.33 show the comparison between CFD calculations and experiment results on the model faces at 45° wind direction azimuth. The calculated absolute pressure values in all model faces in all figures 5.30 and 5.31 show very good agreement with the measured values. Moreover, in both figures 5.32 and 5.33, the calculated absolute pressure values on the faces (1, 2, 3, and 6) are equal or slightly higher than the measured values, with a maximum absolute difference obtained in panel (d) is 15 and 20 Pa, respectively. In contrast, the calculated absolute pressure values on the other faces are a little smaller than the measured values, and the maximum absolute difference obtained in panel (i) is 20 and 42 Pa, respectively.

Figures 5.34 to 5.37 show good agreement between CFD calculations and experiment results on the model faces at 90° wind direction azimuth, especially in figures 5.34 and 5.35. Besides, in figures 5.36 and 5.37, the calculated absolute pressure values are a little higher than the measured values on some model faces, with the maximum absolute difference found in panel (f) is 20 and 40 Pa, respectively.

Figures 5.38 to 5.41 show the comparison between CFD calculations and experiment results on the model faces at 135° wind direction azimuth. In figures 5.38 and 5.39, the values of calculated absolute pressure on all model faces agree well with the measured values.

In figures 5.40 and 5.41, the values of calculated absolute pressure are slightly lower than the measured values on faces (1, 2, 3, 5, and 8), with the maximum absolute difference found in panel (f) is 12 and 30 Pa respectively. Also, the calculated absolute pressure values are a little higher than the measured values on faces (4, 6, and 7) in both figures, with the maximum absolute difference found in panel (k) is 18 and 23 Pa, respectively.

In general, the values of calculated absolute pressure by CFD show a good agreement with the values of measured absolute pressure in the wind tunnel, especially when the air velocity is equal to or less than 10 m/s.

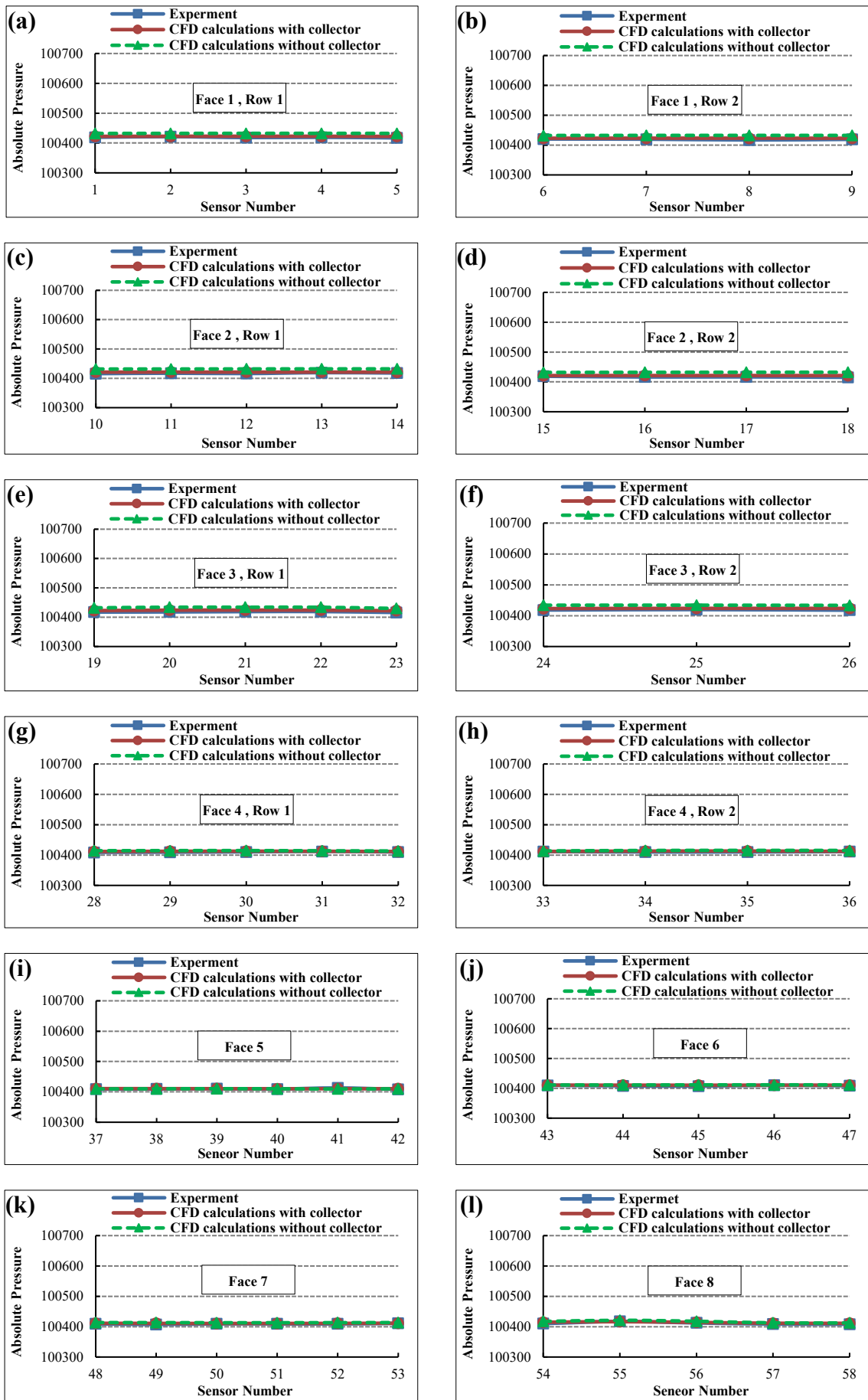


Figure 5.26 Pressure comparison at 0 degrees wind direction azimuth, 5 m/s

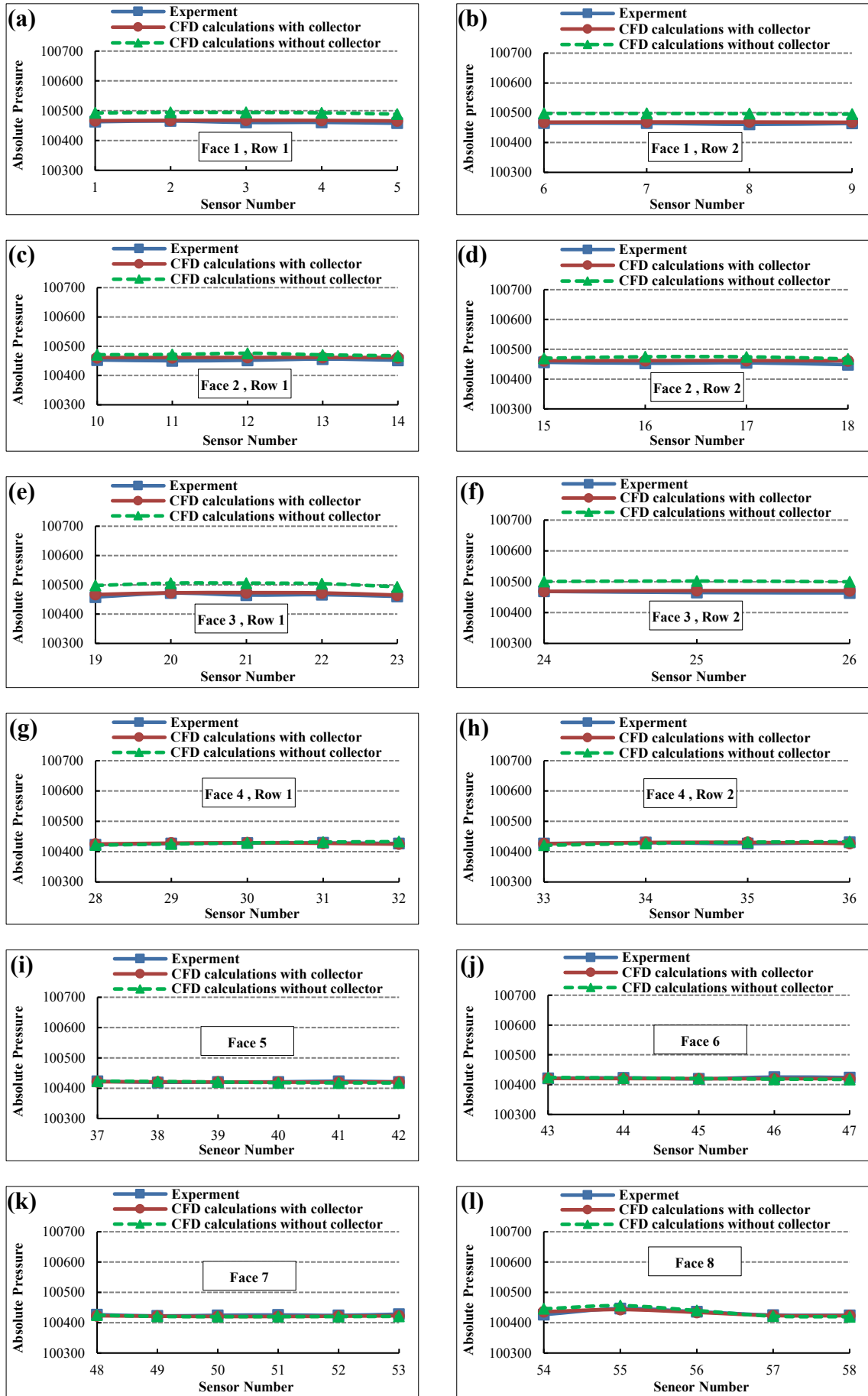


Figure 5.27 Pressure comparison at 0 degrees wind direction azimuth, 10 m/s

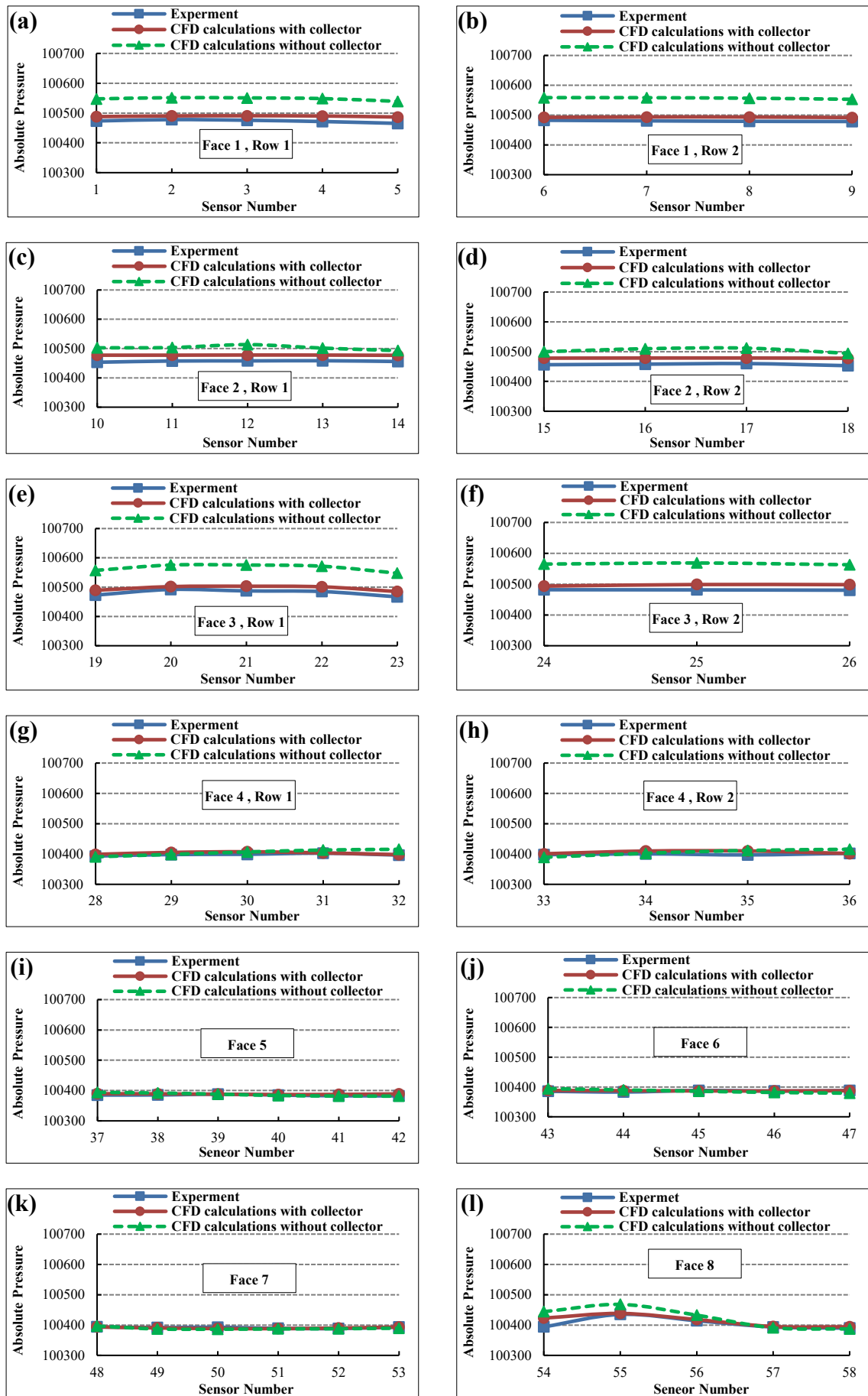


Figure 5.28 Pressure comparison at 0 degrees wind direction azimuth, 15 m/s

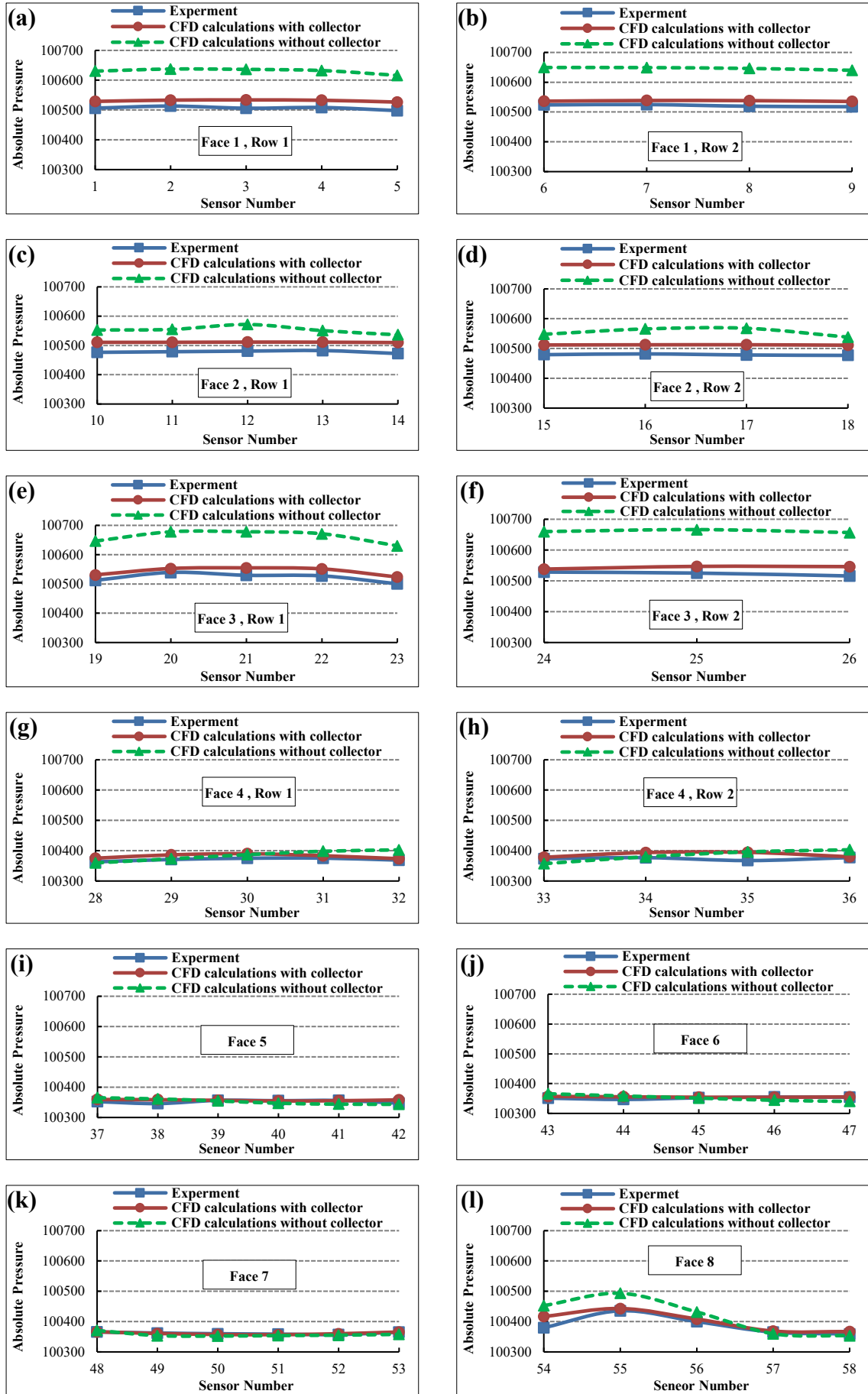


Figure 5.29 Pressure comparison at 0 degrees wind direction azimuth, 20 m/s

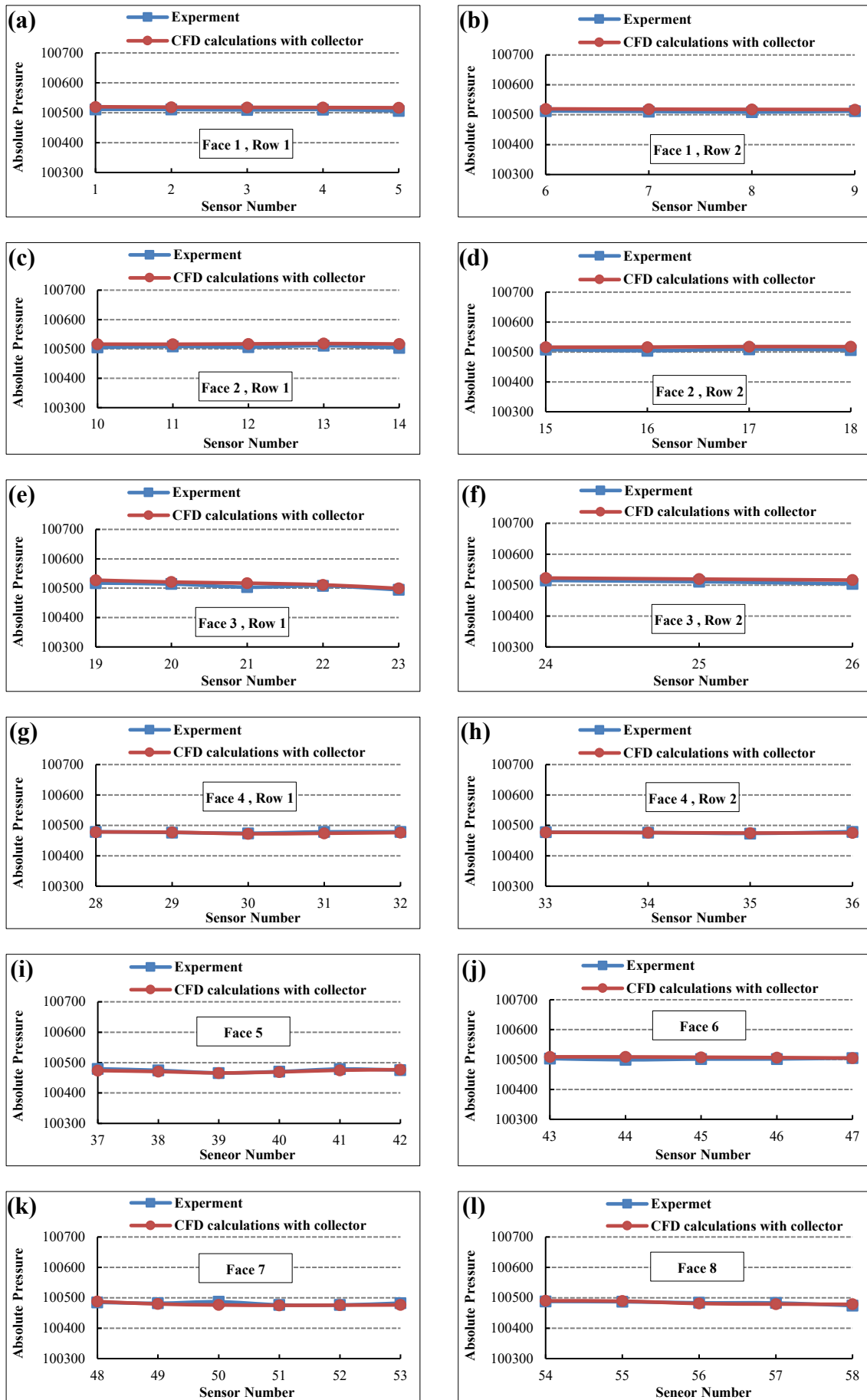


Figure 5.30 Pressure comparison at 45 degrees wind direction azimuth, 5 m/s

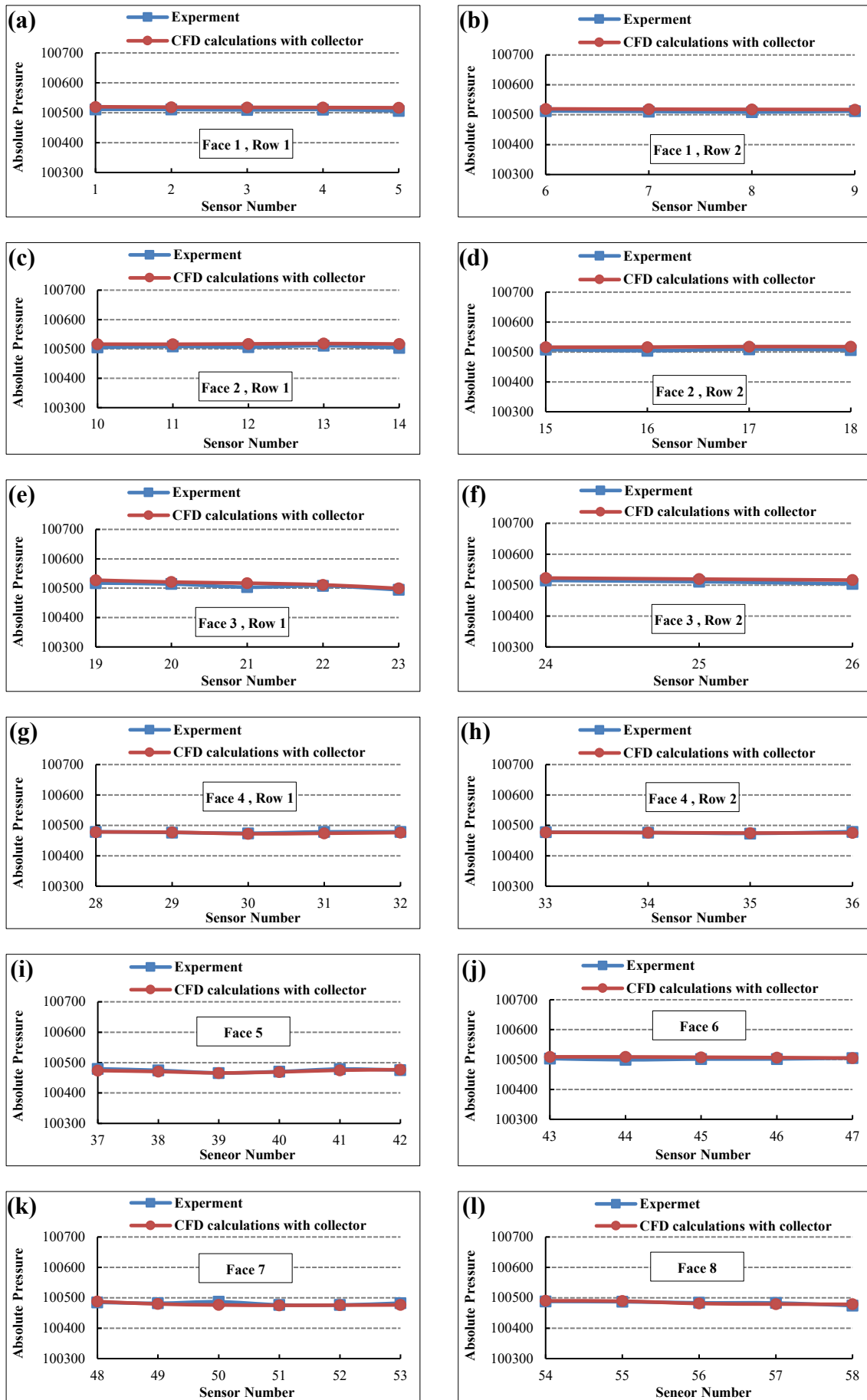


Figure 5.31 Pressure comparison at 45 degrees wind direction azimuth, 10 m/s

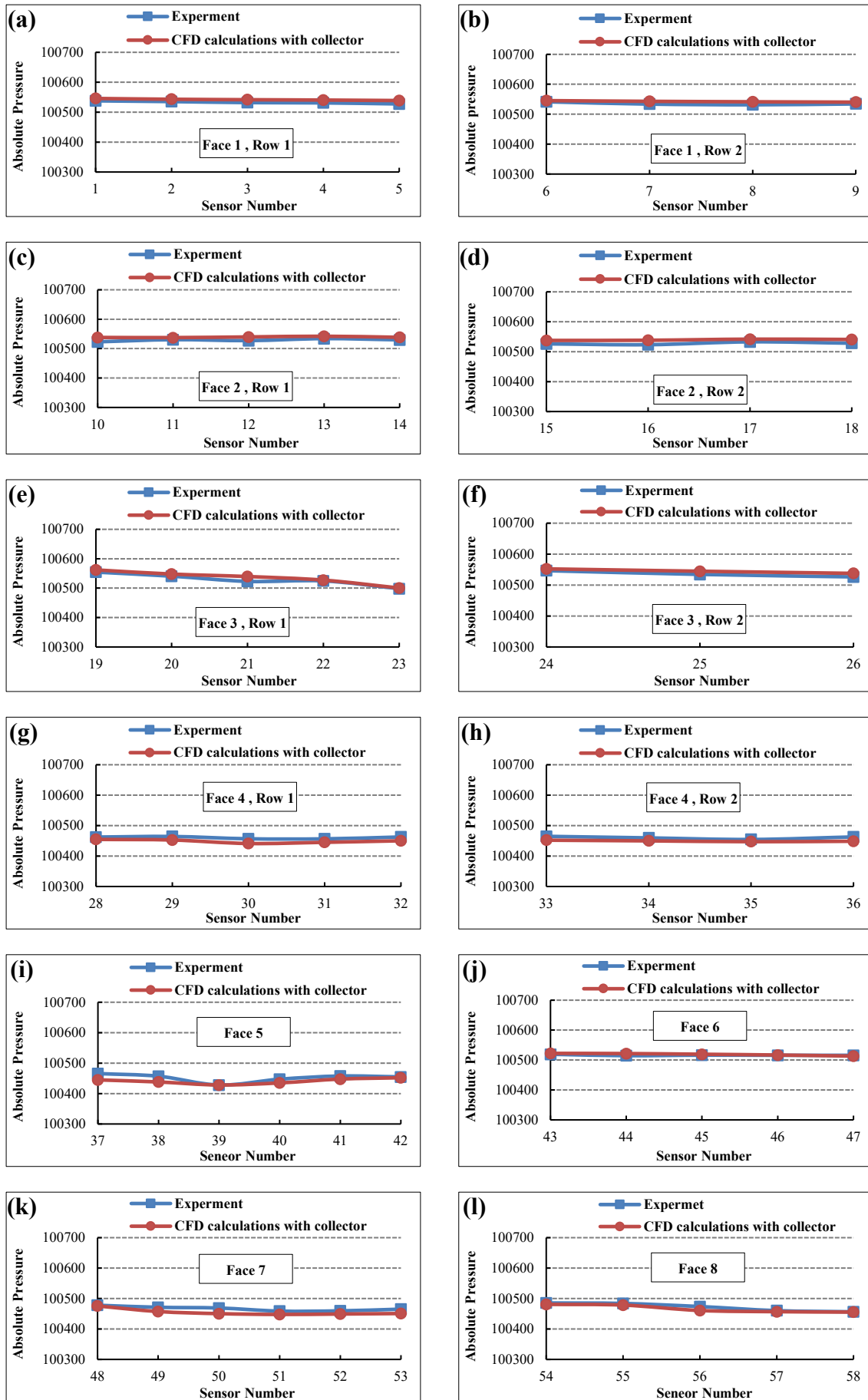


Figure 5.32 Pressure comparison at 45 degrees wind direction azimuth, 15 m/s

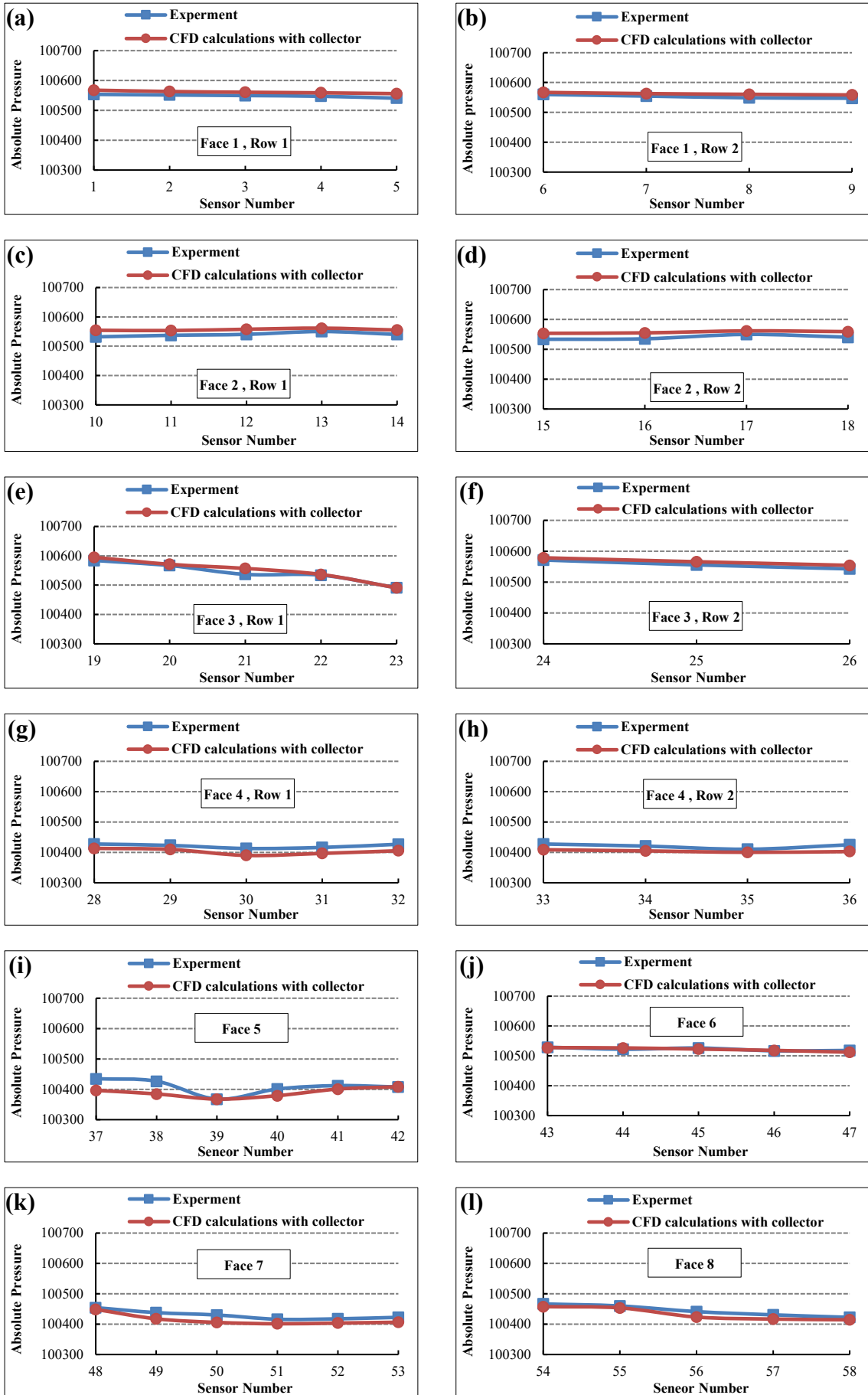


Figure 5.33 Pressure comparison at 45 degrees wind direction azimuth, 20 m/s

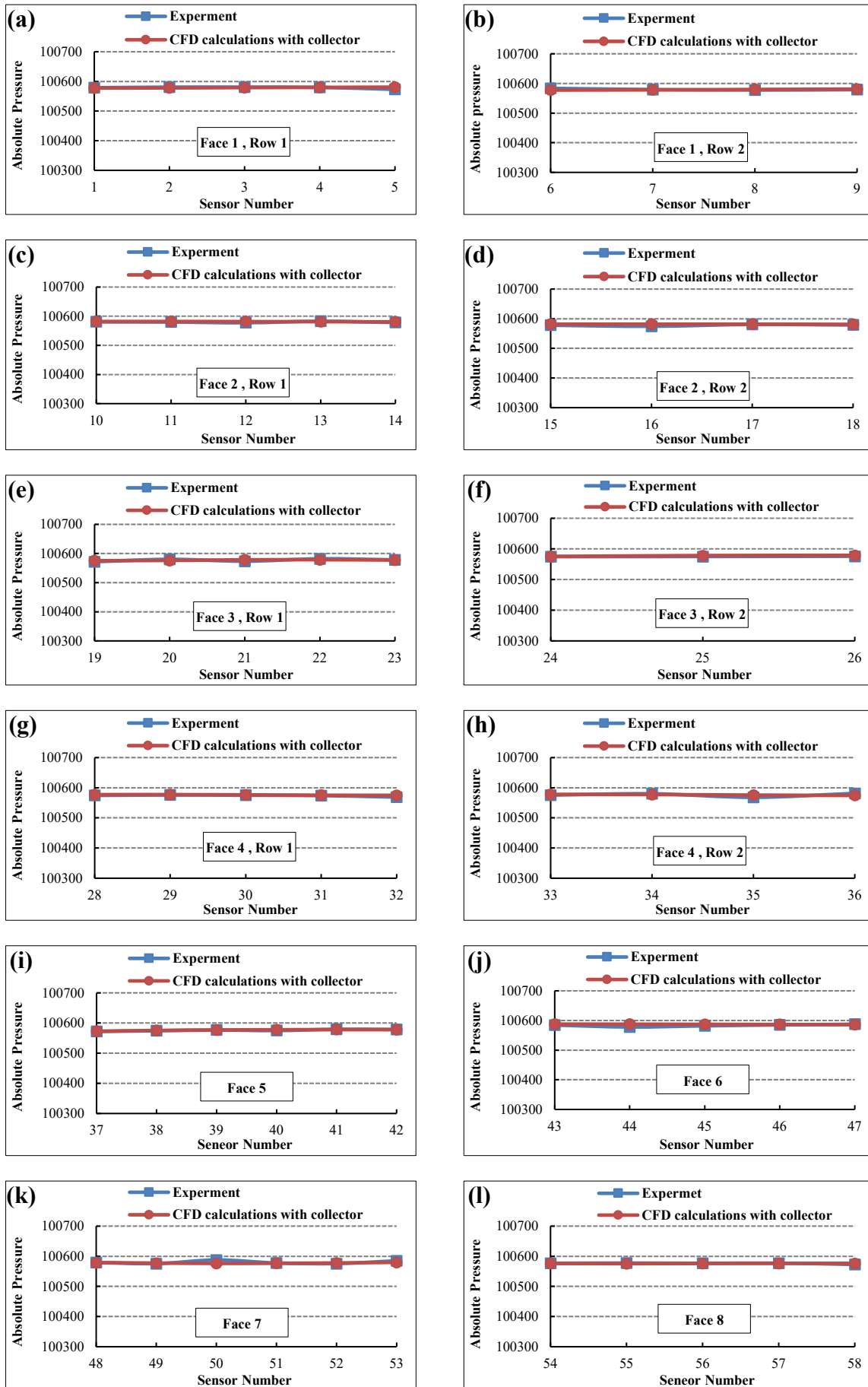


Figure 5.34 Pressure comparison at 90 degrees wind direction azimuth, 5 m/s

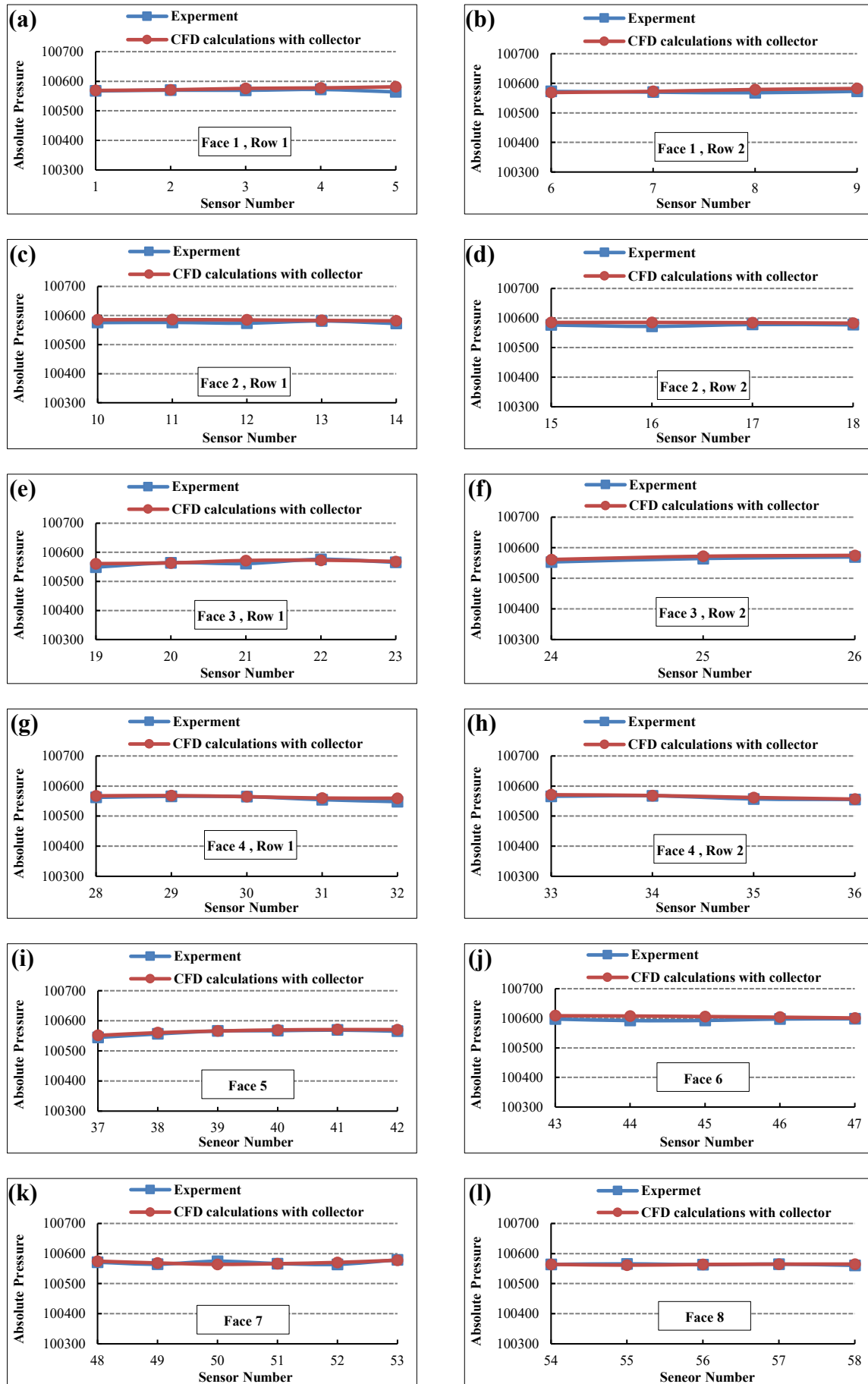


Figure 5.35 Pressure comparison at 90 degrees wind direction azimuth, 10 m/s

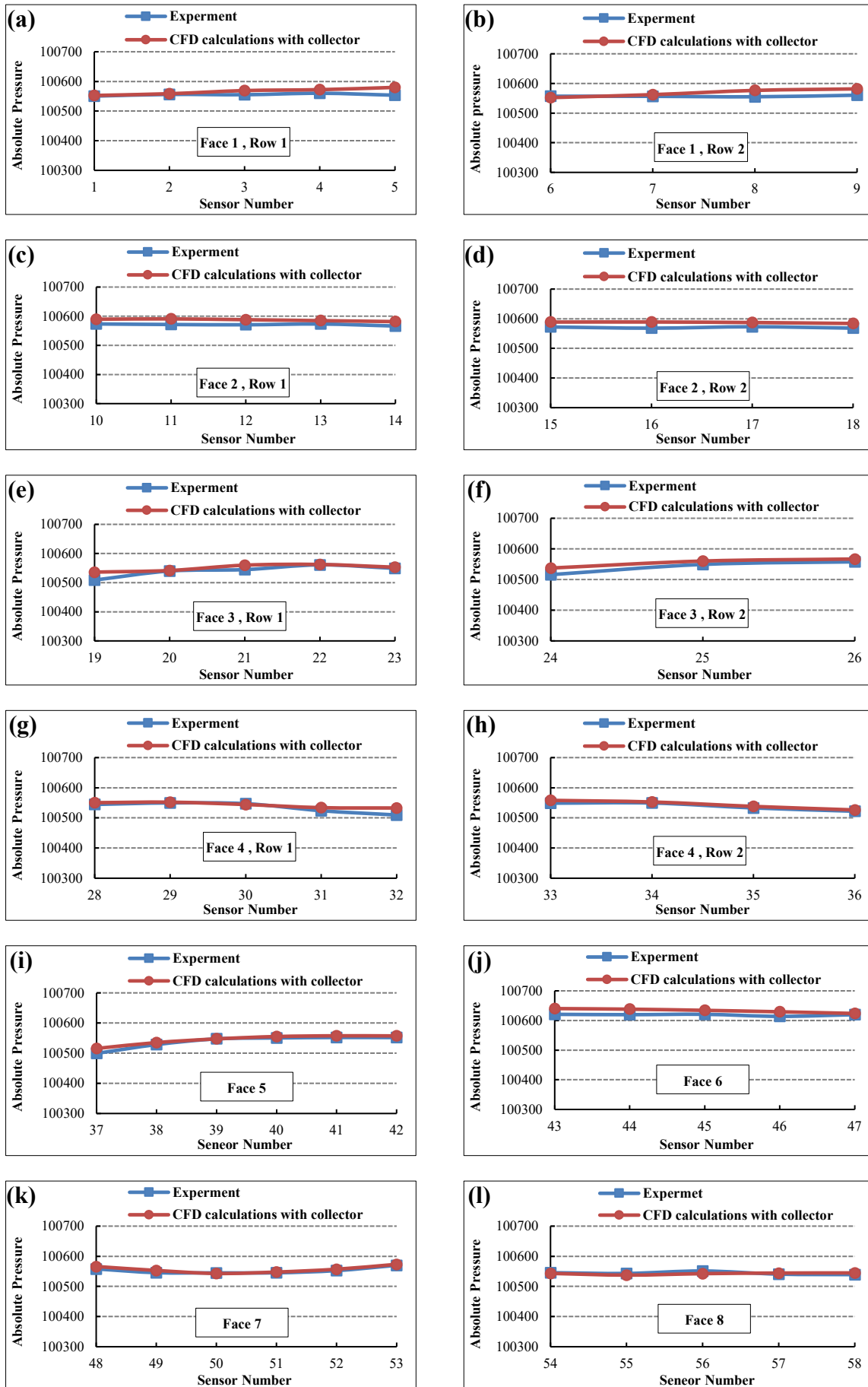


Figure 5.36 Pressure comparison at 90 degrees wind direction azimuth, 15 m/s

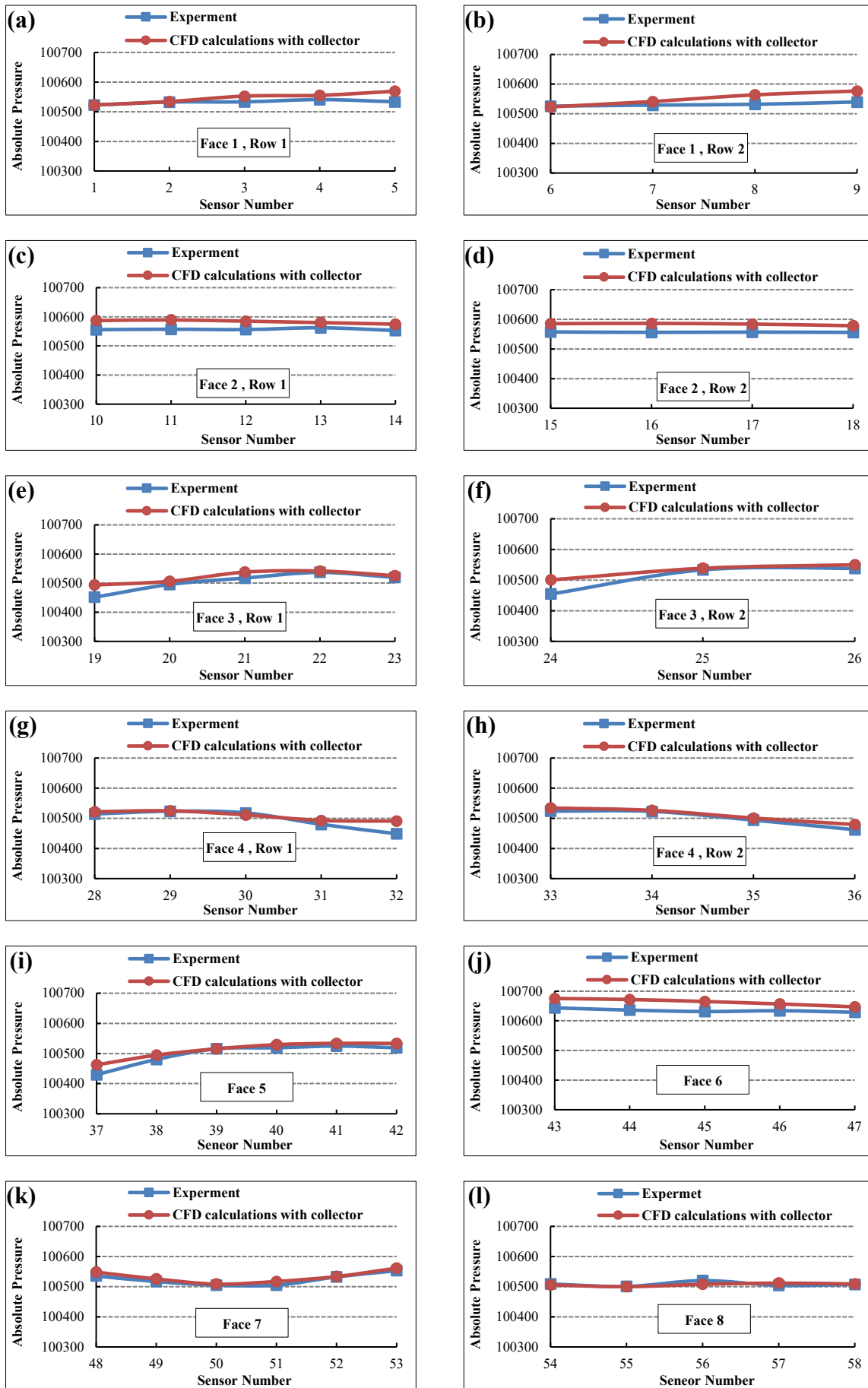


Figure 5.37 Pressure comparison at 90 degrees wind direction azimuth, 20 m/s

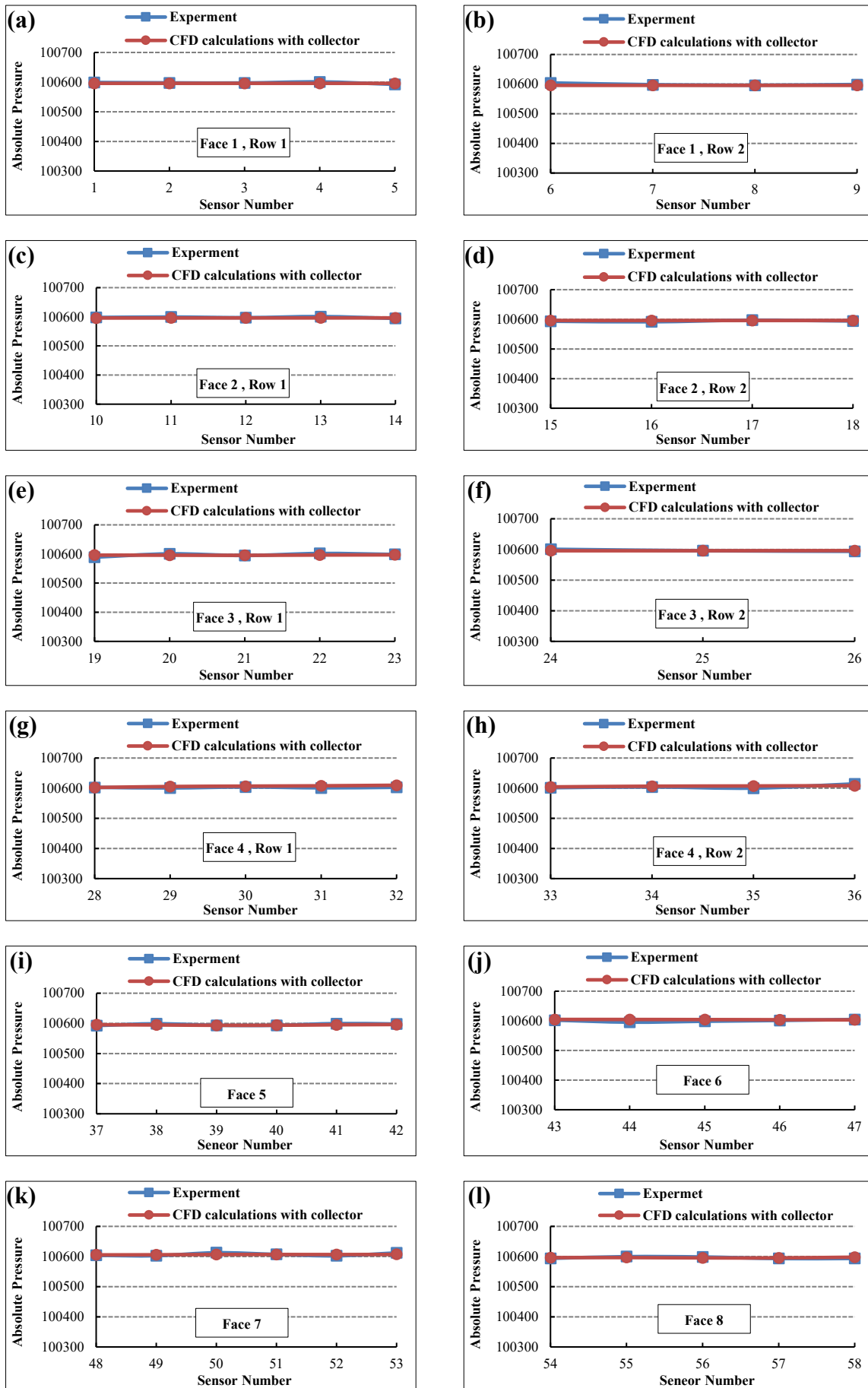


Figure 5.38 Pressure comparison at 135 degrees wind direction azimuth, 5 m/s

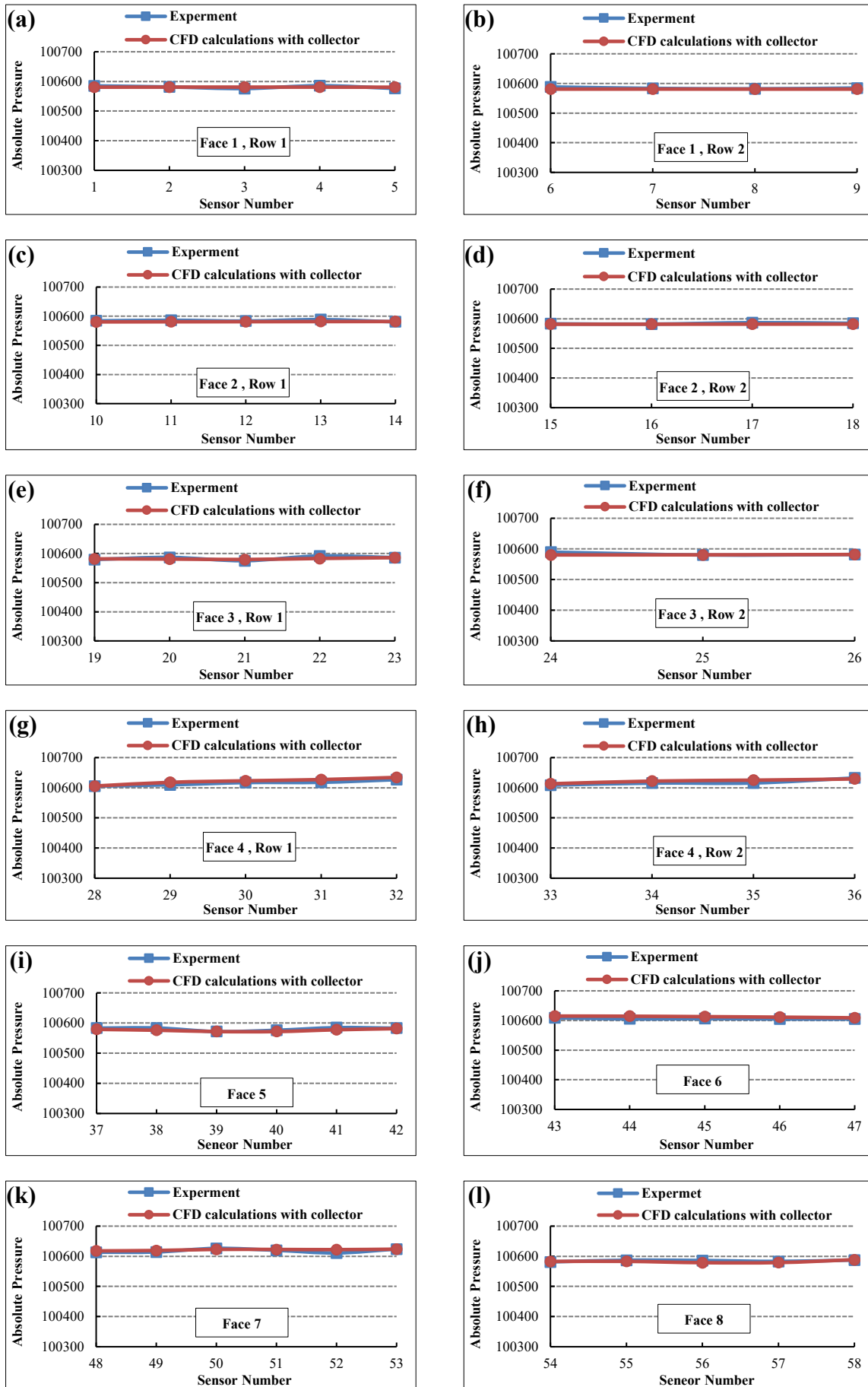


Figure 5.39 Pressure comparison at 135 degrees wind direction azimuth, 10 m/s

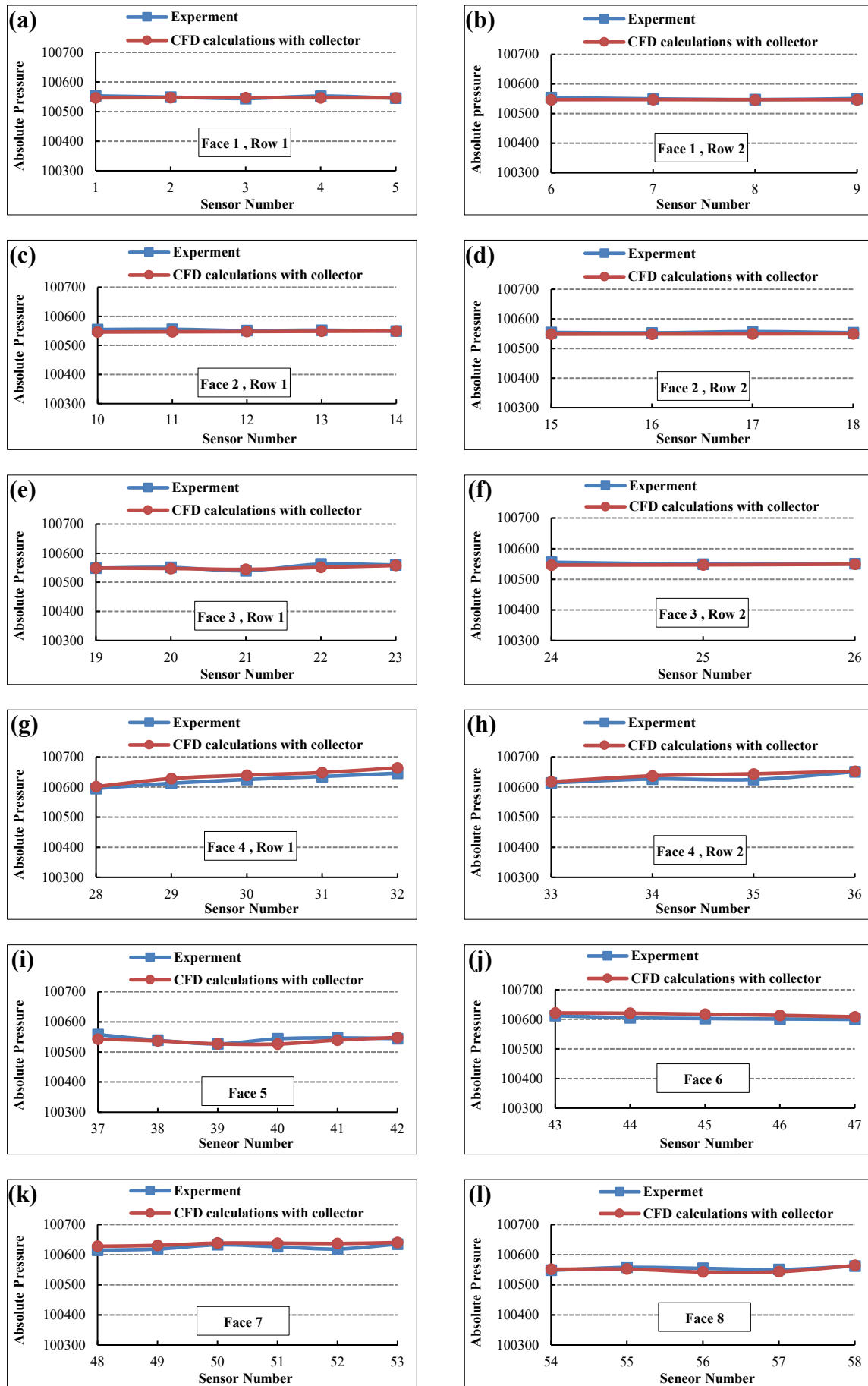


Figure 5.40 Pressure comparison at 135 degrees wind direction azimuth, 15 m/s

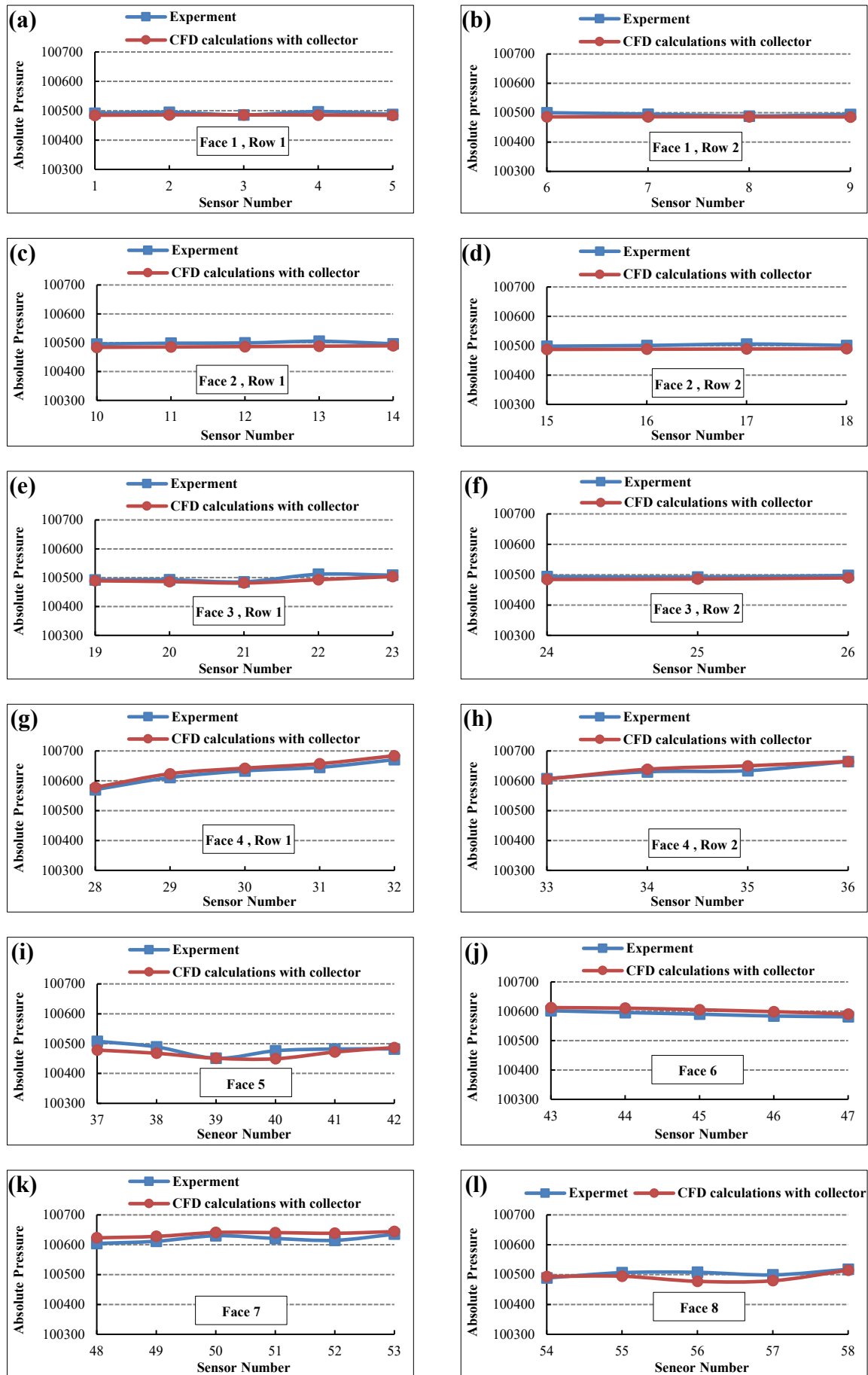


Figure 5.41 Pressure comparison at 135 degrees wind direction azimuth, 20 m/s

Figure 5.42 displays the distributions of local absolute pressure on the model building faces at zero wind direction azimuth for all four wind velocities. As the air velocity increases, the model faces are subject to higher pressure and suction.

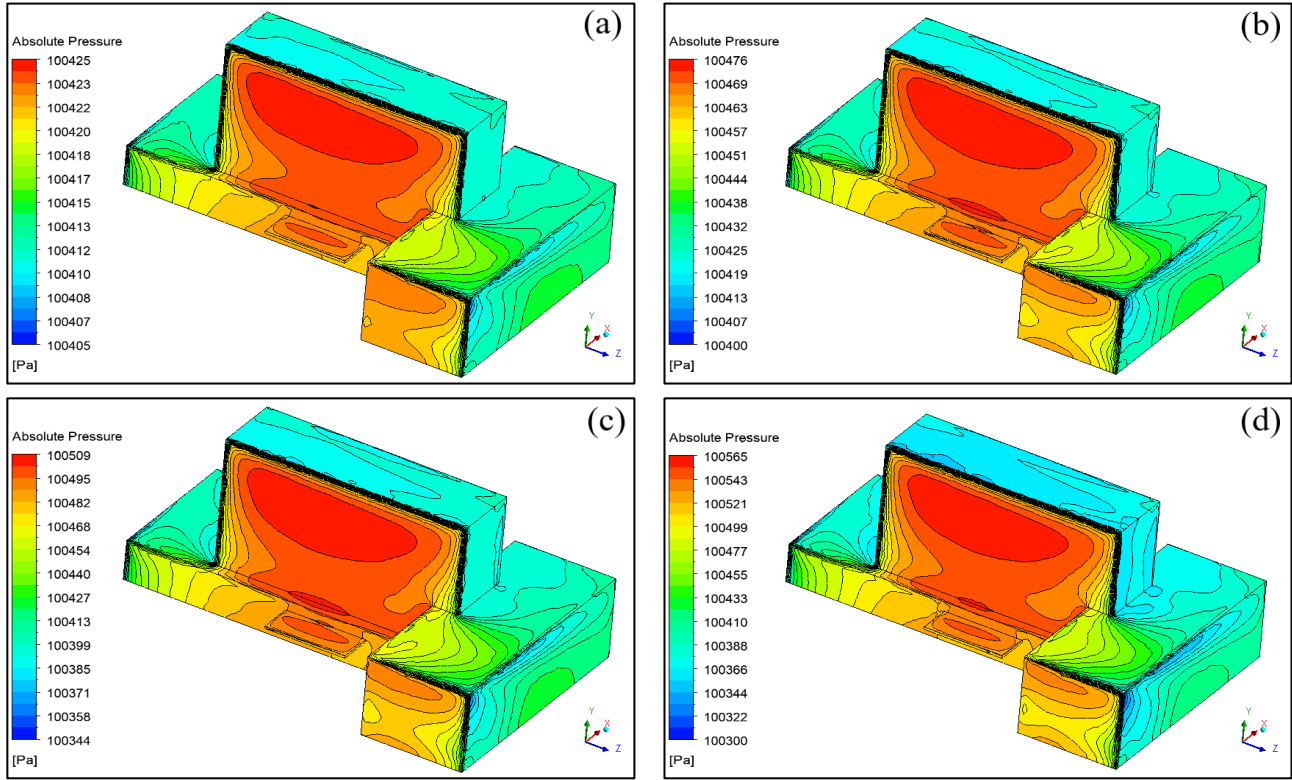


Figure 5.42 Absolute pressure contours at 0 degrees wind direction azimuth, (a) 5 m/s, (b) 10 m/s, (c) 15 m/s, and (d) 20 m/s

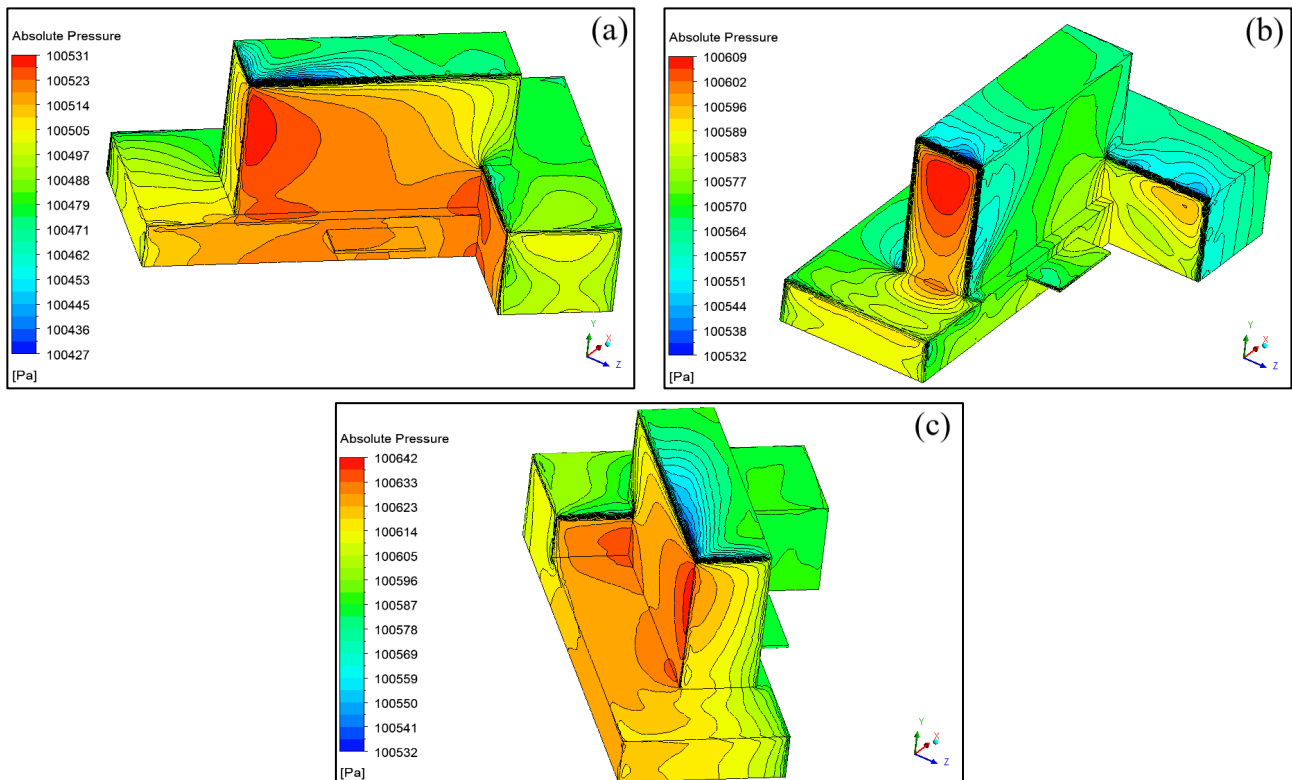


Figure 5.43 Absolute pressure contours at 10 m/s, (a) 45 degrees, (b) 90 degrees and (c) 135 degrees

Additionally, the combination of the flow separated above leading edges of the roof faces (7 and 8) with the flow vortex congregated in front of the face (3) edges cause extraordinary distributions of pressure on these roof faces, as shown in figure 5.42.

Figure 5.43 shows the distributions of local absolute pressure on the model faces at velocity 10 m/s for the other three wind direction azimuths. The effect of the conical vortices in the pressure distributions on the face (5) of the model can also be seen clearly in panels (a and c) when the flow is attached to the model at a skewed angle.

Figures 5.44, 5.45, 5.46, and 5.47 show the eddy viscosity distributions inside the wind tunnel test section at zero wind direction azimuth for all four velocities of wind. The higher and vast domain of eddy viscosity is generated behind the model until the reattachment zone, and then it is straightened to take the shape of the tube along the middle of the test section, and the diameter of this tube gets larger as the wind velocity increases.

Similarly, a horizontal plane at the canopy height was created and concentrated on showing the eddy viscosity distributions on the horseshoe vortex and the wake regions around the building.

Figures 5.48, 5.49, and 5.50 show the eddy viscosity distributions inside the wind tunnel test section at a velocity of 10 m/s for the other three wind direction azimuths. The higher and vast domain of eddy viscosity is also generated behind the building until the reattachment zone, and then it is straightened to take the shape of the tube. This domain is spreading along the middle of the test section when the flow normal to the building, as shown in Figure 5.49. On the other hand, it is spreading along the test section with an angle depending on the model's geometrical shape and wind direction azimuth, as shown in figures 5.48, and 5.50.

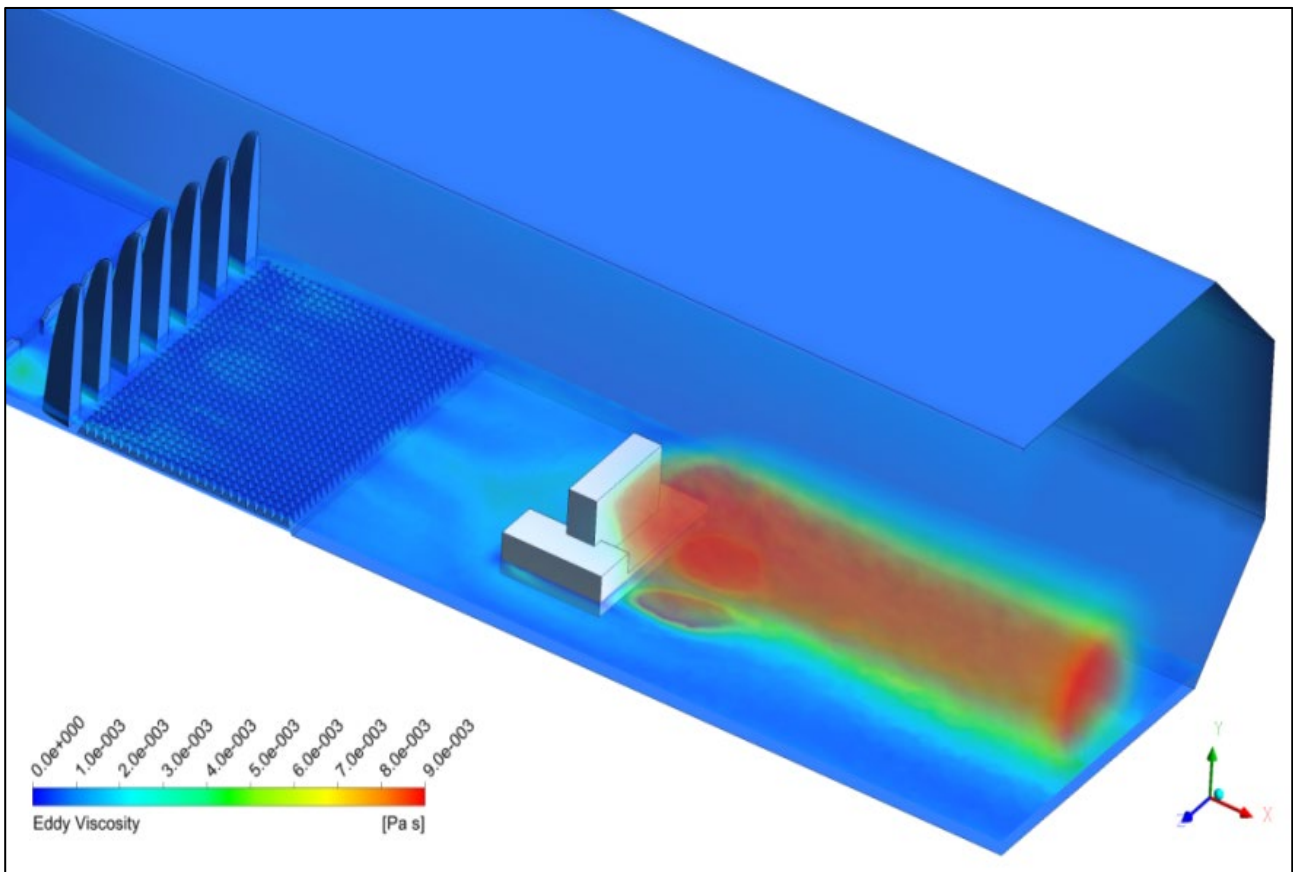


Figure 5.44 Eddy viscosity at 0 degrees wind direction azimuth, 5 m/s

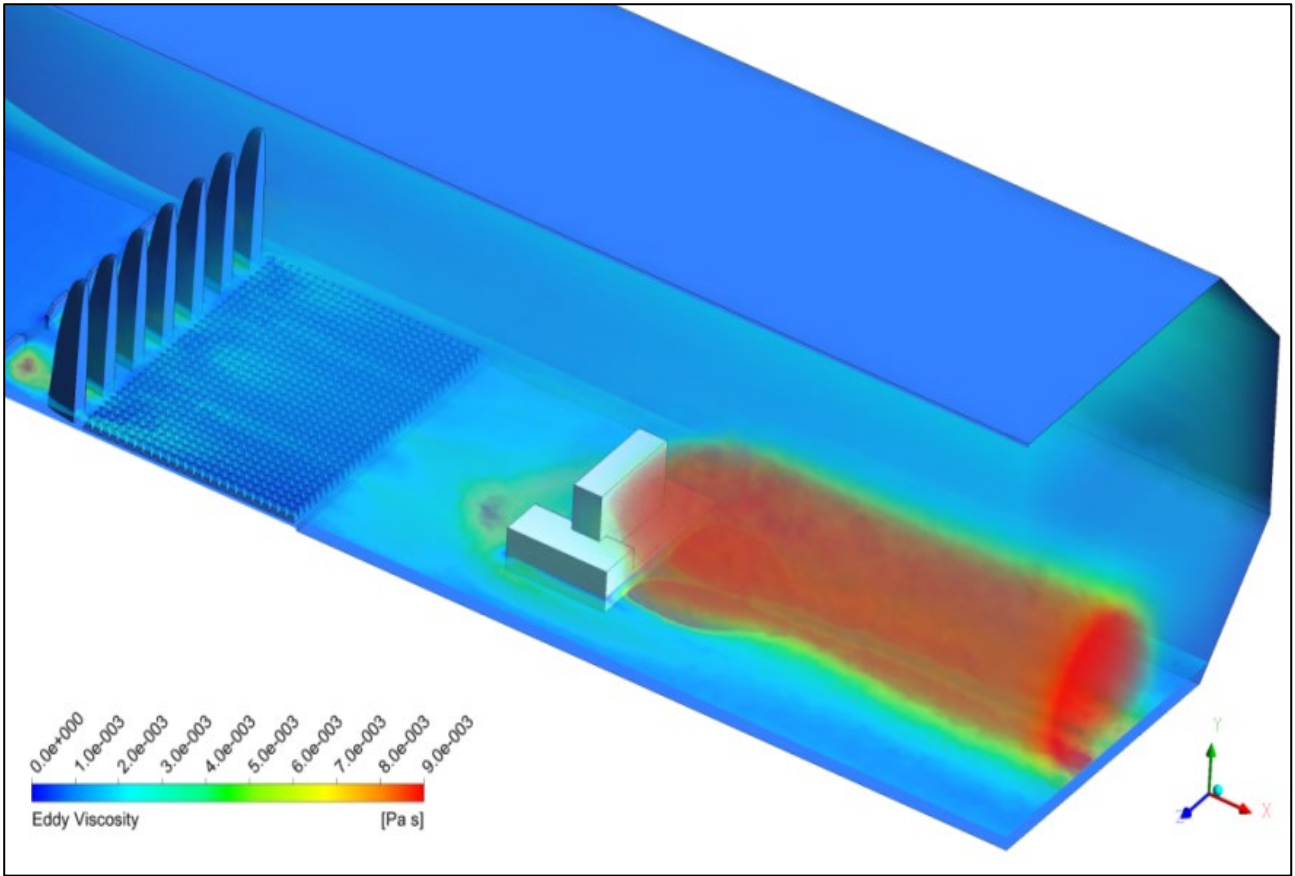


Figure 5.45 Eddy viscosity at 0 degrees wind direction azimuth, 10 m/s

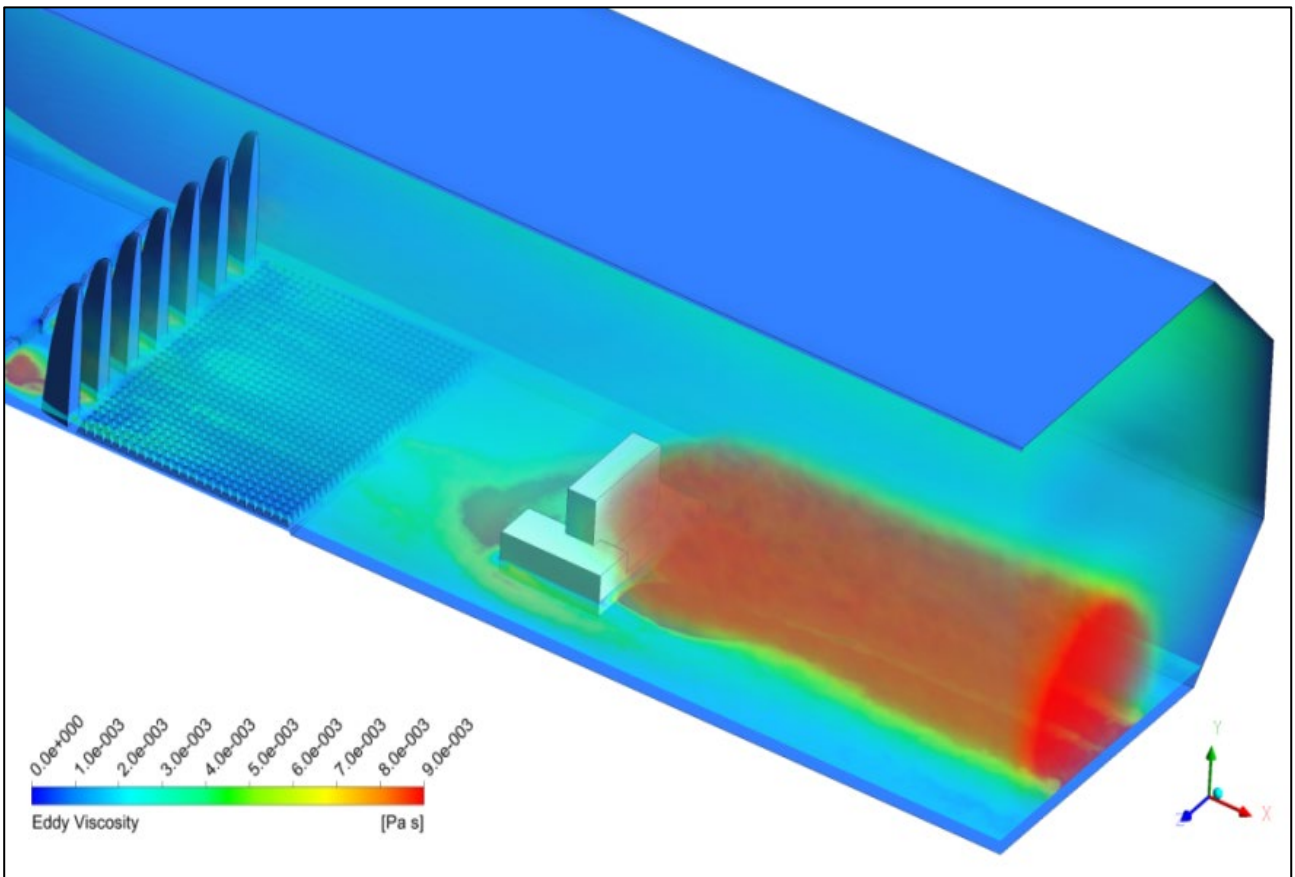


Figure 5.46 Eddy viscosity at 0 degrees wind direction azimuth, 15 m/s

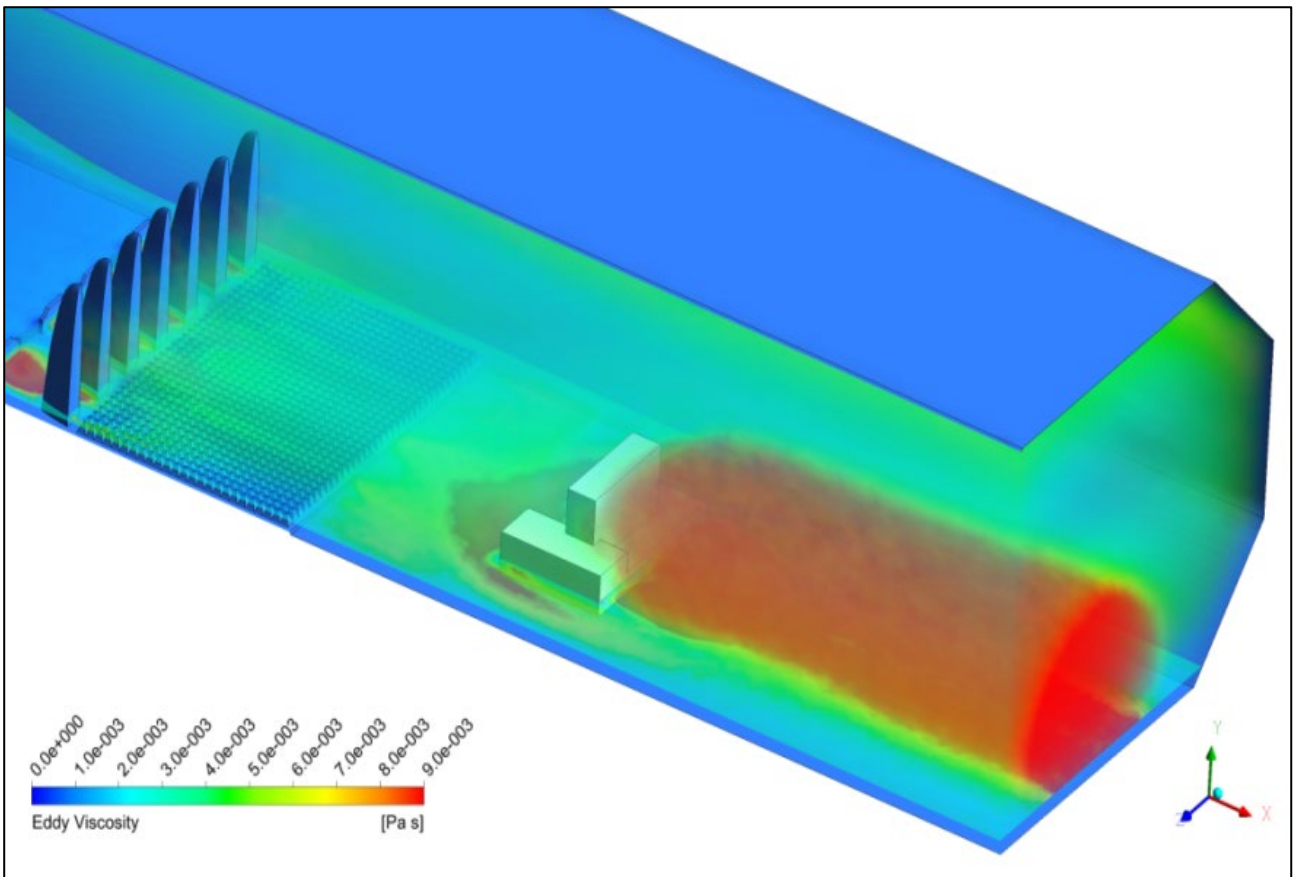


Figure 5.47 Eddy viscosity at 0 degrees wind direction azimuth, 20 m/s

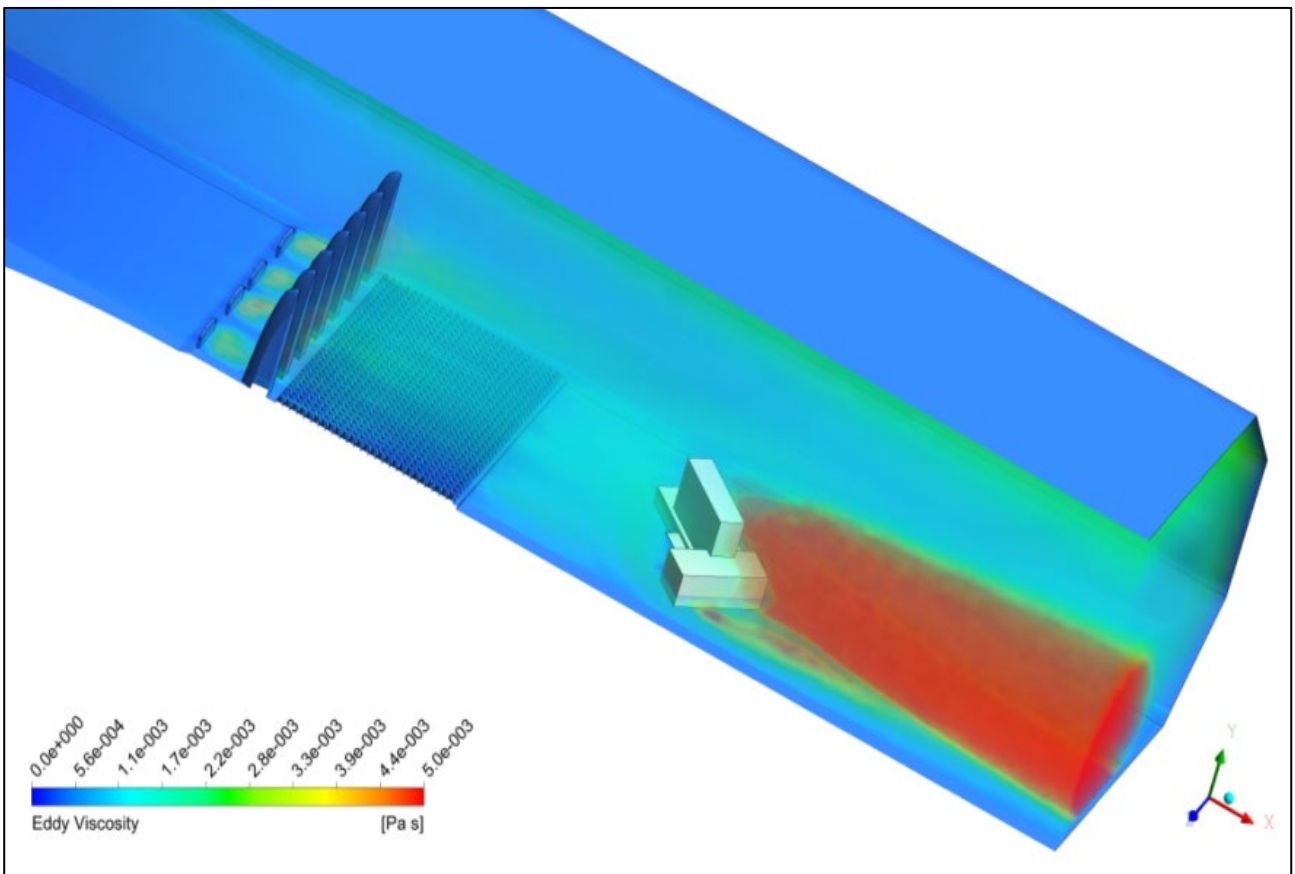


Figure 5.48 Eddy viscosity at 45 degrees wind direction azimuth, 10 m/s

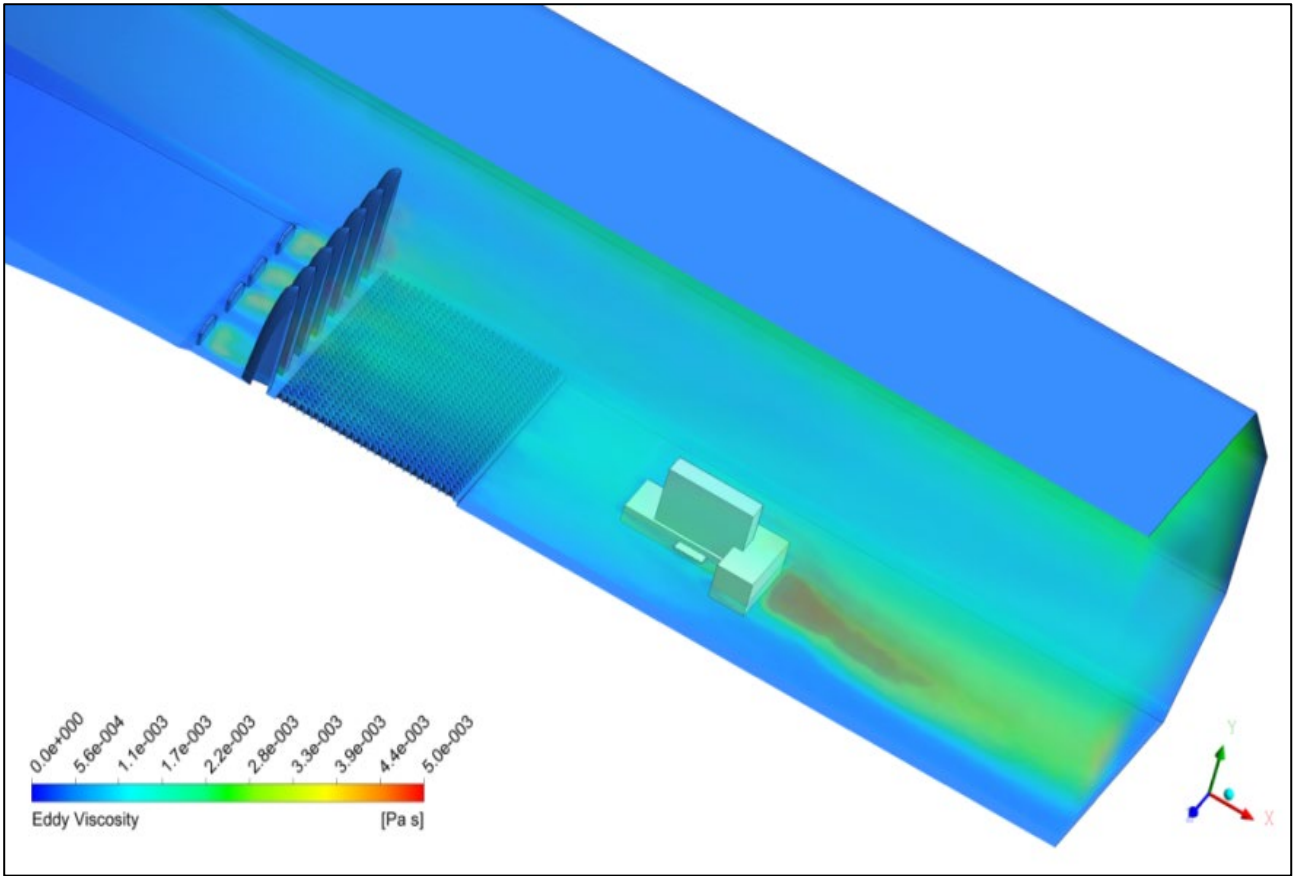


Figure 5.49 Eddy viscosity at 90 degrees wind direction azimuth, 10 m/s

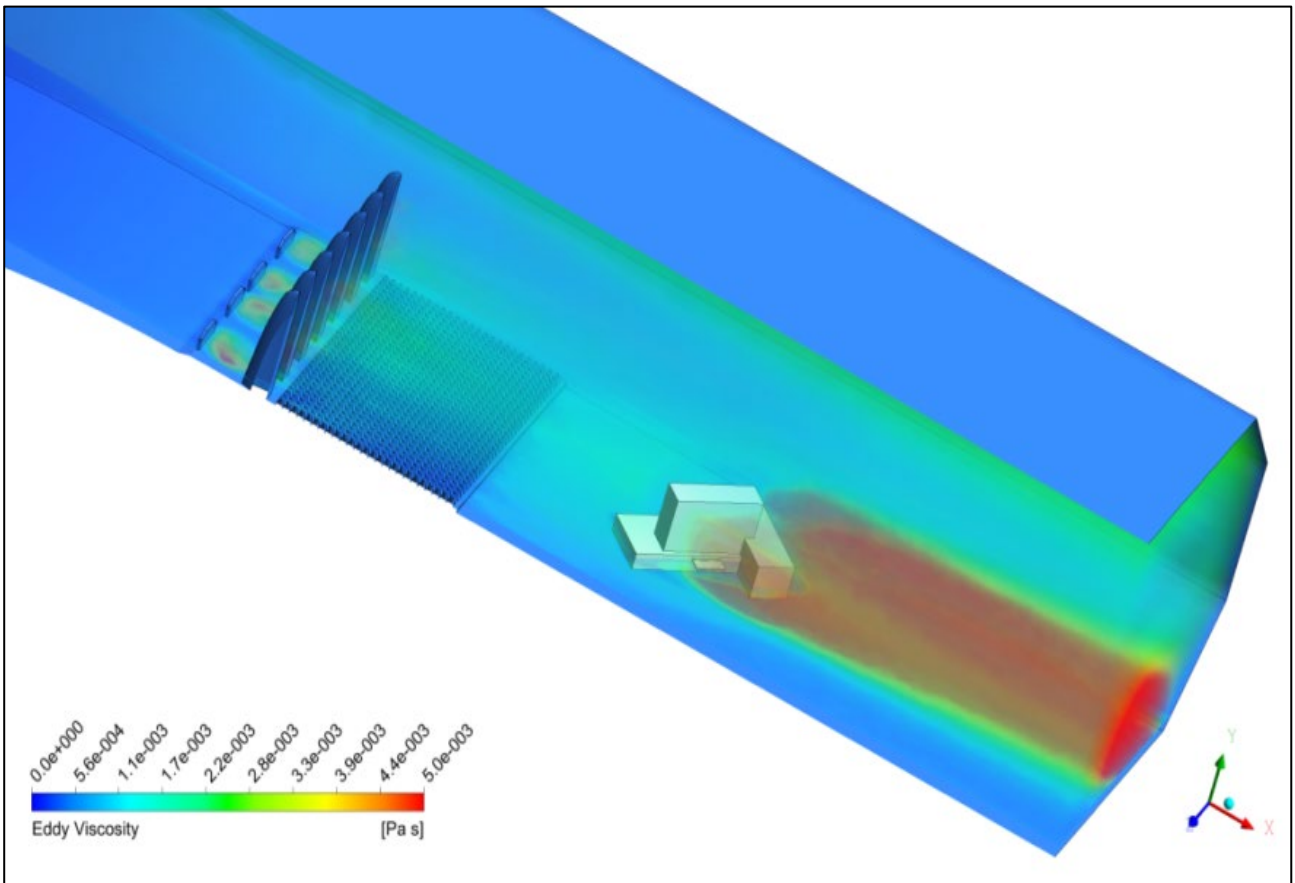


Figure 5.50 Eddy viscosity at 135 degrees wind direction azimuth, 10 m/s

CHAPTER 6: NUMERICAL ANALYSIS OF LOW-RISE BUILDINGS

In this chapter, the numerical analysis by CFD was performed for several low-rise buildings placed at the Belgrade University virtual wind tunnel. For validation of the same CFD model used in this thesis, the pressure coefficients obtained by CFD on the faces (walls and roofs) of the buildings were compared with the pressure coefficients that were documented in the available and suitable wind standard and code.

6.1 Wind Standards and Codes

There are several national standards developed by various countries to evaluate wind loads on the structures. These wind loads are used by engineers to design different safety shapes and types of structures, and they require the pressure coefficients or the force coefficients for different structural elements with site certain wind data and terrain characteristics to regulate them.

In general, the wind standards present different pressure coefficients, which are confirmed from full scale experiments or boundary layer wind tunnel tests and a few of them by using numerical simulations. Also, the standards did not cover all shapes and sizes of the buildings, and they need to list those missed data for updates and improvement.

However, the standards and codes are different in their approaches for calculating the pressure coefficients on the structures. The wind velocity profiles for the open country exposure in different wind standards/codes are quite dissimilar, although the basic wind speed in all of them is defined at 10 m above the ground surface in this exposure [1].

Four of the most used standards by the design engineering and researchers are presented here:

1. American Society of Civil Engineering Standard (ASCE 7-16) [98],
2. European Standard (EN 1991-1-4:2005) [99],
3. Australian/New Zealand standard (AS-NZS 1170-2, 2011) [100],
4. National Building Code of Canada (NBCC, 2010) [101].

These standards were used together by Alrawashdeh [1], who measured local external pressure coefficients on the roof of nine flat low-rise buildings with different large dimensions at the wind tunnel of Concordia University. The experimental results were compared with the respective values specified in these four standards.

The 1st, 3rd, and 4th standards were used by Kola [102], who compared these three standards with the British standard by evaluating the external and internal pressure coefficients to defined the wind loads on the faces of flat roof low and high-rise buildings.

The 1st and 3rd standards were used by John et al. [103], who measured the external pressure coefficients on the front and side walls of 25° gabled roof low-rise building due to interference with a free standing boundary wall placed on the upstream side at different locations. The experimental results from the ABL wind tunnel at the Indian Institute of Technology Roorkee are compared with the listed values in these two standards, as well as with the Indian standard code and the Hong Kong standard.

Also, the first standard only was used by John et al. [104], who measured the external pressure coefficients at different zones on the roof of the same 25° gable low-rise building in the presence of a free standing wall and compared the results with this standard.

The 1st and 2nd standards were used by Kayışoğlu [105], who measured the external pressure coefficients on the faces of the high-rise building in Ankara Wind Tunnel to calculate static loads. The results of static loads compared with these two standards and the İstanbul Yüksek Binalar Rüzgar Yönetmeliği (İybry, 2009).

The 1st and 2nd standards were used by Fouad et al. [106], who calculated the external pressure coefficients by the CFD technique on the roofs of (15°, 30°, 45°, and 60°) gable low-rise buildings when the wind incident angle ($\theta = 0^\circ$, and $\theta = 90^\circ$), and on the roofs of (15°, 30°, 45°, and 60°) mono-slope low-rise buildings when the wind incident angle ($\theta = 0^\circ$, $\theta = 90^\circ$, and $\theta = 180^\circ$),

and on latticed structure surfaces. Then the obtained CFD results are compared with these two standards. Also, they calculated and compared the external pressure coefficients using the CFD technique at different zones on the dome surface of five domed roof low-rise buildings with the 2nd standard.

The 1st and 3rd standards were used by Suárez [107], who measured the local and net pressure coefficients at two canopy models attached to the gabled roof low-rise building in the Building Aerodynamics Laboratory of Concordia University. Then the experimental results are compared with provisions of these two standards.

All standards and codes propose the pressure coefficients of the buildings at open country exposure, and they offer the exposure coefficients for other exposure categories. These pressure coefficients are documented in each standard in a different form contingent on other factors.

Some key data and parameters that specify each of these four standards and manipulate the pressure coefficients are summarized in Table 6-1, which includes the data from which references have been taken.

Table 6-1 The key parameters that affect the values of pressure coefficients in the four standards

	ASCE 7 2016	EN 1991-1-4 2005	AS-NZS 1170-2 2011	NBCC 2010
Wind velocity profile	Logarithmic law Power law ^[1,98]	Logarithmic law ^[1,99]	Logarithmic law ^[1,100]	Power law ^[1,101]
Power exponent (α) for open country exposure	1/6.5 ^[98,108]	—	—	0.16 ^[108]
roughness length (z_0) for open country exposure when ($\alpha=0.15$)	0.048 ^[109]	0.05 ^[99,109]	0.02 ^[100,109]	0.025 ^[109]
turbulence intensity at 10 m height	20% ^[98,110]	18.87% ^[99,110]	18.3% ^[100,110]	20% ^[101,110]

6.2 Generate the Required ABL on the Belgrade University Virtual Wind Tunnel

The passive devices at the Belgrade university virtual wind tunnel were redesigned to generate an open country exposure in its test section, where the low-rise buildings will be placed according to the available key parameters for one of the previous four standards. The CFD procedure was used for this purpose and to calculate these key design parameters.

6.2.1 Redesign of the passive devices on the Belgrade University Virtual Wind Tunnel

The spires were only redesigned with keeping the same roughness elements after discarding the barrier walls for achieving the open country exposure category in the short test section of the Belgrade university virtual wind tunnel, as several researchers defined [105,108,111].

The object of the redesign is to obtain the desired Power exponent (α) and roughness length (z_0) for open country exposure in the central of the short test section. They are proportional to those specified by the four standards above.

A small scale factor (1/250) was assumed to result in boundary layer thickness $\delta = 1.097$ m on the test section considering the atmospheric boundary layer thickness for open country exposure in

nature $\delta_{nature} = 274.32$ m, [98]. This desired boundary layer thickness is approximately $0.55 H$, where H is the test section height. For example, if a low-rise building with a 10 m height was placed on the test section floor, it would be evident in the test section.

However, Farrell et al. [26] and Rahmat et al. [112] suggested that the boundary layer thickness produced by elliptical spires is 20% deeper than that produced by triangular spires with an equivalent height. Kayışoğlu [105] designed triangular spires for the open sea, open country, and suburban exposure categories in Ankara Wind Tunnel (AWT) using the procedure of Simiu et al. [108]. The AWT is a closed circuit wind tunnel with a 3.05×2.44 m octagonal test section and a 6.1 m length.

The elliptic spires were designed at the test section inlet by using an empirical procedure that combines the methods suggested in [26,105,112]. While the desired boundary layer thickness by the elliptic spires desires to be $\delta_{elliptic} = 1.097$ m, the design boundary layer thickness by the triangular spires should be $\delta_{triangular} = \delta_{elliptic} / 1.2 = 0.91$ m.

The ratio of base width to height of triangular spire (b/h_s) was estimated from Figure 6.1 in [108] by using the height of our virtual wind tunnel test section H with the desire Power exponent ($\alpha = 0.15$) and $\delta_{triangular}$.

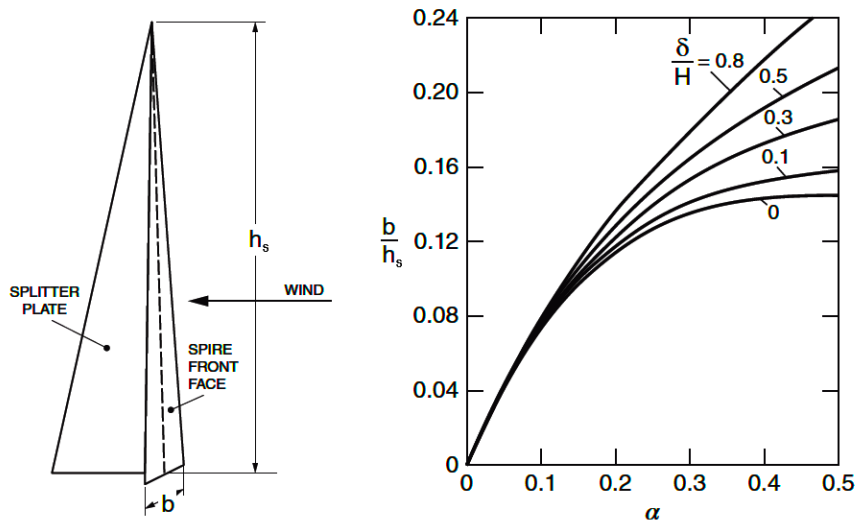


Figure 6.1 Spire base width variation with the power law exponent (Simiu et al., 1978)

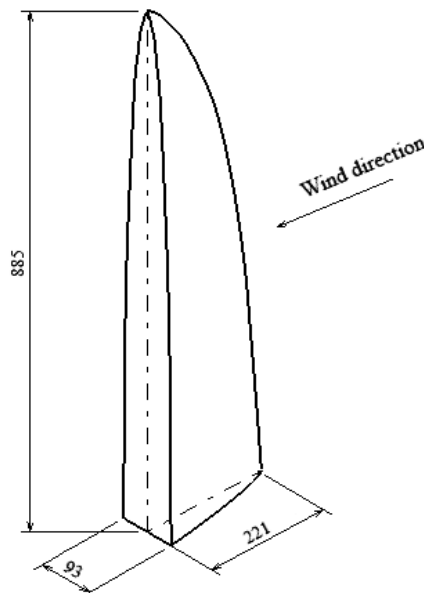


Figure 6.2 The elliptic spire model, dimensions in mm

The spire base width was then estimated by assuming the triangular spire height $h_s = 0.885$ m, as the same used height in AWT [105]. Considering this spire height is generating the power exponent as our desired power exponent, it also relies on the AWT test section dimensions close to the dimensions of our virtual wind tunnel test section.

A Splitter width is a quarter of the spire height, and the number of spires is imposed by the lateral distance of the splitter plate, which is half of the spire height, so the dimensions of the used elliptic spire related to the designed triangular spire are shown in Figure 6.2 above.

6.2.2 Numerical Simulation for the Empty Virtual Wind Tunnel with the New Design of the Passive Devices

The three designed elliptic spires were modeled at the test section inlet and followed by the same configurations of the roughness elements. The computational domain size was half of the collector with the test section due to their symmetry, and the unstructured mesh was generated by the same procedure used in the previous chapter with mesh size 0.5 cm for the test section floor instead of 1 cm. Totally number of elements for the computational domain is 3,104,031. The unstructured mesh is shown in Figure 6.3.

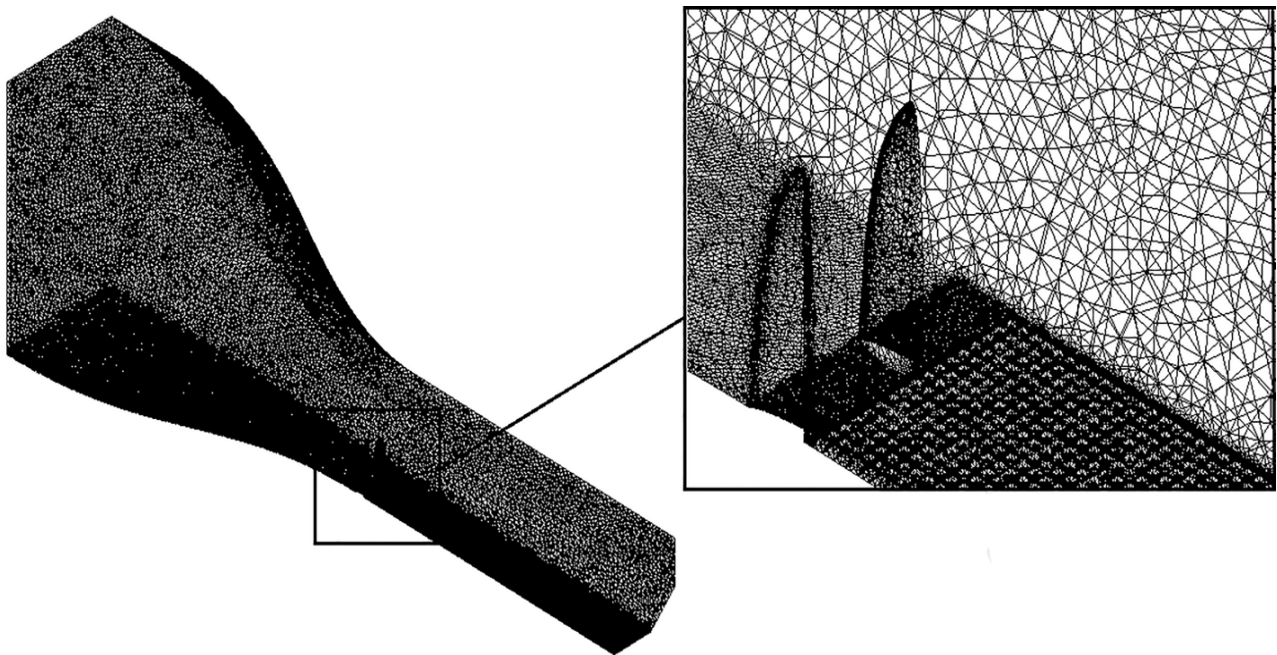


Figure 6.3 The unstructured mesh for the computational domain

The same solver of RANS equations, turbulence model, solution method, and outlet boundary condition, as described in the previous chapter, were used. The ‘inlet velocity’ boundary condition was set at 1.459 m/s at the collector inlet, which corresponds to 10 m/s at the inlet of the wind tunnel test section. The solution convergence was reached while the mass flow rate at outlet remained steady in the solution monitor, and the convergence criterion was set to about 10^{-6} .

As a result, the velocity and turbulence intensity profiles in the central of the test section are shown in Figure 6.4, where the boundary layer thickness $\delta = 1.095$ m, and the Power exponent is $\alpha = 0.145$.

Also, the same indirect method used in chapter three was used to determine the values of the roughness length ($z_0 = 0.0000803$ m). The height curve fitting between predicted and calculated height z at the same value of calculated velocity is shown in Figure 6.5.

Therefore, the parameters α and z_0 calculated by CFD are closer to that presented in Table 6-1 for the Australian/New Zealand AS-NZS 1170-2 standard when the scale factor (1/250) was used in our virtual wind tunnel. One should note that the similarity in turbulence levels rarely can be satisfied in short wind tunnels [105].

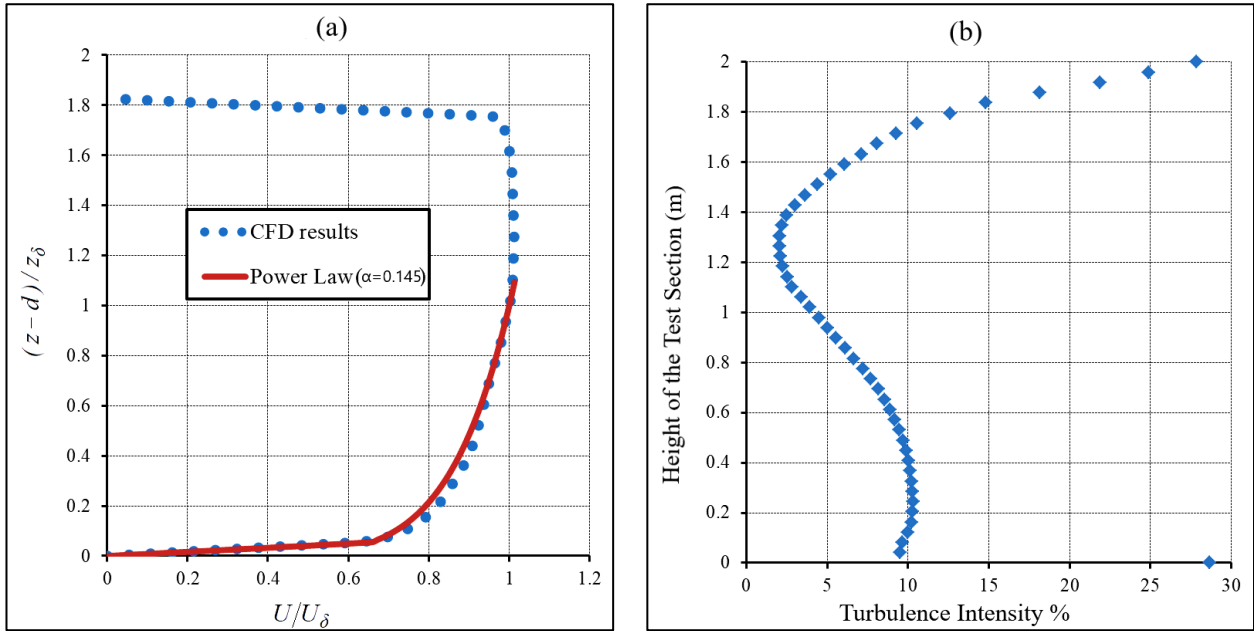


Figure 6.4 (a) Wind velocity profiles, (b) Turbulence intensity profile

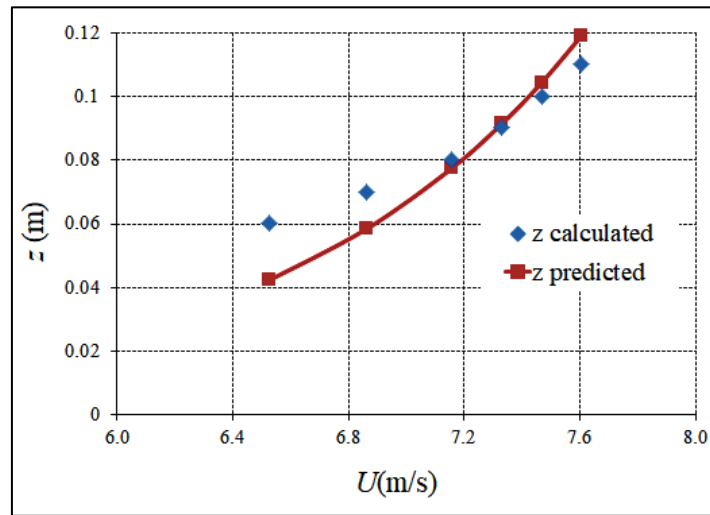


Figure 6.5 The best curve fitting for the height z

6.3 Numerical Simulation of the Low-rise Buildings

Three types of low-rise buildings were chosen for this study. They are the gabled roof, mono-sloped or a shed roof, and curved roof low-rise buildings. They were positioned in the central of our virtual wind tunnel test section while the wind direction was perpendicular to their width.

The CFD simulations were performed to predict the pressure coefficients on the faces (walls or roofs) of every building and compare these coefficients with those given by the Australian/New Zealand standard to verify and validate the established CFD model.

6.3.1 Modeling the Low-rise Buildings

The three chosen types of low-rise buildings have a same average roof height ($h = 10$ m) with different base dimensions: width (d) is parallel to wind direction, length (b) is normal to wind direction. Also, with different roof pitch (β) that is (symbolized as α in Australian/New Zealand standard) for the gabled and mono-sloped roof buildings, and specified rise of an arch for the curved roof building is (r).

The scale factor (1/250) was chosen for modeling the three buildings, according to the matching of the Jensen number in the simulated boundary layer in the wind tunnel with a natural boundary layer:

$$J_m = J_n \Rightarrow \frac{h_m}{z_{0m}} = \frac{h_n}{z_{0n}} \Rightarrow \frac{h_m}{0.0000803} = \frac{10}{0.02} \Rightarrow h_m = 0.04015 \text{ m} \approx 40 \text{ mm}$$

Furthermore, the blockage ratio of the models in the wind tunnel test section is less than 5%.

The description and dimensions of the gabled roof, mono-sloped roof, and the curved roof model buildings used in this study are shown in Figure 6.6.

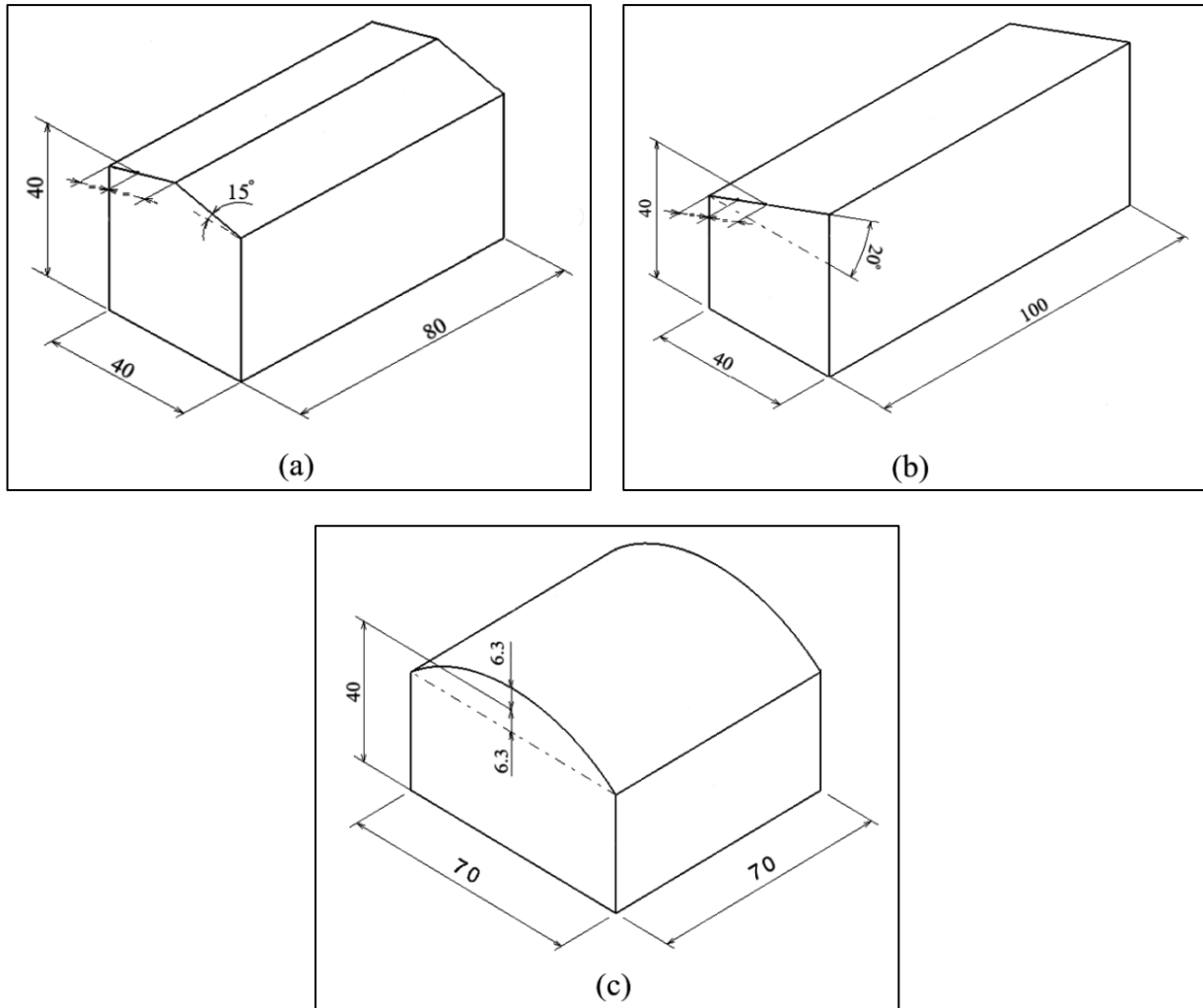


Figure 6.6 (a) The model of the gabled roof building, (b) The model of the mono-sloped roof building, (c) The model of the curved roof building, dimensions in mm

6.3.2 Numerical Simulation Procedure

6.3.2.1 Geometry and Mesh

After creating models of the three buildings in the Catia program, they were placed separately at the test section of our virtual wind tunnel to calculate the pressure coefficients on their walls and roofs.

The computational domain was created by halving the collector, the test section, and the modeled building due to symmetrical modeled buildings when the wind is blowing on them at the zero wind direction azimuth. The unstructured mesh was generated by the same procedure used for the empty virtual wind tunnel in the sub-subsection (6.2.1) with a 4 mm for all the model building faces and 2 cm influence of half-sphere with 30 cm diameter around the building model, as shown in Figure 6.7.

There is a slight difference between the numbers of elements created in each unstructured mesh depending on the geometry of the modeled buildings, as summarized in (Table 6-2).

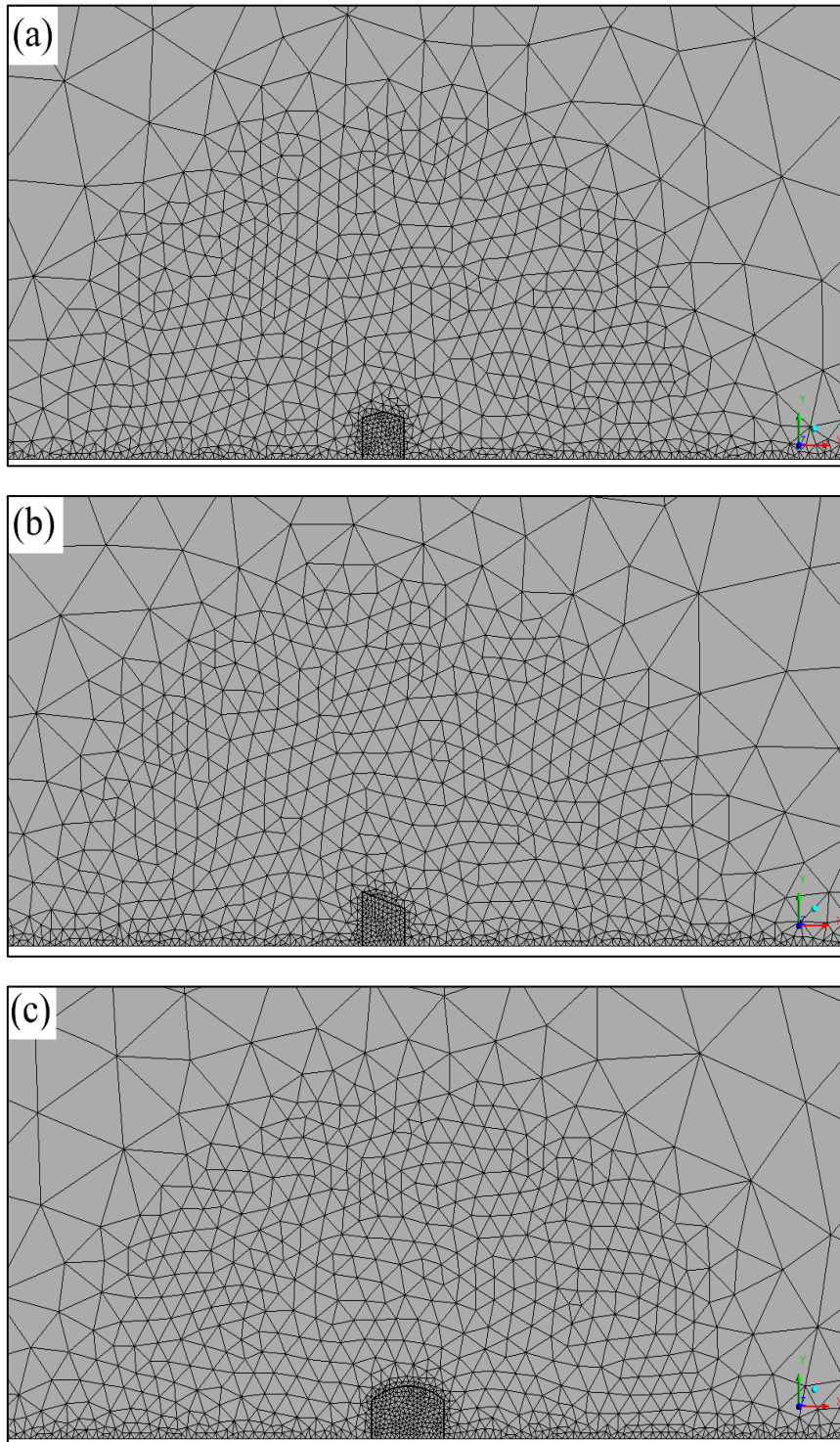


Figure 6.7 The unstructured meshes generated for model buildings and zones around them: (a) gabled roof (b) mono-sloped roof, (c) curved roof

Table 6-2 The number of elements created in each unstructured mesh

The low rise building shape	The number of elements on the control volume
gabled roof	3,125,140
mono-sloped roof	3,125,979
curved roof	3,128,167

6.3.2.2 Setup and Solution

These processes were performed using the same solver of (RANS) equations, turbulence model, solution methods, and boundary conditions described in the previous chapter, except the inlet boundary condition. Considering the equal volume flow rate through the collector, the ‘inlet velocity’ boundary condition was set at 1.459 m/s at the collector inlet that corresponds to 10 m/s at the inlet of the virtual wind tunnel test section.

The solution convergence reached while the mass flow rate at outlet in the solution monitor remained steady, and the convergence criterion is about 10^{-6} .

6.4 Results and Discussion

6.4.1 Area-averaged Pressure Coefficients

The pressure coefficients on the chosen low-rise buildings presented in the Australian/New Zealand standard are used to validate the CFD model. The local pressure coefficients are represented by a non-dimensional parameter C_p as

$$C_{p_i} = \frac{P_i - P_0}{1/2 \rho V_0^2} \quad (6-1)$$

where P_i - is the pressure on the building walls or roof,

P_0 - is the pressure of the undisturbed flow of air at a reference height,

ρ - is the density of the undisturbed flow of air ($\rho = 1.2 \text{ kg/m}^3$ in the AS-NZS 1170-2, 2011 standard),

V_0 - is the velocity of the undisturbed airflow at the average roof height.

The local pressure coefficients are measured from wind tunnel experiments on small scale models or experimental results from full scale buildings at many taps locations. So, for the effective area as walls or roofs, the area-averaged pressures coefficients are calculated by integrating the instantaneous local wind pressure coefficients after being factored by the contributing area to each pressure tap being considered in the effective area. The area-averaged pressure coefficient for each contributing area is calculated by the following expression [1]:

$$C_{p,A} = \frac{1}{\sum_{i=1}^n A_i} \sum_{i=1}^n C_{p_i} A_i \quad (6-2)$$

in which (A_i) is the contributing area to the i^{th} pressure tap, and (n) is the number of pressure taps in the precise area (A). The possible errors during integration are reduced using a high pressure tap density to the models tested in experiments and using a high mesh density on and around the models for the numerical simulation.

In the AS-NZS 1170-2, 2011 standard, the area average pressure coefficients for the faces of several types of low-rise buildings are provided in figures and tables according to different building parameters (e.g. dimensions). These parameters are shown in Figure 6.8 for the gabled roof and mono-sloped roof low-rise buildings and in Figure 6.9 for the curved roof low-rise building.

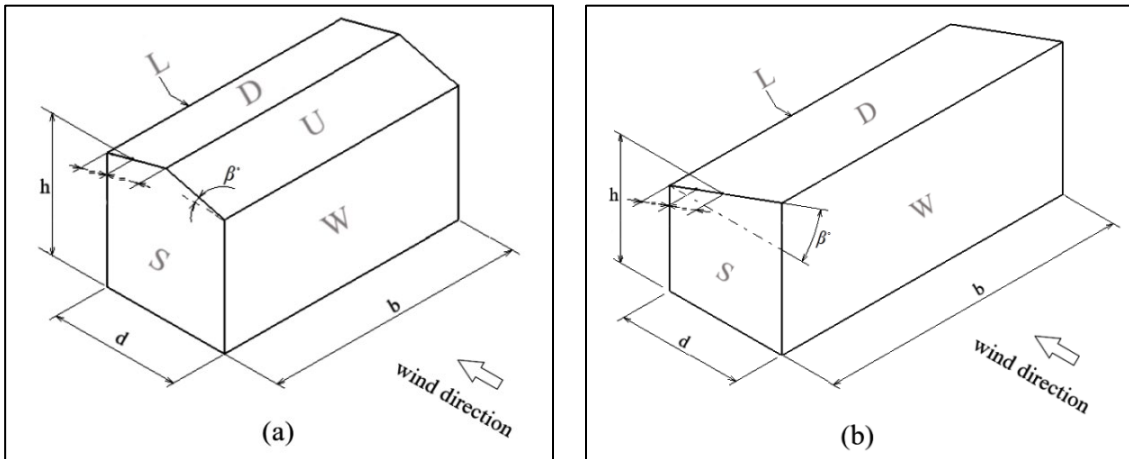
As the summary from these tables, the area average pressure coefficients on the gabled roof and mono-sloped roof low-rise buildings are:

- the same for windward walls,
- based on the ratios between the base dimensions of the buildings (b/d) and the roof angles (β) for leeward walls,
- assigned according to the horizontal distance from the windward wall for side walls,
- given according to the roof angles (β) and the ratios (h/d) for roof slopes.

whereas the area average pressure coefficients on the curved roof low-rise buildings are:

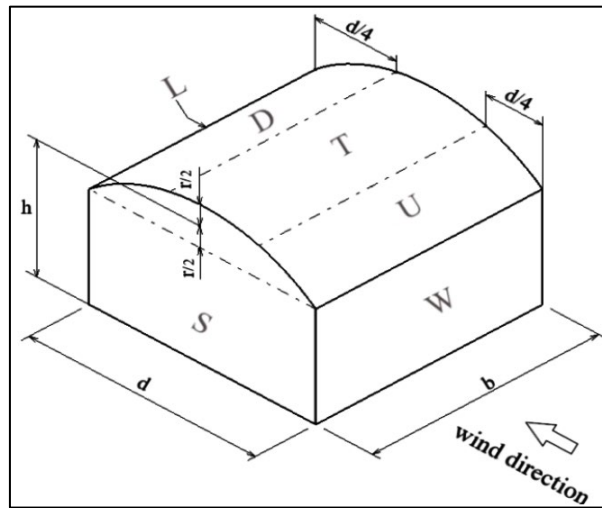
- the same for windward walls,
- unlisted for leeward walls,

- unlisted for side walls,
- given according to the ratios (r/h) for the curved roofs.



LEGEND:
 W = Windward wall U = Upwind roof slope
 S = Side wall D = Downwind roof slope
 L = Leeward wall

Figure 6.8 (a) Parameters for the gabled roof low-rise buildings, (b) Parameters for the mono-sloped roof low-rise buildings



LEGEND:
 W = Windward wall U = Windward quarter roof
 S = Side wall T = Centre half roof
 L = Leeward wall D = Downwind quarter roof

Figure 6.9 Parameters for the curved roof low-rise buildings

6.4.2 Comparison of the CFD Results with the AS-NZS 1170-2, 2011 Standard

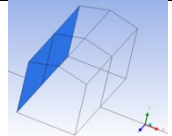
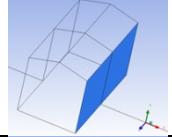
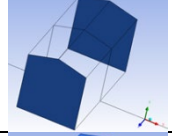
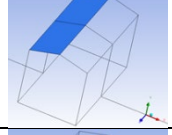
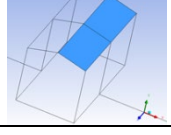
The area average pressure coefficients for the three types of low-rise buildings were calculated by the CFD using equations (6-1) and (6-2) and compared with the listed pressure coefficients in the AS-NZS 1170-2, 2011 standard. From the flow results of CFD analysis for our empty virtual wind tunnel in the central of the test section:

- the undisturbed flow pressure (p_0) was estimated at the reference height (1.5 m from the test section floor),
- the undisturbed flow velocity (V_0) was estimated at the average roof height of the three chosen low rise buildings (0.04 m from the test section floor).

6.4.2.1 The Comparison on the Gabled roof low-rise building

The pressure coefficients on the faces of the chosen gabled roof low-rise building were obtained from standard tables (5.2A), (5.2B), and (5.2C) for the walls, and from tables (5.3B) and (5.3C) for the roofs, using our building parameters $d/b=0.5$, $\beta=15^\circ$, and $h/d=1$. After that, the calculated area average pressure coefficients by CFD were compared with the obtained pressure coefficients, and the results are given in Table 6-3.

Table 6-3 Comparison of the pressure coefficients on the gabled roof low-rise building

	Locations	CFD Results	AS/NZS 1170.2:2011
	Windward Wall	0.63	0.7
	Leeward Wall	-0.28	-0.3
	Side Wall	-0.58	-0.65
	Upward Roof	-0.83	-1, -0.5
	Downward Roof	-0.57	-0.6

From the table above, the C_p values calculated by CFD are very similar to AS/NZS values, with a dissimilarity of less than 10% for all building faces. When the standard lists two values of C_p , the roofs intend to be designed for both values, and in this case, the roofs may be exposed to either value due to turbulence. The local pressure coefficients on the model faces are shown in Figure 6.10 for the wind blowing in the x-direction.

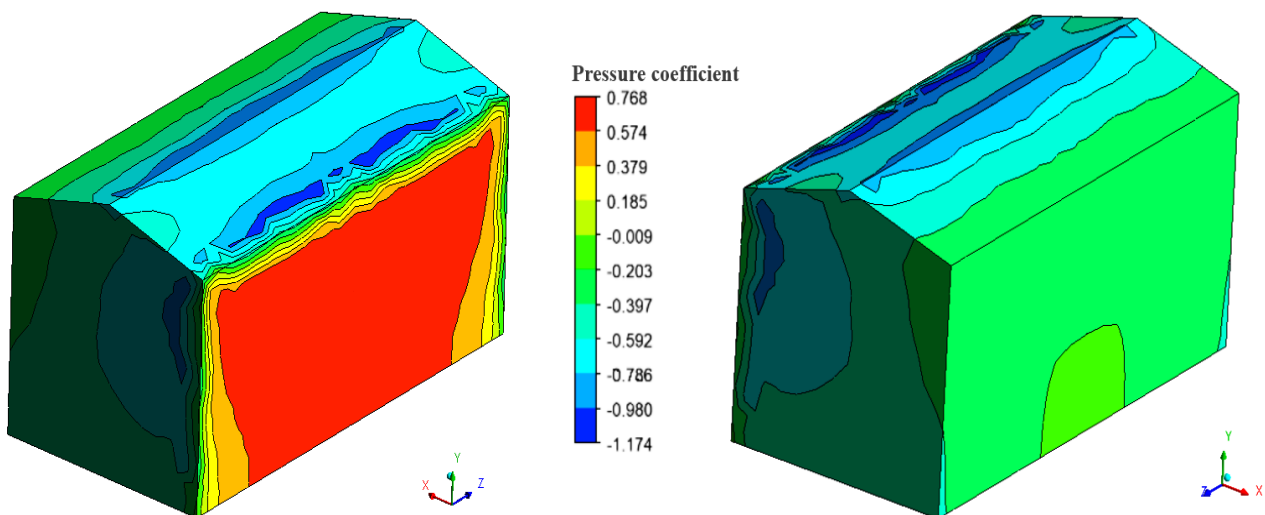


Figure 6.10 Pressure coefficient distributions for the gabled roof model, frontal (left) and rear (right) isometric view

The windward wall registered the highest positive pressure coefficient, and the magnitude of C_P decreased slightly along the wall edges. The side walls generally have little local changes in the pressure coefficient, and higher negative pressure coefficients are noted at the front edges of the side wall due to the flow separation at this edge. The leeward wall registered less suction than the side walls, and the registered negative pressure coefficients on the leeward wall were relatively constant due to the fact that the flow is fully separated from the downward roof.

For the roof, it was noticed that the suction over the upward roof was more than that over the downward roof, although the upward roof registered positive pressure coefficients at its leading edge due to the roof angle. Higher values of negative pressure coefficient registered close the leading edge of the upward roof and on the roof ridge, caused by the separation of the flow at these locations resulting in high suction in the nearby region. Figure 6.11 shows these separations zone and recirculation wake around the model.

However, a similar trend of the pressure coefficient over the gabled roof low-rise buildings with a roof angle higher than 10° was observed by Ho et al. [109].

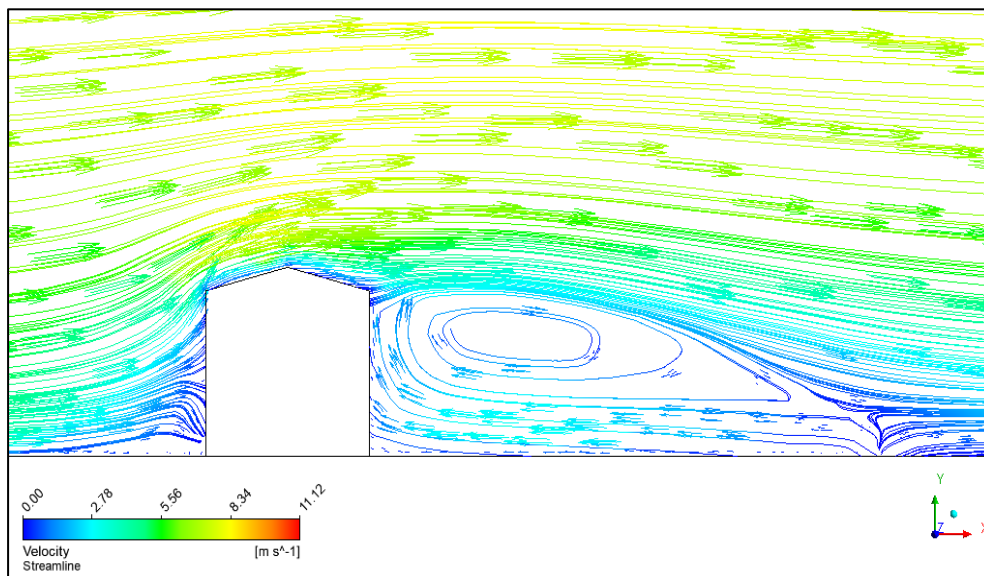
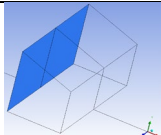
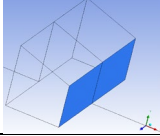


Figure 6.11 Flow pattern around the gabled roof model at a vertical section

6.4.2.2 The Comparison on the Mono-sloped roof low-rise building

The pressure coefficients on the faces of the chosen mono-sloped roof low-rise building were obtained from standard tables (5.2A), (5.2B), and (5.2C) for the walls, and from the table (5.3C) for the roof using our building parameters, $d/b=0.4$, $\beta=20^\circ$, and $h/d=1$. After that, the area average pressure coefficients calculated by CFD were compared with these obtained pressure coefficients, and the results are given in Table 6-4.

Table 6-4 Comparison of the pressure coefficients on the mono-sloped roof low-rise building

	Locations	CFD Results	AS/NZS 1170.2:2011
	Windward Wall	0.65	0.7
	Leeward Wall	-0.37	-0.4

	Side Wall	-0.65	-0.65
	Downward Roof	-0.6	-0.6

From Table 6-4, one can see that the obtained C_p values by CFD are similar to AS/NZS values, with a maximum relative error equal to 7.5% on the leeward wall. The local pressure coefficients on the model faces are shown in Figure 6.12.

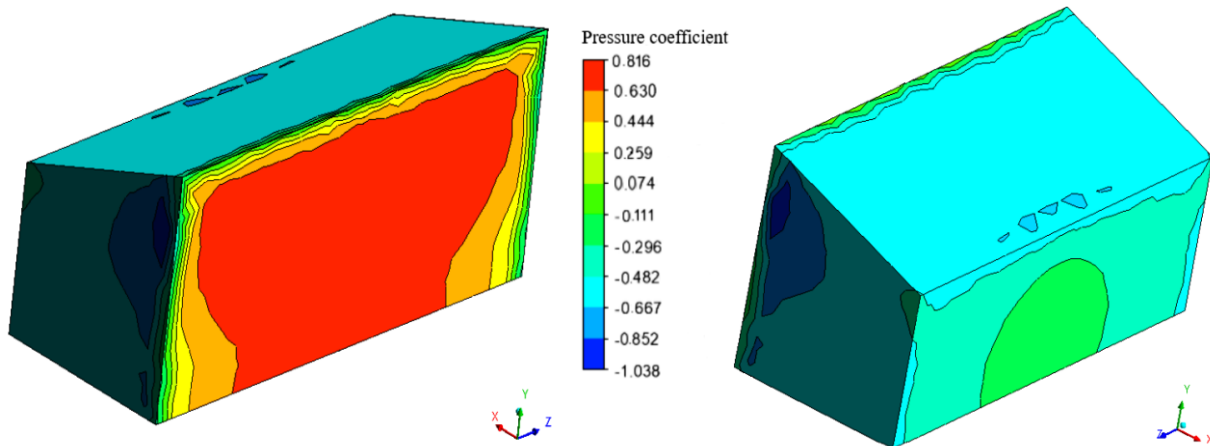


Figure 6.12 Pressure coefficient distributions for the mono-sloped roof model, frontal (left) and rear (right) isometric view

The pressure coefficient distributions of the windward wall and the leeward wall have a similar graphic configuration as in the gable roof model. The highest negative pressure coefficients were noted at the front edges of the side walls. The downward roof observed less suction than the side walls, the higher values of the negative pressure coefficient registered near the back edge due to separate flow of the recirculation wake at this edge. The recirculation wake generated behind the roof and the leeward wall due to the roof angle, as shown in Figure 6.13.

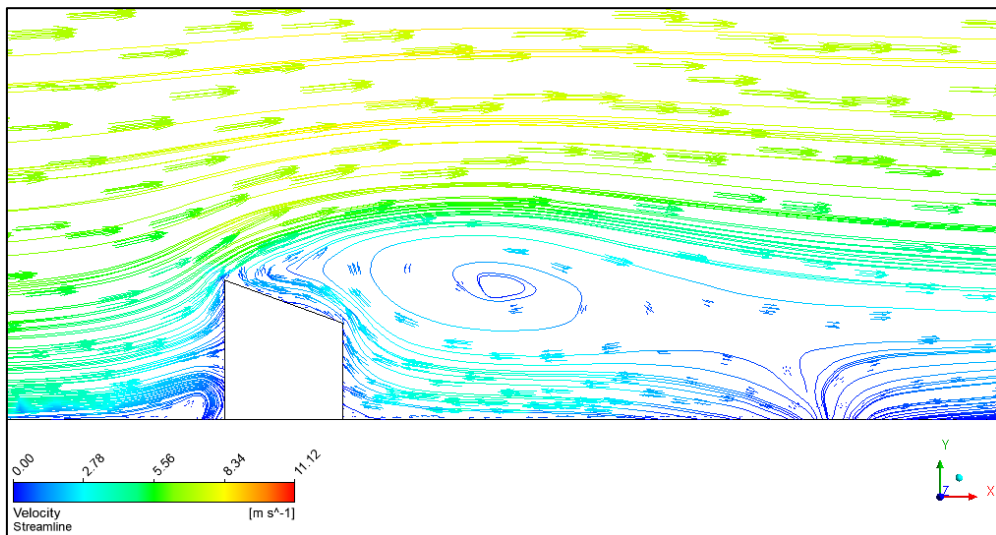
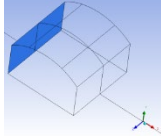
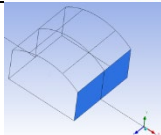
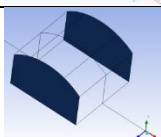
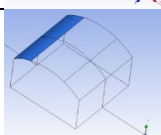
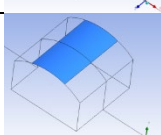
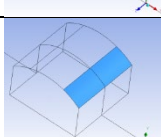


Figure 6.13 Flow pattern around the mono-sloped roof model at a vertical section

6.4.2.3 The Comparison on the Curved roof low-rise building

The pressure coefficients on the faces of the chosen curved roof low-rise building were obtained from the standard table (5.2A) for the windward wall and from the table (C3) for the roof using our building parameters, $r/d=0.18$, $(b/d)^{0.25}=1$, and $h/r= 3.17$, with a note for table C3 that h/r value shall be 2 when $h/r >2$. For leeward and side walls, no values of pressure coefficients are listed in the standard. After that, the calculated area average pressure coefficients by CFD were compared with the obtained pressure coefficients, and the results are presented in Table 6.5.

Table 6.5 Comparison of the pressure coefficients on the curved roof low-rise building

	Locations	CFD Results	AS/NZS 1170.2:2011
	Windward Wall	0.66	0.7
	Leeward Wall	-0.18	/
	Side Wall	-0.47	/
	Windward Quarter Roof	-0.45	-0.5 or 0
	Centre Half Roof	-0.89	-0.95
	Leeward Quarter Roof	-0.6	-0.65 or 0

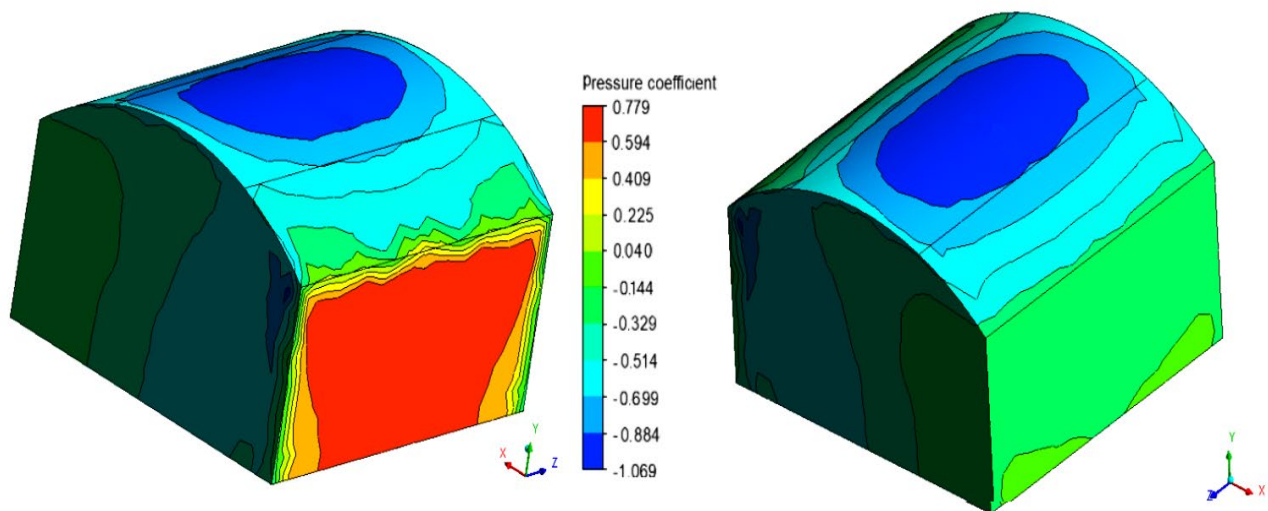


Figure 6.14 Pressure coefficient distributions for the curved roof model, frontal (left) and rear (right) isometric view

From table 6.5, one can see that the obtained C_P values by CFD are also similar to AS/NZS available values, with a maximum relative error of 10% registered on the windward quarter roof. The zero values afforded for the windward and leeward quarter roof are substitute values for action effects, such as bending which are sensitive to pressure distribution. The local pressure coefficients on the model faces are shown in Figure 6.14.

The pressure coefficient distributions of the windward wall have a similar graphic configuration as in the gable roof and mono-slope roof models. Also, the registered negative pressure coefficients on the leeward wall were relatively constant. The windward quarter roof observed less suction than the other roof portions due to the positive pressure coefficients at its leading edge. The highest negative pressure coefficients were noted at the upper front edges of the side walls and the center half roof. The negative pressure coefficients on the roof began increasing after the leading edge of the windward quarter roof as the separation of the flow started until getting the highest value along the back area of the center half roof, then began decreasing along the leeward quarter roof as the flow reattachment the roof. This separation and reattachment of the flow with the recirculation wake around the model are shown in Figure 6.15.

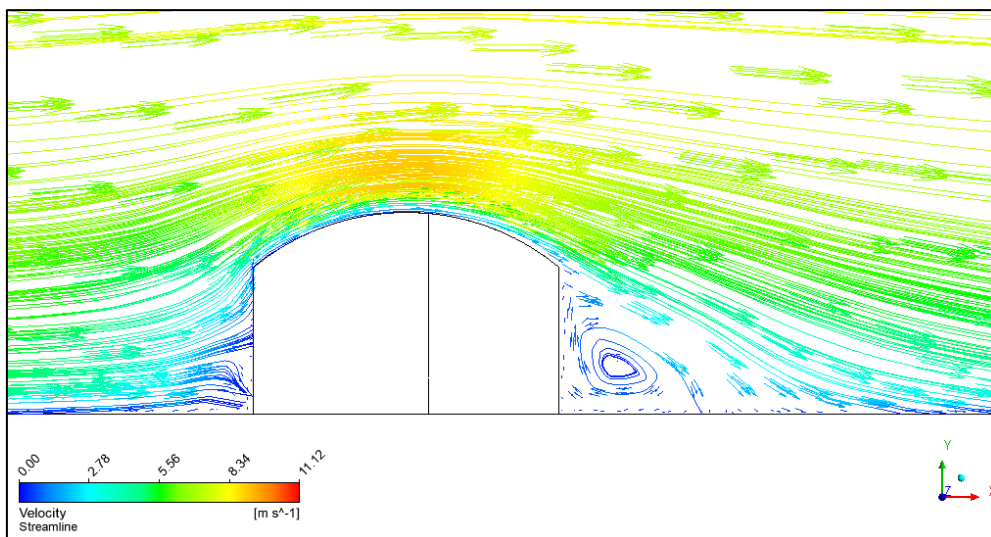


Figure 6.15 Flow pattern around the curved roof model at a vertical section

CHAPTER 7: CONCLUSION AND RECOMMENDATIONS FOR FUTURE WORK

7.1 Summary and Conclusion

In the past, several types of research were published on the use of CFD to model wind flow in and around buildings, and most of them have focused on which type of turbulence model can predict accurate results. Moreover, according to the computational domain size of the CFD model, some of them have performed a conventional approach that needs well-known boundary conditions, and others have used the entire wind tunnel as a computational domain, which is computationally expensive. The primary involvement of the current research study was to provide an accurate, reliable, and low-cost CFD computational model that works as a virtual wind tunnel to model the complex built environment or terrain exposure and study the influence of wind flow on low and medium-rise buildings. The provided computational model is based on:

1. The computational domain size, which has been implemented by modeling the contraction cone and test section, including used passive devices with/without building models, all using actual dimensions in the wind tunnel. Advantages of this size are easier setup for boundary conditions than the conventional approach and a lower number of mesh elements than the entire wind tunnel domain.
2. Use the *SST k- ω* model, one of the well-predicated turbulence models for ABL flow and pressures on buildings.
3. Allocate a large volume of grid cells at the inner boundary layer, around the vicinity of the building model, which enable better reproduction of the flow features and distribution of pressure in those regions.
4. Use an accurate solver, schemes, and solution methods.

In order to meet the primary goal, several numerical simulations have been performed in commercial Ansys Fluent code. The first simulations were performed to predict velocity profiles of various ABLs generated in the empty test section of various wind tunnels at different air blowing speeds. Two ABLs have been generated in the Assuit University wind tunnel at lower subsonic speeds 1 - 4 m/s, and another ABL has been generated in the Belgrade University wind tunnel at a subsonic speed of 45 m/s (these particular tests were performed in 1992). The predicted velocity profiles were compared with the measured data of previous experimental tests.

The second simulations were performed to predict absolute pressures on the complex model shape of a medium-rise building at different wind directions and different blowing speeds. The building model was tested in the Belgrade University wind tunnel in the year 2020, within the investigations performed as a part of the fulfillment of this Ph.D. thesis. The model has been tested at 0°, 45°, 90°, and 135° wind blowing angles and by varying air velocity from 5 to 20 m/s at each angle. The absolute pressures on the model faces were measured using special instruments. Special adapters, silicone tubes, a multi-manometer box to house all sensors, and an Arduino microcontroller board were assembled to interact with a computer for real-time recordings of these pressures. The sensors have been calibrated and tested to provide good accuracy during measurements. The predicted absolute pressures were compared with the provided measured pressures in all tested cases.

Final simulations were performed to predict pressure coefficients on three types of low-rise building models separately, at one wind direction and one blowing speed. The buildings were immersed in an open country exposure generated in the virtual test section of Belgrade University Wind Tunnel. The predicted results were compared to one of the national wind standards data considering their data presented according to the open country exposure that its key parameters as power exponent, roughness length, and turbulence intensity have specific values on each standard.

Specific conclusions regarding the results presented in this thesis can be stated as follows:

- The provided CFD model has successfully predicted velocity profiles over smooth and suburban terrains at lower subsonic speeds 1 - 4 m/s in the Assuit University wind tunnel and over urban terrain at higher subsonic speed 45 m/s in the Belgrade University wind tunnel. These results demonstrated this model's ability to simulate various ABLs for a wide speed range, which can help investigate the influence of wind on different buildings built in different terrain categories.
- The absolute pressures on the medium-rise building model have been generally well predicted compared with values measured in the wind tunnel, especially for the flow perpendicular to the building. The maximum predicted pressure value on building faces was of the order of 42 Pa. The agreements here indicating that the same CFD model can readily be used for predicted pressures on medium-rise buildings, even for its specific small structures.
- The ability of the provided CFD model to be used as a design assistant tool has been established when the model succeeded in simulating the ABL profiles of open terrain in the virtual test section of Belgrade University Wind Tunnel. The ABL was generated by redesign some of the used passive devices in the previous tests in this wind tunnel. This simulated ABL has key parameters value close to the Australian/New Zealand Standard terms.
- The accuracy of the provided CFD model has also been proven to predict pressure coefficients on all faces of several low-rise building models. The predicted pressure coefficients on the gabled roof, mono-sloped roof, and curved roof low-rise building models agree well with the Australian/New Zealand Standard data. This validation gives the CFD model access to cover missing data of this standard by predicting pressure coefficients on low-rise buildings with complex roof shapes and buildings under various oblique wind directions.

Besides the quantitative analyses presented above, some other qualitative analyses have been performed using the established CFD model. The results of these qualitative analyses have shown the capability of this model to substitute a vast portion of more costly wind tunnel test runs and working hours. These qualitative analyses can be listed as follows:

- The contours of calculated mean velocity and local eddy viscosity inside the empty test sections of the Assuit and Belgrade University wind tunnels were displayed to provide a detailed insight into the flow-fields within the simulated ABLs.
- The contours of predicted pressure distributions on the medium-rise building model and eddy viscosity distributions on the wind tunnel test section were presented to show the influence of wind on and around the building walls.
- The contours of predicted pressure coefficient distributions on the low-rise building models and velocity streamlines in the middle of the wind tunnel test section were presented to show the critical area of pressure and suction on buildings walls, separations zone, and recirculation wake around the buildings.

These qualitative analyses can be extended to study natural ventilation on the building, gas plumes dispersion from the building, pedestrian wind level comfort, solar cell mounting above the building, etc.

7.2 Recommendations for Future Work

- The current study results showed the efficiency of the provided CFD model to study wind influence on isolate building models immersed in constant terrain exposure. Future work can examine this CFD model's accuracy for studying wind influence on building in the group or surrounded by other obstacles, a building located over a hill or located in any mixed terrain exposures, building with complex shape and configurations.
- Performing other simulations using other turbulence models and comparing their

results with the suggested turbulence model results, this may help in improving the computational model efficiency and accuracy.

- Extend the use of the provided CFD model to survey computational parameters for airflow in indoor environments, such as natural ventilation strategies, since this CFD model showed good accuracy to model wind flows around buildings.

REFERENCES

- [1] Alrawashdeh, H., 2015, “Wind Pressures on Flat Roof Edges and Corners of Large Low Buildings,” Ph.D. Thesis, Building, Civil & Environmental Engineering Department, Concordia University, Montreal, Quebec, Canada.
- [2] Snæbjörnsson, J. T., 2002, “Full- and Model Scale Study of Wind Effects on a Medium-Rise Building in a Built up Area,” Ph.D. Thesis, Structural Engineering Department, University of Science and Technology, Norway.
- [3] Holmes, J. D., 2004, *Wind Loading of Structures.*, Taylor & Francis e-Library, Spon Press.
- [4] Phillips, D. A., and Soligo, M. J., 2019, “Will CFD Ever Replace Wind Tunnels for Building Wind Simulations?,” *Int. J. High-Rise Build.*, **8**(2), pp. 107–116.
- [5] Montazeri, H., and Blocken, B., 2013, “CFD Simulation of Wind-Induced Pressure Coefficients on Buildings with and without Balconies: Validation and Sensitivity Analysis,” *Build. Environ.*, **60**, pp. 137–149.
- [6] Ahmed, S., Muzzammil, M., and Zaheer, I., 2011, “Numerical Prediction of Wind Loads on Buildings,” *Int. J. Eng. Sci. Technol.*, **3**(5), pp. 59–72.
- [7] Bedair, R., 2009, “Comprehensive Study of Wind Loads on Parapets,” Ph.D. Thesis, Building, Civil & Environmental Engineering Department, Concordia University, Montreal, Quebec, Canada.
- [8] Kim, D., 2013, “The Application of CFD to Building Analysis and Design : A Combined Approach of an Immersive Case Study and Wind Tunnel Testing,” Ph.D. Thesis, Architecture and Design Research Department, Virginia Polytechnic Institute and State University, USA.
- [9] Xing, F., 2019, “Experimental and Numerical Investigation of Wind Flow Around Gable Roof Low-Rise Buildings With,” MSc Thesis, Philosophy Department, Sydney University, Australia.
- [10] Aldoum, M., 2018, “Wind Loads on Low-Slope Roof of Low-Rise and Mid-Rise Buildings with Large Plan Dimensions,” MSc Thesis, Building, Civil & Environmental Engineering Department, Concordia University, Montreal, Quebec, Canada.
- [11] Garratt, J. R., 1992, *The Atmospheric Boundary Layer.*, Cambridge University Press, Cambridge, United Kingdom.
- [12] Cermak, J. E., 1975, “Applications of Fluid Mechanics to Wind Engineering—A Freeman Scholar Lecture,” *J. Fluids Eng.*, **97**(1), pp. 9–38.
- [13] Aynsley, R., Melbourne, W., and Vickery, B., 1977, “Architectural Aerodynamics,” *Build. Environ.*, **14**(4), pp. 275--276.
- [14] Song, P., 2017, “Simulation of Atmospheric Boundary Layer in an Open-Loop Wind Tunnel Using Spire-Roughness-Element Technique,” MSc Thesis, Civil & Environmental Engineering Department, Windsor University, Windsor, Ontario, Canada.
- [15] Kaimal, J. C., and Finnigan, J. J., 1994, *Atmospheric Boundary Layer Flows: Their Structure and Measurement*, Oxford University Press, New York.
- [16] Roth, M., 2000, “Review of Atmospheric Turbulence over Cities,” *Q. J. R. Meteorol. Soc.*, **126**(564), pp. 941–990.
- [17] Buschmann, M. H., and Gad-el-Hak, M., 2003, “Debate Concerning the Mean-Velocity Profile of a Turbulent Boundary Layer,” *AIAA J.*, **41**(4), pp. 565–572.
- [18] Ikhwan, M., 2005, “Investigation of Flow and Pressure Characteristics around Pyramidal Buildings,” Ph.D. Thesis, Department of geo- and environmental sciences, Karlsruhe Institute of Technology, Germany.
- [19] Satya, R. D. B. E., 2004, “Boundary Layer Characteristics Just Above Sub-Urban Roughness,” MSc Thesis, Civil Engineering Department, Texas Tech University, Lubbock, Texas, USA.

- [20] V. Burton, W., 2001, "Wind Tunnel Simulation of an Atmospheric Boundary Layer," MSc Thesis, Mechanical Engineering Department, Texas Tech University, Lubbock, Texas, USA.
- [21] Niemann, H. J., 1993, "The Boundary Layer Wind Tunnel: An Experimental Tool in Building Aerodynamics and Environmental Engineering," *J. Wind Eng. Ind. Aerodyn.*, **48**, pp. 145–161.
- [22] Lindgren, B., and Johansson, A., 2002, *Design and Evaluation of a Low-Speed Wind-Tunnel with Expanding Corners.*, Royal Institute of Technology, Stockholm, Sweden.
- [23] Cermak, B. J. E., and Asce, F., 1984, "Wind-Simulation Criteria for Wind-Effect Tests," *J. Struct. Eng.*, **110**(2), pp. 328–339.
- [24] Irwin, H. P. A. H., 1981, "The Design of Spires for Wind Simulation," *J. Wind Eng. Ind. Aerodyn.*, **7**(3), pp. 361–366.
- [25] Cook, N. J., 1978, "Wind-Tunnel Simulation of the Adiabatic Atmospheric Boundary Layer by Roughness, Barrier and Mixing-Device Methods," *J. Wind Eng. Ind. Aerodyn.*, **3**, pp. 157–176.
- [26] Farrell, C., and Iyengar, A. K. S., 1999, "Experiments on the Wind Tunnel Simulation of Atmospheric Boundary Layers," *J. Wind Eng. Ind. Aerodyn.*, **79**, pp. 11–35.
- [27] Cermak, J. E., 1982, "Physical Modeling of the Atmospheric Boundary Layer (ABL) in Long Boundary-Layer Wind Tunnels (BLWT)," *Proceedings of International Workshop on Wind Tunnel Modeling Criteria and Techniques in Civil Engineering Application*, Cambridge University Press, Cambridge, UK, pp. 97–137.
- [28] Sanni, R. A., Surry, D., and Davenport, A. G., 1992, "Wind Loading on Intermediate Height Buildings," *Can. J. Civ. Eng.*, **19**(1), pp. 148–163.
- [29] Simiu, E., and Scanlan, R. H., 1996, *Wind Effects on Structures: Fundamentals and Applications to Design*, Third Edit, John Wiley & Sons, Inc, Maryland.
- [30] Neff, D. E., and Meroney, R. N., 1996, *Reynolds Number Independence of the Wind Tunnel Simulation of Transport and Dispersion about Buildings.*, Fluid Mechanics and Wind Engineering Program, Civil Engineering Department, Colorado State University, USA.
- [31] Holmes, J. D., and Carpenter, P., 1990, "The Effect of Jensen Number Variations on the Wind Loads on a Low-Rise Building," *J. Wind Eng. Ind. Aerodyn.*, **36**(PART 2), pp. 1279–1288.
- [32] Kumar, P., 2005, "Pressure-Velocity Correlation Study on 1:50 Scale Model of the TTU Wind Engineering Research Field Building," LSU Master's Theses, Department of Mechanical Engineering, Louisiana State University, USA.
- [33] Zhongshan Zhao, M. E., 1997, "Wind Flow Characteristics and Their Effects on Low-Rise Buildings," Ph.D. Thesis, Civil Engineering Department, Texas Tech University, Lubbock, Texas, USA.
- [34] Woo, H. G. C., Peterka, J. . A., and Cermak, J. E., 1976, *Wind-Tunnel Measurements in The Wakes of Structures*, Fluid Mechanics and Wind Engineering Program, Engineering Sciences Branch Library.
- [35] Peterka, J. A., Meroney, R. N., and Kothari, K. . M., 1985, "Wind Flow Patterns About Buildings," *J. Wind Eng. Ind. Aerodyn.*, **21**, pp. 21–38.
- [36] Hosker, R. P., 1981, *Methods for Estimating Wake Flow and Effluent Dispersion Near Simple Block-Like Buildings*, Air Resources Laboratories Silver Spring, Maryland.
- [37] Baines, W. . D., 1963, "Effects of Velocity Distribution on Wind Loads and Flow Patterns on Buildings," *Proceedings of the Symposium on Wind Effects on Buildings and Structures*, London.
- [38] Dalglish, W. A., and Schriever, W. R., 1965, *Wind Pressures and Suctions on Roofs.*, Division of Building Research, National Research Council, Ottawa, Canada.
- [39] Stone, J. B., "Designing for High Winds: Wood Is a Proven Choice for Wind-Resistive Construction," Rethink Wood.
- [40] Dalglish, W. A., and Schriever, W. R., 1962, *Wind Pressures on Buildings*, National Research Council Canada CBD, Canada.

- [41] Hunt, A., 1982, “Wind-Tunnel Measurements of Surface Pressures on Cubic Building Models at Several Scales,” *J. Wind Eng. Ind. Aerodyn.*, **10**(2), pp. 137–163.
- [42] Wacker, J., 1995, “Local Wind Pressures for Rectangular Buildings in Turbulent Boundary Layers,” *Wind Climate in Cities*, Springer Netherlands, pp. 185–207.
- [43] Stathopoulos, T., 2007, “Introduction to Wind Engineering, Wind Structure, Wind-Building Interaction,” *CISM Int. Cent. Mech. Sci. Courses Lect.*, **493**, pp. 1–30.
- [44] Ozmen, Y., Baydar, E., and van Beeck, J. P. A. J., 2016, “Wind Flow over the Low-Rise Building Models with Gabled Roofs Having Different Pitch Angles,” *Build. Environ.*, **95**, pp. 63–74.
- [45] Blocken, B., Stathopoulos, T., Carmeliet, J., and Hensen, J. L. M., 2011, “Application of Computational Fluid Dynamics in Building Performance Simulation for the Outdoor Environment: An Overview,” *J. Build. Perform. Simul.*, **4**(2), pp. 157–184.
- [46] Blocken, B., 2015, “Computational Fluid Dynamics for Urban Physics: Importance, Scales, Possibilities, Limitations and Ten Tips and Tricks towards Accurate and Reliable Simulations,” *Build. Environ.*, **91**, pp. 219–245.
- [47] Parente, A., and Benocci, C., 2010, “On the RANS Simulation of Neutral ABL Flows,” *Comput. Wind Eng.*, (November), pp. 1–9.
- [48] Shojaee, S. M. N., Uzol, O., and Kurç, Ö., 2014, “Atmospheric Boundary Layer Simulation in a Short Wind Tunnel,” *Int. J. Environ. Sci. Technol.*, **11**(1), pp. 59–68.
- [49] Abdulrahim, A., Elfarrar, M., and Uzol, O., 2019, “A Numerical Assessment of Atmospheric Boundary Layer,” *10th Ankara International Aerospace Conference AIAC-2019-151*, Ankara, Turkey, pp. 1–11.
- [50] Amerio, L., 2014, “Numerical and Experimental Analysis of Peak Pressure Loads on Rectangular Building,” MSc Thesis, Structures Department, Polytechnic University of Milan, Italy.
- [51] Yassen, Y. E.-S., and Abdelhamed, A. S., 2015, “CFD Modeling of the Atmospheric Boundary Layer in Short Test Section Wind Tunnel,” *Am. J. Aerosp. Eng.*, **2**(1), pp. 38–46.
- [52] Pires, L. B. M., De Paula, I. B., Fisch, G., Gielow, R., and Girardi, R. da M., 2013, “Simulations of the Atmospheric Boundary Layer in a Wind Tunnel with Short Test Section,” *J. Aerosp. Technol. Manag.*, **5**(3), pp. 305–314.
- [53] Yang, Y., Gu, M., Chen, S., and Jin, X., 2009, “New Inflow Boundary Conditions for Modelling the Neutral Equilibrium Atmospheric Boundary Layer in Computational Wind Engineering,” *J. Wind Eng. Ind. Aerodyn.*, **97**(2), pp. 88–95.
- [54] Calautit, J. K., Chaudhry, H. N., Hughes, B. R., and Sim, L. F., 2014, “A Validated Design Methodology for a Closed-Loop Subsonic Wind Tunnel,” *J. Wind Eng. Ind. Aerodyn.*, **125**, pp. 180–194.
- [55] Moonen, P., Blocken, B., Roels, S., and Carmeliet, J., 2006, “Numerical Modeling of the Flow Conditions in a Closed-Circuit Low-Speed Wind Tunnel,” *J. Wind Eng. Ind. Aerodyn.*, **94**(10), pp. 699–723.
- [56] Blanco, M., 2019, “Design and Qualification of a Boundary-Layer Wind Tunnel for Modern CFD Validation Experiments,” MSc Thesis, Mechanical Engineering Department, Youngstown State University, USA.
- [57] Pook, D. A., and Watmuff, J. H., 2014, “Streak Generation in Wind Tunnels,” *Phys. Fluids*, **26**, p. 19.
- [58] Downie, T. E., and Huynh, B. P., 2014, “Turbulent Airflow Past a Rectangular Cylinder Building,” *Proceedings of the 19th Australasian Fluid Mechanics Conference, AFMC 2014*, p. 5.
- [59] Van Druenen, T., van Hooff, T., Montazeri, H., and Blocken, B., 2019, “CFD Evaluation of Building Geometry Modifications to Reduce Pedestrian-Level Wind Speed,” *Build. Environ.*, **163**, p. 24.
- [60] Hubova, O., Macak, M., Konecna, L., and Ciglan, G., 2017, “External Pressure Coefficients on the Atypical High-Rise Building - Computing Simulation and Measurements in Wind

- Tunnel,” *Procedia Eng.*, **190**, pp. 488–495.
- [61] Tominaga, Y., Akabayashi, S., Kitahara, T., and Arinami, Y., 2015, “Air Flow around Isolated Gable-Roof Buildings with Different Roof Pitches: Wind Tunnel Experiments and CFD Simulations,” *Build. Environ.*, **84**, pp. 204–213.
- [62] Yang, W., Quan, Y., Jin, X., Tamura, Y., and Gu, M., 2008, “Influences of Equilibrium Atmosphere Boundary Layer and Turbulence Parameter on Wind Loads of Low-Rise Buildings,” *J. Wind Eng. Ind. Aerodyn.*, **96**, pp. 2080–2092.
- [63] Peren, J. I., van Hooff, T., Leite, B. C. C., and Blocken, B., 2014, “CFD Analysis of Cross-Ventilation of a Generic Isolated Building with Asymmetric Opening Positions: Impact of Roof Angle and Opening Location,” *Build. Environ.*, **85(0)**, p. 21.
- [64] Holmes, J. D., and Paterson, D. A., 1993, “Mean Wind Pressures on Arched-Roof Buildings by Computation,” *J. Wind Eng. Ind. Aerodyn.*, **50**, pp. 235–242.
- [65] Ntinias, G. K., Shen, X., Wang, Y., and Zhang, G., 2018, “Evaluation of CFD Turbulence Models for Simulating External Airflow around Varied Building Roof with Wind Tunnel Experiment,” *Build. Simul.*, **11(1)**, pp. 115–123.
- [66] Fouad, N. S., Mahmoud, G. H., and Nasr, N. E., 2018, “Comparative Study of International Codes Wind Loads and CFD Results for Low Rise Buildings,” *Alexandria Eng. J.*, **57(4)**, pp. 3623–3639.
- [67] Abohela, I., Hamza, N., and Dudek, S., 2013, “Effect of Roof Shape, Wind Direction, Building Height and Urban Configuration on the Energy Yield and Positioning of Roof Mounted Wind Turbines,” *Renew. Energy*, **50**, pp. 1106–1118.
- [68] Revuz, J., 2011, “Numerical Simulation of the Wind Flow around a Tall Building and Its Dynamic Response to Wind Excitation,” Ph.D. Thesis, Civil Engineering Department, University of Nottingham, United Kingdom.
- [69] Moukalled, F., Mangani, L., and Darwish, M., 2016, *The Finite Volume Method in Computational Fluid Dynamics: An Advanced Introduction with OpenFOAM® and Matlab®*, Fluid Mechanics and Its Applications, Springer International Publishing Switzerland.
- [70] Ashgriz, N., and Mostaghimi, J., 2002, “An Introduction to Computational Fluid Dynamics,” *Fluid Flow Handbook*, Chapter 20, University of Toronto, Toronto, Canada.
- [71] Anderson, J. D., 1995, *Computational Fluid Dynamics. The Basics with Applications*, Department of Aerospace Engineering, University of Maryland, McGraw-Hill, Inc., New York, USA.
- [72] Chung, T. J., 2002, *Computational Fluid Dynamics*, Cambridge University Press, Cambridge, UK.
- [73] Stangroom, P., 2004, “CFD Modelling of Wind Flow over Terrain,” Ph.D. Thesis, Civil Engineering Department, University of Nottingham, United Kingdom.
- [74] ANSYS Inc, 2011, *ANSYS Fluent Theory Guide, Release 14.0*.
- [75] Chaudhry, H. M., and Mays, L. W., 1994, *Computer Modeling of Free-Surface and Pressurized Flows*, Springer Science+Business Media, Dordrecht, Netherlands.
- [76] Versteeg, H. K., and Malalasekera, W., 2007, *An Introduction to Computational Fluid Dynamics: The Finite Volume Method*, Second Edition, Pearson Education Limited, Harlow.
- [77] Yu, H., and Thé, J., 2016, “Validation and Optimization of SST K- ω Turbulence Model for Pollutant Dispersion within a Building Array,” *Atmos. Environ.*, **145**, pp. 225–238.
- [78] Moraes, A., Lage, P., Cunha, G., and Da Silva, L., 2013, “Analysis of the Non-Orthogonality Correction of Finite Volume Discretization on Unstructured Meshes,” *22nd International Congress of Mechanical Engineering (COBEM 2013)*, pp. 3519–3530.
- [79] Hu, P., Li, Y., Cai, C. S., Liao, H., and Xu, G. J., 2013, “Numerical Simulation of the Neutral Equilibrium Atmospheric Boundary Layer Using the SST K- ω Turbulence Model,” *Wind Struct.*, **17(1)**, pp. 87–105.
- [80] Hu, P., Li, Y., Han, Y., Cai, S. C. S., and Xu, X., 2016, “Numerical Simulations of the Mean Wind Speeds and Turbulence Intensities over Simplified Gorges Using the SST K- ω

- Turbulence Model,” *Eng. Appl. Comput. Fluid Mech.*, **10**(1), pp. 359–372.
- [81] Yu, Y., 2012, “Numerical Simulation of Wind Load on Roof Mounted Solar Panels,” MSc Thesis, Department of Mechanical, Automotive and Materials Engineering, University of Windsor, Canada.
- [82] Weiss, J. M., and Smith, W. A., 1995, “Preconditioning Applied to Variable and Constant Density Time-Accurate Flows on Unstructured Meshes,” *Am. Inst. Aeronaut. Astronaut. (AIAA)*, **33**(11).
- [83] Weiss, J. M., Maruszewski, J. P., and Smith, W. A., 1997, “Implicit Solution of the Navier-Stokes Equations on Unstructured Meshes,” *Am. Inst. Aeronaut. Astronaut.*, pp. 139–149.
- [84] Weiss, J. M., Maruszewski, J. P., and Smith, W. A., 1999, “Implicit Solution of Preconditioned Navier-Stokes Equations Using Algebraic Multigrid,” *Am. Inst. Aeronaut. Astronaut.*, **37**(1), pp. 29–36.
- [85] Phongthanapanich, S., and Takayama, K., 2019, “A Comparison of the Roe’s FDS, HLLC, AUFs, and AuSMDV+ Schemes on Triangular Grids,” *Appl. Sci. Eng. Prog.*, **12**(3), pp. 150–157.
- [86] Fürst, J., 2017, “On the Implicit Density Based OpenFOAM Solver for Turbulent Compressible Flows,” *EPJ Web of Conferences*.
- [87] Jemcov, A., and Maruszewski, J. P., 2010, “Algorithm Stabilization and Acceleration in Computational Fluid Dynamics: Exploiting Recursive Properties of Fixed Point Algorithms,” *Computational Fluid Dynamics and Heat Transfer*, WIT Transactions on State of the Art in Science and Engineering, pp. 459–486.
- [88] Muzaferija, S., 1994, “Adaptive Finite Volume Method for Flow Prediction Using Unstructured Meshes and Multigrid Approach,” Ph.D. Thesis, Department of Mechanical Engineering, University of London, United Kingdom.
- [89] Zubair, H. Bin, 2009, “Efficient Multigrid Methods Based on Improved Coarse Grid Correction Techniques,” MSc Thesis, Computer Science, University of Karachi, Pakistan.
- [90] Mazumder, S., 2015, *Numerical Methods for Partial Differential Equations: Finite Difference and Finite Volume Methods*, Academic Press, Elsevier.
- [91] Al-Nehari, H. A., Abdel-Rahman, A. K., Nassib, A. E.-M., and Shafey, H. M., 2010, “Design and Construction of a Low Speed Wind Tunnel for Environmental Flow Studies,” *J. Eng. Sci.*, **38**(1), pp. 177–193.
- [92] Stefanović, Z., and Pešić, S., 1992, “Simulation of Atmospheric Boundary Layer in Laboratory Conditions,” *International Symposium on Contemporary Problems in Fluid Mechanics*, Belgrade, Serbia.
- [93] Kemmer, G., and Keller, S., 2010, “Nonlinear Least-Squares Data Fitting in Excel Spreadsheets,” *Nat. Protoc.*, **5**(2), pp. 267–281.
- [94] Goliber, M. R., 2009, “Pressure Distribution on the Roof of a Model Low- Rise Building Tested in a Boundary Layer Wind Tunnel,” MSc Thesis, Department of Civil Engineering (Structural Engineering), Iowa State University, USA.
- [95] Kumar, P., 2005, “Pressure-Velocity Correlation Study on 1 : 50 Scale Model of the TTU Wind Engineering Research Field Lab Building,” MSc Thesis, Department of Mechanical Engineering, Louisiana State University, Baton Rouge, Louisiana.
- [96] Bosch, “Pressure Sensor BMP280” [Online]. Available: <https://www.bosch-sensortec.com/products/environmental-sensors/pressure-sensors/pressure-sensors-bmp280-1.html>. [Accessed: 18-Mar-2019].
- [97] Mentor, 2006, *Automated Pressure Calibrator (APC) Series 600*, Operation Manual.
- [98] ASCE/SEI 7-16, 2017, *Minimum Design Loads and Associated Criteria for Buildings and Other Structures*, Structural Engineering Institute of ASCE, Reston, Virginia, USA.
- [99] EN1991-1-4, E. 1, 2005, *Actions on Structures-General Actions-Part 1-4: Wind Actions*, European Standard.
- [100] AS/NZS 1170.2, 2011, *Australian/New Zealand Standard for Structural Design Actions, Part 2: Wind Actions*, Standards Australia and Standards New Zealand, Sydney, New South

Wales, Australia.

- [101] NBC2015, *User's Guide-NBC 2015, Structural Commentaries (Part 4)*, Issued by the Canadian Commission on Buildings and Fire Codes, National Research Council of Canada.
- [102] Kola, S., 1995, "Comparison of Wind Load Standards," MSc Thesis, Civil Engineering Department, Texas Tech University, Lubbock, Texas, USA.
- [103] John, A. D., Roy, A. K., and Gairola, A., 2012, "Wind Loads on Walls of Low-Rise Building," *6th National Conference on Wind Engineering (NCWE)*, New Delhi, pp. 449–456.
- [104] John, A. D., Gairola, A., and Krishna, P., 2008, "Wind Loads on Overhangs in a Low Gable Building in Presence of Free Standing Wall," *J. Wind Eng.*, **5**(1), pp. 39–46.
- [105] Kayışoğlu, B., 2011, "Investigation of Wind Effects on Tall Buildings Through Wind Tunnel Testing," MSc Thesis, Civil Engineering Department, Middle East Technical University, Ankara, Turkey.
- [106] Fouad, N. S., Mahmoud, G. H., and Nasr, N. E., 2018, "Comparative Study of International Codes Wind Loads and CFD Results for Low Rise Buildings," *Alexandria Eng. J.*, **57**(4), pp. 3623–3640.
- [107] Suárez, J. D. C., 2012, "Wind-Induced Pressures on Canopies Attached to the Walls of Low-Rise Buildings," MSc Thesis, Department of Building, Civil and Environmental Engineering, Concordia University, Montreal, Quebec, Canada.
- [108] Simiu, E. P. E., and Yeo, D. P. E., 2019, *Wind Effects on Structures: Modern Structural Design for Wind*, Fourth Edition, John Wiley & Sons Ltd.
- [109] Ho, T. C. E., Surry, D., Morrish, D., and Kopp, G. A., 2005, "The UWO Contribution to the NIST Aerodynamic Database for Wind Loads on Low Buildings: Part 1. Archiving Format and Basic Aerodynamic Data," *J. Wind Eng. Ind. Aerodyn.*, **93**(1), pp. 1–30.
- [110] Endo, M., 2011, "Wind Tunnel Modeling and Analysis of Wind Effects on Low-Rise Buildings," Ph.D. Thesis, Department of Civil and Environmental Engineering, Colorado State University, USA.
- [111] Bai, Y., 2015, "A New Wind Tunnel Setup and Evaluation of Flow Characteristics with/without Passive Devices," MSc Thesis, Department of Civil and Environmental Engineering, University of Windsor, Windsor, Ontario, Canada.
- [112] Rahmat, N. A., Hagishima, A., Ikegaya, N., and Tanimoto, J., 2018, "Experimental Study on Effect of Spires on the Lateral Nonuniformity of Mean Flow in a Wind Tunnel," *Evergreen*, **5**(1), pp. 1–15.

БИОГРАФСКИ ПОДАЦИ

Ахмед Али Ирхаим Абубакер, М.Сс, дипл. инж. маш.

Ahmed Ali Irhayim Abubaker рођен је 27. 01. 1983. године у Тамизаваху, Либија. Основну школу завршио је 1997. године, док је средњу школу - природни смер завршио у граду Аламарифа 2000. године. Дипломирао је на Универзитету Сабха у Либији, на Факултету за инжењерство и технологију, Катедра за машинско инжењерство, 2005. године.

У периоду 2006. – 2008. похађао је дипломске студије на Универзитету у Триполију (раније Ал-Фатех), где је положио све предвиђене испите.

Године 2009. уписао се на Мастер академске студије на Машинском факултету Универзитета у Београду, Катедра за ваздухопловство, које је успешно завршио одбраном тезе под насловом “ CFD analysis of Separation and Reattachment for a Flow in Sudden Expansion Channel ”, 2012. године.

Докторске студије на Машинском факултету Универзитета у Београду, уписао је школске 2013/14. године на Катедри за ваздухопловство. Користи програмске пакете MS Office, MATLAB, CATIA, VLAERO, ANSYS Design Modeler, ICEM CFD, ANSYS Fluent, CFD-Post и друге. Област научно-истраживачког рада којом се бави на докторским студијама представља наставак и надградњу истраживачког рада којим се бавио током мастер академских студија. Говори енглески и арапски језик.

Изјава о ауторству

Потписани-а Ахмед Али Ирхаим Абубакер

број индекса Д1/2013

Изјављујем

да је докторска дисертација под насловом

Numerical and Experimental Simulation of Atmospheric Boundary Layer Influence on Flow Patterns around Building Structures

Нумеричка и експериментална симулација утицаја атмосферског граничног слоја на струјно поље око грађевинских објеката

- резултат сопственог истраживачког рада,
- да предложена дисертација у целини ни у деловима није била предложена за добијање било које дипломе према студијским програмима других високошколских установа,
- да су резултати коректно наведени и
- да нисам кршио/ла ауторска права и користио интелектуалну својину других лица.

Потпис аутора

У Београду, _____

Изјава о истоветности штампане и електронске верзије докторског рада

Име и презиме аутора Ахмед Али Ирхаим Абубакер

Број индекса Д1/2013

Студијски програм докторске студије

Наслов рада **Numerical and Experimental Simulation of Atmospheric Boundary Layer Influence on Flow Patterns around Building Structures** (Нумеричка и експериментална симулација утицаја атмосферског граничног слоја на струјно поље око грађевинских објеката)

Ментор проф. др Иван Костић

Изјављујем да је штампана верзија мог докторског рада истоветна електронској верзији коју сам предао/ла за објављивање на порталу **Дигиталног репозиторијума Универзитета у Београду**.

Дозвољавам да се објаве моји лични подаци везани за добијање академског звања доктора наука, као што су име и презиме, година и место рођења и датум одбране рада.

Ови лични подаци могу се објавити на мрежним страницама дигиталне библиотеке, у електронском каталогу и у публикацијама Универзитета у Београду.

Потпис аутора

У Београду, _____

Изјава о коришћењу

Овлашћујем Универзитетску библиотеку „Светозар Марковић“ да у Дигитални репозиторијум Универзитета у Београду унесе моју докторску дисертацију под насловом:

Numerical and Experimental Simulation of Atmospheric Boundary Layer Influence on Flow Patterns around Building Structures

Нумеричка и експериментална симулација утицаја атмосферског граничног слоја на струјно поље око грађевинских објеката

која је моје ауторско дело.

Дисертацију са свим прилозима предао/ла сам у електронском формату погодном за трајно архивирање.

Моју докторску дисертацију похрањену у Дигитални репозиторијум Универзитета у Београду могу да користе сви који поштују одредбе садржане у одабраном типу лиценце Креативне заједнице (Creative Commons) за коју сам се одлучио/ла.

1. Ауторство (CC BY)
2. Ауторство – некомерцијално (CC BY-NC)
3. Ауторство – некомерцијално – без прераде (CC BY-NC-ND)
4. Ауторство – некомерцијално – делити под истим условима (CC BY-NC-SA)
5. Ауторство – без прераде (CC BY-ND)
6. Ауторство – делити под истим условима (CC BY-SA)

(Молимо да заокружите само једну од шест понуђених лиценци, кратак опис лиценци дат је на полеђини листа).

Потпис аутора

У Београду, _____

1. **Ауторство.** Дозвољаваате умножавање, дистрибуцију и јавно саопштавање дела, и прераде, ако се наведе име аутора на начин одређен од стране аутора или даваоца лиценце, чак и у комерцијалне сврхе. Ово је најслободнија од свих лиценци.

2. **Ауторство – некомерцијално.** Дозвољаваате умножавање, дистрибуцију и јавно саопштавање дела, и прераде, ако се наведе име аутора на начин одређен од стране аутора или даваоца лиценце. Ова лиценца не дозвољава комерцијалну употребу дела.

3. **Ауторство - некомерцијално – без прераде.** Дозвољаваате умножавање, дистрибуцију и јавно саопштавање дела, без промена, преобликовања или употребе дела у свом делу, ако се наведе име аутора на начин одређен од стране аутора или даваоца лиценце. Ова лиценца не дозвољава комерцијалну употребу дела. У односу на све остале лиценце, овом лиценцом се ограничава највећи обим права коришћења дела.

4. **Ауторство - некомерцијално – делити под истим условима.** Дозвољаваате умножавање, дистрибуцију и јавно саопштавање дела, и прераде, ако се наведе име аутора на начин одређен од стране аутора или даваоца лиценце и ако се прерада дистрибуира под истом или сличном лиценцом. Ова лиценца не дозвољава комерцијалну употребу дела и прерада.

5. **Ауторство – без прераде.** Дозвољаваате умножавање, дистрибуцију и јавно саопштавање дела, без промена, преобликовања или употребе дела у свом делу, ако се наведе име аутора на начин одређен од стране аутора или даваоца лиценце. Ова лиценца дозвољава комерцијалну употребу дела.

6. **Ауторство - делити под истим условима.** Дозвољаваате умножавање, дистрибуцију и јавно саопштавање дела, и прераде, ако се наведе име аутора на начин одређен од стране аутора или даваоца лиценце и ако се прерада дистрибуира под истом или сличном лиценцом. Ова лиценца дозвољава комерцијалну употребу дела и прерада. Слична је софтверским лиценцама, односно лиценцама отвореног кода.